Theory and Simulation of the Microwave Response of Concentric Ferromagnetic Shells

Submitted by **Conor John McKeever** to the University of Exeter as a thesis for the degree of Doctor of Philosophy in Physics, in September 2018.

I certify that all material in this thesis which is not my own work has been identified and that no material has previously been submitted and approved for the award of a degree by this or any other University.

. . . . . .

1

Abstract

Structured ferromagnetic metal-based metamaterials comprised of spherical particles exhibit properties that are attractive for microwave applications, such as a broad frequency bandwidth and higher working frequencies when compared with bulk ferrimagnetic oxides. In this thesis, the dynamical properties of ferromagnetic spherical shells are studied using a combination of analytical and numerical methods, to further understanding and enhance the permeability of these materials towards higher frequencies. Using linearised micromagnetic equations, saturated spherical shells are investigated in the exchange-dominated regime when assuming that surface anisotropy is present at both the inner and outer boundaries. This configuration is amenable to exact solutions for the resonance eigenvalues and to investigate the size/thickness dependence of the resonance frequencies. It is found that the mode frequency can increase with decreasing shell thickness or is driven rapidly towards the ferromagnetic resonance frequency depending on the choice of the surface anisotropy constant at each boundary. Moreover, surface anisotropy introduces a dependence of the zeroth mode on shell thickness, removing the degeneracy with the ferromagnetic resonance and leading to a pronounced size dependence of this mode for thin shells. A generalised resonance theory is further outlined for a multilayered spherical nanoparticle comprised of exchange-coupled concentric layers. It can be used to compute the resonance spectra of core-shell nanoparticles, as in the case of a solid spherical ferromagnetic core surrounded by an outer oxide shell.

Detailed micromagnetic modelling of two- and three-dimensional ferromagnetic particles was carried out to study the role of long-range magnetostatic interactions between concentric rings and the influence of realistic domain structures on the dynamic susceptibility. Micromagnetic modelling of such structures demonstrates that a family of higher-order flexural modes is present for spherical shells relaxed into the vortex state, which can reach high-frequencies 20-25 GHz under weak-field excitations. These simulations provide an alternative and more plausible interpretation of observed high-frequency resonance modes in measured permeability spectra of spherical shell particle composites, and aid in the design of high-frequency, light-weight composite materials. The dynamical properties of three-dimensional permalloy elements supporting vortex domain structures were also investigated with micromagnetic simulations and compared with experiment. This is to study the influence of non-uniform field gradients and three-dimensional static magnetisation configurations on

the dynamical behaviour. It is found that the permalloy elements support domain walls with perpendicular out-of-plane components which can be switched dynamically in response to specific magnetic pulse parameters.

This project further aimed to incorporate the fundamental nonlinear micromagnetic and electromagnetic details, including exchange and magnetocrystalline anisotropy, within the finite-difference time-domain (FDTD) method. This is to study the interaction between magnetic materials and electromagnetic waves in the presence of current and magnetic sources at microwave frequencies. Results are presented for conducting semi-infinite permalloy pillars in the micrometer and sub-micrometer size range. It is found that microwave absorption results primarily from edge modes localised at the boundaries of the pillar in accordance with the skin depth, which appear at a lower frequency than the ferromagnetic resonance.

Acknowlegements

I wish to thank various people for their contribution to this project. Foremost, I would like to express my sincere gratitude to my supervisors Dr Mustafa Aziz and Dr Feodor Ogrin for their continuous support of my PhD study, and for their guidance, motivation and knowledge. I would also like to extend my thanks to Professor Alastair Hibbins and Professor Roy Sambles for countless fruitful discussions, and for their continuous encouragement, insight and enthusiasm.

My deep thanks are extended to Dr Feodor Ogrin for providing the opportunity to partake in research at the ESRF (European Synchrotron Radiation Facility), and I am grateful to all of those with whom I have had the pleasure to collaborate with during this project.

I also gratefully acknowledge the Engineering and Physical Sciences Research Council (EPSRC) of the United Kingdom for providing funding via the Centre for Doctoral Training (CDT) in Metamaterials (Grant No. EP/L015331/1), without which this research would not have been possible.

I am also profoundly thankful to my family for their wise counsel and encouragement throughout my life. Finally, I would like to extend a heartfelt thank you to my partner Marziyeh Belal, for all her love and support throughout my PhD.

Contents

1 Introduction **8**

2 Theory and Background **15**

2.1 Maxwell's equations 15

2.1.1 Wave equation 16

2.1.2 Skin depth 17

2.2 Ferromagnetism 19

2.2.1 Exchange interaction 20

2.2.2 Static energy terms 25

2.2.2.1 Magnetostatic energy 25

2.2.2.2 Exchange energy 27

2.2.2.3 Zeeman energy 28

2.2.2.4 Magnetocrystalline anisotropy 29

2.2.2.5 Surface anisotropy 30

2.3 Critical sizes and domains 31

2.3.1 Equilibrium configurations 31

2.3.2 Domain walls 35

2.4 Hysteresis 37

2.4.1 Nucleation 37

2.4.1.1 Coherent rotation 40

2.4.1.2 Curling 40

2.4.2 Stoner-Wohlfarth model 43

2.5 Ferromagnetic resonance 44

2.5.1 Equation of motion 45

2.5.1.1 Damping 47

2.5.1.2 Conservation of magnetisation 49

2.5.1.3 Energy decay 49

2.5.2 Uniform resonance 50

2.5.3 Magnetostatic resonance . . . 53
2.5.4 Exchange resonance . . . 55
2.6 Summary . . . 58

3 Methodology **59**
3.1 Numerical micromagnetics . . . 60
3.2 Maxwell-Landau-Lifshitz-Gilbert formulation . . . 63
3.2.1 Coupled equations . . . 64
3.2.2 Electromagnetic energy . . . 65
3.3 Numerical implementation . . . 67
3.3.1 Finite-difference time-domain (FDTD) method . . . 67
3.3.2 Maxwell's equations . . . 67
3.3.3 Numerical integration of the LLG equation and FDTD-LLG iterative algorithm . . . 70
3.3.4 Numerical stability . . . 74

4 Exchange resonance in multilayered spherical particles **78**
4.1 Introduction . . . 78
4.2 Surface anisotropy . . . 80
4.3 Shell thickness . . . 85
4.4 Size dependence . . . 87
4.5 Multilayered particles . . . 88
4.6 Summary . . . 91

5 Dynamic susceptibility of concentric rings **93**
5.1 Introduction . . . 93
5.2 Hysteresis . . . 95
5.3 Ring width . . . 98
5.4 Ring separation . . . 100
5.5 Summary . . . 103

6 Role of domain structure in microwave absorption **104**
6.1 Introduction . . . 104
6.2 Onion domain . . . 106
6.3 Vortex domain . . . 111
6.4 Chiral domain . . . 116
6.5 Summary . . . 120

7 Three-dimensional domain wall dynamics in permalloy films 122
7.1 Introduction 122
7.2 Static magnetisation 123
7.3 Core gyration 124
7.4 External bias field 130
7.5 Summary 133

8 Wave propagation in metallic structures 134
8.1 Introduction 134
8.2 Plane wave excitation 137
8.3 Magnetisation dynamics 140
8.4 Reflection loss 143
8.5 Summary 144

9 Summary and future work 146
9.1 Summary 146
9.2 Future work 149

Bibliography 150

Journal Publications

McKeever, C., Ogrin, F. Y., and Aziz, M. M. (2018) Influence of surface anisotropy on exchange resonance modes in spherical shells. *Journal of Physics D: Applied Physics*, **51**, 305003.

McKeever, C., Ogrin, F. Y., and Aziz, M. M. (2019) Microwave magnetization dynamics in ferromagnetic spherical nanoshells. *Physical Review B* (accepted for publication).

Gallagher, C., et al. (2019) A broadband stripline technique for characterizing relative permittivity and permeability. *IEEE Transactions on Microwave Theory and Techniques* (accepted for publication).

McKeever, C., Ogrin, F. Y., and Aziz, M. M. (2017) Dynamic susceptibility of concentric permalloy rings with opposite chirality vortices. *Journal of Applied Physics* **67**, 203901.

Bukin, N., et al. (2016) Time-resolved imaging of magnetic vortex dynamics using holography with extended reference autocorrelation by linear differential operator. *Scientific Reports* **6**, 36307.

Bukin, N., et al. Time-resolved and field-dependent imaging of double-Landau magnetic state using x-ray holography with extended reference autocorrelation by linear differential operator. *In preparation.*

Aziz, M. M., and McKeever, C. Wave propagation in conducting ferromagnetic prisms. *In preparation.*

McKeever, C. Magnetic resonance in concentric multilayered spherical particles. *In preparation.*

McKeever, C., Ogrin, F. Y., and Aziz, M. M. Wideband magnetisation dynamics due to chiral domain walls in ferromagnetic shells. *In preparation.*

Chapter 1

Introduction

High-frequency dynamics of magnetic materials has been the focus of intense research in recent years [1], driven by the continuing demand for smaller and faster magnetic devices in high density storage media, magnetic field sensors and microwave devices. Structured ferromagnetic metal-based materials display remarkable dynamical properties which can differ markedly from their bulk counterparts [2, 3]. The origin of this difference is the fact that in fine particles surface and exchange effects are not at all negligible, in contrast with bulk materials [4, 5]. Composites comprised of these magnetic materials are characterised by a non-zero imaginary component of the permeability, which stems from a gyromagnetic resonance phenomenon occurring in the microwave frequency range. A detailed understanding of the high-frequency response of such ferromagnetic materials is of primary interest. However, calculation of the dynamic susceptibility can only be achieved with conventional analytical methods for highly simplified systems. This is because the primary features of the resonance spectra depend strongly on the static magnetisation configuration, in addition to the gradient and orientation of the excitation field [6]. Hence, accurate determination of the dynamic susceptibility spectra for nano- and sub-micrometer scale ferromagnetic particles supporting inhomogeneous magnetisation configurations is a central topic of this thesis.

Numerical micromagnetics can predict quantitatively the static magnetisation distribution in ferromagnetic materials [7], and is an appropriate method for inves-

tigating the high-frequency properties of nano- and sub-micrometer particles with inhomogeneous internal domain structures. Several methods exist for computing the dynamic susceptibility spectra of ferromagnetic materials with complex domain configurations, which can be categorized into frequency and time domain methods. In the frequency domain approach the static configuration is first computed using an iterative method [8]. The Landau-Lifshitz-Gilbert (LLG) equation of magnetisation motion is then linearised about the stable magnetisation configuration and the dynamic susceptibility is solved by means of a complex dense linear system, assuming a harmonic time dependence for the weakly excited magnetisation. In the time-domain approach, the LLG equation is integrated directly with respect to time in the presence of a weak time-varying excitation field, where the specific parameters of the field are user-defined. The Fourier analysis of the time domain data can then be used to calculate the primary details of the susceptibility spectra, namely the linewidth, frequency and intensity of the resonances, in addition to the spatial distribution of the susceptibility throughout the material. This technique has been widely used to study the dynamic susceptibility spectra of both homogeneous and inhomogeneous domain structures [9, 10, 11, 12] and is adopted in this thesis.

In recent years, three-dimensional magnetisation dynamics has become a subject of general interest in the field of nanomagnetism [13]. This recent trend has been stimulated by rapid advancements in chemical synthesis and nanotomography techniques, in addition to new computational methods. The extension of 2D nanostructures into 3D leads to the emergence of more complex magnetic configurations, many with outstanding magnetic properties. For example, the presence of curvature in shells brings about an effective curvature-induced anisotropy and an effective Dzyaloshinskii-Moriya interaction (DMI) [14, 15]. This curvature-induced anisotropy and effective DMI gives rise to a rich diversity of static and dynamic behaviour, in addition to polarity-chirality coupling [16] and curvature-driven magnetochirality [17]. The chiral symmetry of the magnetic vortex, which is intrinsically degenerate

in 2D nanomagnets, can be broken by 3D geometries. Recent micromagnetic studies of cylindrical nanowires and nanotubes have shown that domain walls with an axial vortex configuration can overcome the Walker breakdown due to a break in the chiral symmetry induced by the surface curvature [18]. By tailoring the geometry of curved elements these magnetochiral effects can lead to novel functionalities and devices, with a wide range of unique physical properties.

Magnetic composites employing curved structures have garnered significant interest in advanced and emerging magnetic technologies including ultrahigh-density magnetic data storage, microwave devices and materials for communications, electromagnetic compatibility/interference and deference applications, and next generation of low loss, high-power density electrical machines and devices. This interest evolved with the ability to fabricate fine magnetic particles with small dimensions, controlled magnetic properties and narrow particle size distributions. Independent control over these intrinsic particle characteristics enable the tuning and the engineering of lightweight, compact and high-frequency magnetic composites. However there is currently limited understanding of the resonance mechanisms responsible for enhancing the high-frequency response of magnetic composites, and of the correlation between the intrinsic particle attributes and the high-frequency resonance modes in composites. Experimental work on fine particle assemblies [3, 19, 20, 21] indicated the presence of high-frequency resonance modes attributed to exchange resonances [22] and surface effects [23] but with size dependences and modes that deviate from exchange resonance theory on saturated particles [24]. The micromagnetic studies also ignored the effects of the metallic nature of the particles and corresponding Eddy current effects resulting from the interaction with electromagnetic waves experienced during operation.

This theoretical research programme aimed to unravel the potential resonance mechanisms and modes in sub-micrometer metallic magnetic particles, and identify the correlation between the resonance modes and particle attributes under high-

frequency magnetic field and electromagnetic wave excitations. This is to enable the design and engineering of advanced magnetic composites for microwave materials and devices with extended high-frequency response. This involved new developments in the analytical theory of ferromagnetic resonance in single and multi-shell magnetic particles to understand the size dependence of these structures in the saturated regime. Detailed numerical micromagnetic models of 3D nanometer multi-shell structures were developed using MuMax3 and simulations of nanosecond pulse field excitations were carried out for different relaxed ground states. This is to evaluate the validity of the analytical micromagnetics, identify the resonance mechanism in practicable and non-saturated particles and investigate potential magnetic configurations for enhancing the resonance frequencies. An efficient numerical algorithm for combining micromagnetics and electromagnetics based on the finite-difference time-domain (FDTD) method was developed to fully simulate the complex electromagnetic wave interaction with metallic magnetic structures and study the excited resonance modes.

Chapter 2 - Background

Chapter 2 introduces the relevant background concepts of magnetism for this thesis. This chapter briefly reviews Maxwell's equations and the origins of spontaneous magnetisation in ferromagnetic materials, with particular attention to the quantum mechanical exchange interaction. The micromagnetic energy terms are then introduced and the critical sizes and reversal properties of spherical particles are discussed. This chapter closes with a discussion of the dynamical properties of spherical ferromagnetic particles in the micrometer, sub-micrometer and nanometer size ranges.

Chapter 3 - Theory and methodology

Chapter 3 introduces the numerical methodology used throughout this thesis. The

energy terms used in micromagnetic solvers are introduced and the general properties of the discretized Landau-Lifshitz-Gilbert equation of magnetisation motion are discussed. Finally, a generalised electromagnetic-micromagnetic approach which incorporates the complete solution of Maxwell's equation is presented. Simplified analysis of numerical stability of the FDTD-LLG algorithm is discussed.

Chapter 4 - Exchange resonance in multilayered spherical particles

In Chapter 4, the dynamical properties of saturated spherical shells are investigated analytically in the exchange-dominated regime when assuming that surface anisotropy is present at both the inner and outer boundaries. This is to provide detailed understanding into the high-frequency dynamics for an idealised shell, before moving onto more detailed micromagnetic computations. The theory is generalized to a core-shell particle in the final section of this chapter, however the method of solution is applicable to a concentric spherical particle with an arbitrary number of shells.

Chapter 4 - Dynamic susceptibility of concentric rings

In Chapter 5, the high-frequency dynamic behaviour of concentric permalloy nanorings supporting vortex domain structures is investigated by micromagnetic simulations. The aim is to explore the dynamic susceptibility of the concentric ring structure as a function of geometric parameters of the system, with consideration of long-range magnetostatic interactions. This serves as foundation for more complex numerical work involving three-dimensional spherical structures.

Chapter 6 - Role of domain structure in microwave absorption

In Chapter 6, the dynamical properties of spherical shells are investigated when

supporting fully three-dimensional domain configurations. This is to uncover potential resonance mechanisms and modes in sub-micrometer metallic magnetic particles, and identify their intrinsic resonant behaviour. The dynamic susceptibility of saturated shells is computed and compared with analytical predictions. The dynamic susceptibility of ferromagnetic spherical shells with vortex domain structure is also investigated in the sub-micrometer and nanometer size range. Finally, the dynamic susceptibility response of a chiral magnetisation texture is computed and the full mode spectrum is mapped out.

Chapter 7 - Three-dimensional domain wall dynamics in permalloy films

In Chapter 7, the dynamical properties of relatively thick ($\approx$ 80 nm) permalloy elements supporting a vortex domain structure are investigated with numerical micromagnetic simulations, and compared with experiment. This is to study the three-dimensional character of the static magnetisation configuration and its impact on the dynamical properties. The role of an external DC field on the static behaviour is also briefly investigated. This work is a collaborative effort of several people. The individual contributions can be found in the relevant publication [25].

Chapter 8 - Wave propagation in metallic elements

In Chapter 8, a hybrid electromagnetic and micromagnetic method is proposed based on the finite-difference time-domain (FDTD) Maxwell's equation framework, offering numerical efficiency and stability for solving the complex system of the combined Landau-Liftshitz-Gilbert (LLG) and Maxwell's equations. In this chapter, the FDTD-LLG algorithm is extended to model electromagnetic wave interaction with metallic magnetic nano-structures. The results indicate the importance of the combined electromagnetic-micromagnetic numerical approach to account for Eddy current

screening and damping inside the magnetic material, and to enable the inclusion of the full micromagnetic details in the dynamic permeability of the material.

Chapter 2

Theory and Background

2.1 Maxwell's equations

James Clerk Maxwell published the first unified theory of electromagnetism with a set of fours equations which state the fundamentals of electricity and magnetism. The theory combined all previously known results in electromagnetism and led to the prediction of electromagnetic waves. The four equations in differential and integral forms are given by

$$\nabla \cdot \mathbf{D} = \rho_v \qquad \oint \mathbf{D} \cdot \mathbf{S} = \oint_v \rho_v dv \tag{2.1}$$

$$\nabla \cdot \mathbf{B} = 0 \qquad \oint \mathbf{B} \cdot d\mathbf{S} = 0 \tag{2.2}$$

$$\nabla \times \mathbf{E} = -\frac{\partial \mathbf{B}}{\partial t} \qquad \oint_L \mathbf{E} \cdot d\mathbf{L} = -\frac{\partial}{\partial t} \int_S \mathbf{B} \cdot d\mathbf{S} \tag{2.3}$$

$$\nabla \times \mathbf{H} = \mathbf{J} + \frac{\partial \mathbf{D}}{\partial t} \qquad \oint_L \mathbf{H} \cdot d\mathbf{L} = \oint_S \left(\mathbf{J} + \frac{\partial \mathbf{D}}{\partial t} \right) \cdot d\mathbf{S} \tag{2.4}$$

where ρ_v is the electric charge density, J is the electric current density, $\mathbf{E}$ is the electric field, $\mathbf{B}$ is the magnetic field and $\mathbf{D}$ is the electric flux density and t is time.

The continuity equation follows from equation (2.4)

$$\nabla \cdot \mathbf{J} = -\frac{\partial \rho_v}{\partial t} \tag{2.5}$$

To equations (2.1) - (2.4) and (2.5) one should add the constitutive relations for a linear, homogeneous and isotropic medium

$$\mathbf{D} = \epsilon \mathbf{E} = \epsilon_0 \mathbf{E} + \mathbf{P} \tag{2.6}$$

$$\mathbf{B} = \mu \mathbf{H} = \mu_0 (\mathbf{H} + \mathbf{M}) \tag{2.7}$$

$$\mathbf{J} = \sigma \mathbf{E} + \frac{\partial \mathbf{D}}{\partial t} \tag{2.8}$$

where ϵ is the permittivity of free space, $\mathbf{P}$ is the polarisation vector, μ_0 is the permeability of free space, $\mathbf{H}$ is the magnetic field, $\mathbf{M}$ is the magnetisation and σ is the conductivity.

2.1.1 Wave equation

Maxwell's curl equations in differential form are first order coupled equations, where both the electric $\mathbf{E}$ and magnetic $\mathbf{H}$ fields appear in each equation. However, it is often convenient to express these equations as second-order differential equations and solve for the electric or magnetic field components separately. Taking the curl of both sides of equation (2.3) and (2.4) we have

$$\nabla \times \nabla \times \mathbf{E} = \mu \nabla \times \left(\frac{\partial \mathbf{H}}{\partial t} \right) = -\mu \frac{\partial}{\partial t} (\nabla \times \mathbf{H}) \tag{2.9}$$

$$\nabla \times \nabla \times \mathbf{H} = \nabla \times \left(\mathbf{J} + \frac{\partial \mathbf{D}}{\partial t} \right) = \sigma \nabla \times \mathbf{E} + \epsilon \frac{\partial}{\partial t} (\nabla \times \mathbf{E}) \tag{2.10}$$

Substituting equation (2.4) into (2.9) and using the vector identity $\nabla \times \nabla \times \mathbf{A} = \nabla(\nabla \cdot \mathbf{A}) - \nabla^2 \mathbf{A}$ leads to an expression in terms of the electric field only, namely

$$\nabla(\nabla \cdot \mathbf{E}) - \nabla^2 \mathbf{E} = -\mu\sigma \frac{\partial \mathbf{E}}{\partial t} - \mu\epsilon \frac{\partial^2 \mathbf{E}}{\partial t^2} \tag{2.11}$$

where ϵ and μ correspond to a linear, homogeneous and isotropic material. For a source free region $\rho_v = 0$ the wave equation reduces to

$$\nabla^2 \mathbf{E} = \mu\sigma \frac{\partial \mathbf{E}}{\partial t} + \mu\epsilon \frac{\partial^2 \mathbf{E}}{\partial t^2} \tag{2.12}$$

Using a similar argument, it can be shown that the wave equation for the magnetic field is given by

$$\nabla^2 \mathbf{H} = \mu\sigma \frac{\partial \mathbf{H}}{\partial t} + \mu\epsilon \frac{\partial^2 \mathbf{H}}{\partial t^2} \tag{2.13}$$

When the material is also lossless ($\sigma = 0$) then the wave equations take the form

$$\nabla^2 \mathbf{E} = \mu\epsilon \frac{\partial^2 \mathbf{E}}{\partial t^2} \tag{2.14}$$

$$\nabla^2 \mathbf{H} = \mu\epsilon \frac{\partial^2 \mathbf{H}}{\partial t^2} \tag{2.15}$$

2.1.2 Skin depth

Skin effect is the tendency of an alternating electric current to become distributed within a conductor. The electric current flows primarily at the surface (or 'skin') of the conductor, and penetrates into the conductor to a depth known as the *skin depth*. The skin depth decreases with increasing frequency and reduces the effective cross-section of a conductor by causing the effective resistance to increase at higher frequencies. Without loss of generality, let us restrict the solution to the electric field $\mathbf{E}$. Assume that a plane wave with electric field $\mathbf{E}_x$ and magnetic field $\mathbf{H}_y$ is

propagating in the z-direction,

$$\mathbf{E}_x \propto e^{j\omega t - \gamma_0 z} \tag{2.16}$$

where ω is the frequency and γ_0 is the propagation constant. Substituting (2.16) into (2.11) leads to

$$\gamma = \alpha + j\beta = \pm\sqrt{-\omega^2\mu\big(\epsilon - j\frac{\sigma}{\omega}\big)} \tag{2.17}$$

where γ and α are the propagation and attenuation constants, respectively. Here, the propagation constant and attenuation constant should not be confused with the gyromagnetic ratio and damping constant. By taking the square of equation (2.17) and equating the real and imaginary components, the attenuation and phase constants can be expressed

$$\alpha = \omega\sqrt{\mu\epsilon}\left(\frac{1}{2}\sqrt{1+\left(\frac{\sigma}{\omega\epsilon}\right)^2} - 1\right)^{1/2} \tag{2.18}$$

and

$$\beta = \omega\sqrt{\mu\epsilon}\left(\frac{1}{2}\sqrt{1+\left(\frac{\sigma}{\omega\epsilon}\right)^2} + 1\right)^{1/2} \tag{2.19}$$

for a travelling wave which is propagating in the z-direction. The skin depth δ is given by

$$\delta = \frac{1}{\alpha} \tag{2.20}$$

When the lossy material considered is a good conductor, the skin depth can be well approximated by the expression

$$\delta = \sqrt{\frac{2}{\omega\mu\sigma}} \tag{2.21}$$

The equation describes a decay of the field $\mathbf{E}$ with a characteristic distance given by the real part of $1/\sqrt{j\omega\mu(\sigma + j\omega\epsilon)}$. The real component approaches zero as σ approaches infinity, and thus the electric field must be zero everywhere inside an ideal conductor.

2.2 Ferromagnetism

Maxwell's equation play a central role in the description of microwave magnetic materials. For ferromagnetic materials, which are a central focus of this thesis, the strongly coupled atomic dipole moments tend to have a parallel alignment at sufficiently low temperatures. As a result, ferromagnetic materials exhibit spontaneous magnetisation which can be present even in the absence of a magnetic field. Some examples of room-temperature ferromagnetic materials are Fe, Ni, Co and their alloys. For such materials a paramagnetic behaviour is observed above a critical temperature known as the Curie temperature. A ferromagnetic material may still exhibit no magnetic moment at temperatures below the Curie temperature despite the tendency for the atomic dipole moments to align in a parallel fashion. However, after application of a small magnetic field, the ferromagnetic material will produce a magnetic moment which is orders of magnitude larger than paramagnetic materials.

Weiss introduced an internal field in order to describe the spontaneous alignment of the magnetic moments in a ferromagnetic material. This postulated field, known as the *Weiss field*, is proportional to the spontaneous magnetisation, such that

$$H_W = N_W M \tag{2.22}$$

where H_W is the Weiss field, N_W is the molecular field constant and M is the spontaneous magnetisation. The total magnetic field, neglecting the demagnetizing and Lorentz fields, can then be written

$$H = H_0 + N_W M, \tag{2.23}$$

where H_0 is the externally applied magnetic field. Here it should be noted that the constant N_W is of the order of magnitude $N_W = H_W/M \approx 10^4$ which is significantly larger than the Lorentz factor $4\pi/3$. To first order the temperature dependence of

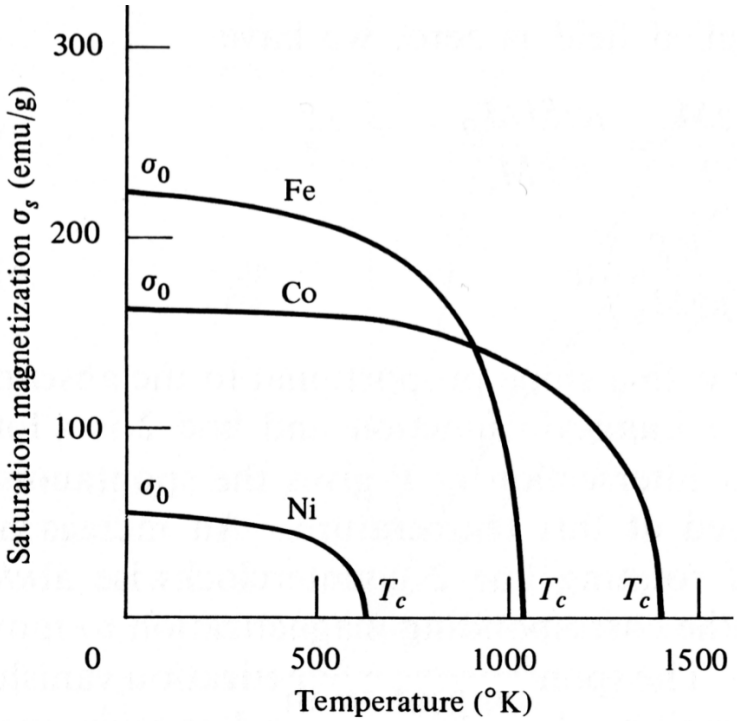

Figure 2.1: Plot of the saturation magnetisation against the temperature for iron, cobalt and nickel. Reproduced from *"Introduction to Magnetic Materials"*, B.D. Cullity (1972).

the magnetisation of a ferromagnetic material is given by the expression

$$M(T) = M(0)(1 - T/T_c)^{3/2} \tag{2.24}$$

where $M(0)$ is the spontaneous magnetisation at absolute zero and T_c is the Curie temperature. The saturation magnetisation as a function of temperature is shown in Figure 2.1 for iron, cobalt and nickel.

2.2.1 Exchange interaction

The nature of the Weiss field was unclear until the advent of quantum mechanics. Heisenberg developed a theory based on the Heitler-London method which showed that the molecular field postulated by Weiss was a result of the quantum mechanical exchange interaction. Consider two electrons moving in the potential fields $V(\vec{r}_1)$ and

$V(\vec{r}_2)$, where $\vec{r}_1$ and $\vec{r}_2$ are the electron coordinates. When interaction between the electrons is neglected, the system can be described by the Schrödinger equation

$$\Big(-\frac{\hbar^2}{2m}\Big(\nabla_1^2 + \nabla_2^2 + V(\vec{r}_1) + V(\vec{r}_2)\Big)\Big)\Phi = E\Phi \tag{2.25}$$

where the subscripts 1 and 2 refer to the two electrons, Φ is the electron wave function, m is the electron mass, V is the potential energy and E is the total energy. It is readily seen by substitution that two solutions for the wave function Φ are given by

$$\Phi_I = \Phi_a(1)\Phi_b(2) \tag{2.26}$$

and

$$\Phi_{II} = \Phi_a(2)\Phi_b(1) \tag{2.27}$$

where $E = E_a + E_b$ in each case. The wave functions $\Phi_a(1)$ and $\Phi_b(2)$ represent electron 1 in state a and electron 2 in state b, respectively. Conversely, $\Phi_a(2)$ and $\Phi_b(1)$ are the wave functions when electrons 1 and 2 are interchanged. The requirement that each electron is indistinguishable leads to the condition

$$|\Phi(1,2)|^2 d\vec{r}_1 d\vec{r}_2 = |\Phi(2,1)|^2 d\vec{r}_1 d\vec{r}_2 \tag{2.28}$$

where the wave function $\Phi(1,2)$ describes the two-electron system and the wave function $\Phi(2,1)$ represents interchanged electrons. Two different cases result from equation (2.28)

$$\Phi(1,2) = +\Phi(2,1) \tag{2.29}$$

or

$$\Phi(1,2) = -\Phi(2,1) \tag{2.30}$$

which are known as symmetrical (2.29) and anti-symmetrical (2.30) wave functions. The solutions (2.26)-(2.27) lack these properties and cannot be taken as legitimate

solutions as a result. This can be resolved by replacing (2.26)-(2.27) with a set of linear combinations

$$\Phi_{sym}(1,2) = \frac{1}{\sqrt{2}}(\Phi_a(1)\Phi_b(2) + \Phi_a(2)\Phi_b(1)) \tag{2.31}$$

and

$$\Phi_{anti}(1,2) = \frac{1}{\sqrt{2}}(\Phi_a(1)\Phi_b(2) - \Phi_a(2)\Phi_b(1)) \tag{2.32}$$

where $1/\sqrt{2}$ is a normalising constant. From the Pauli exclusion principle, the probability that two electrons will be in the same state is zero. As a result, electrons always have wave functions which are antisymmetric.

The single-electron wavefunctions depend on both the spatial coordinate and intrinsic spin. When the orbital motion is quenched, the one-electron wave functions can be expressed in the form

$$\Phi = \psi(\mathbf{r})\chi \tag{2.33}$$

where χ is a function of the spin coordinates only and $\psi(\mathbf{r})$ represents the solution of a Schrodinger equation for an electron with no spin. In the two-electron case, the antisymmetrical wave functions of the electrons can have either two forms

$$\Phi_{sym}(1,2)\chi_{anti}(1,2) \tag{2.34}$$

or

$$\Phi_{anti}(1,2)\chi_{sym}(1,2), \tag{2.35}$$

where the spatial coordinate is represented by $\Phi_{sym}(1,2)$ and $\Phi_{anti}(1,2)$ for the symmetrical and antisymmetrical wave functions, respectively. The symmetrical and antisymmetrical spin wave functions are expressed by $\chi_{sym}(1,2)$ and $\chi_{anti}(1,2)$, respectively. It is possible to express the wave functions of equations (2.34)-(2.35) in

terms of one-electron wave functions

$$\Phi_I = A\Big(\Phi_a(1)\Phi_b(2) + \Phi_a(2)\Phi_b(1)\Big)\Big(\chi_\alpha(1)\chi_\beta(2) - \chi_\alpha(2)\chi_\beta(1)\Big) \tag{2.36}$$

and

$$\Phi_{II} = B\Big(\Phi_a(1)\Phi_b(2) - \Phi_a(2)\Phi_b(1)\Big)\begin{pmatrix} \chi_\alpha(1) & \chi_\alpha(2) \\ \chi_\alpha(1)\chi_\beta(2)+ & \chi_\alpha(2)\chi_\beta(1) \\ \chi_\beta(1) & \chi_\beta(2) \end{pmatrix} \tag{2.37}$$

where A and B are normalising factors. Equation (2.36) represents anti-parallel alignment (singlet state) electron spins, whereas equation (2.37) represents parallel alignment (triplet state).

The electrostatic interaction between two hydrogen atoms with nuclei a and b is given by the Hamiltonian H_{12}

$$H_{12} = \frac{e^2}{r_{ab}} + \frac{e^2}{r_{12}} - \frac{e^2}{r_{1b}} - \frac{e^2}{r_{2a}}, \tag{2.38}$$

where the distance between nuclei is given by r_{ab}, the distance between electrons is r_{12} and the distance between a given nucleus and the electron on the other atom is given by r_{1b} and r_{2a}. The energy of the singlet ($S = 0$) and triplet ($S = 1$) states can be calculated as first order perturbations, where H_{12} is taken as the electrostatic perturbation of the two-electron system. The correction to the energy is then given by the standard expression

$$E = \int \Phi^* H_{12} \Phi dr \tag{2.39}$$

The energy of the singlet and triplet states can be calculating using equation (2.39) to give

$$E_I = A^2(K_{12} + J_{12}) \tag{2.40}$$

and

$$E_{II} = B^2(K_{12} - J_{12}), \tag{2.41}$$

where

$$K_{12} = \int \Phi_a^*(1)\Phi_b^*(2)H_{12}\Phi_a(1)\Phi_b(2)dt_1dt_2 \tag{2.42}$$

and

$$J_{12} = \int \Phi_a^*(1)\Phi_b^*(2)H_{12}\Phi_a(2)\Phi_b(1)dt_1dt_2. \tag{2.43}$$

where K_{12} is the average Coulomb interaction energy and J_{12} is the exchange integral. The exchange integral J_{12} is negative for the hydrogen molecule and as a result the spins are antiparallel in the ground state. However, ferromagnetic behaviour occurs when the exchange integral J_{12} is positive and the spins are aligned in parallel. The conditions which lead to a positive sign of J_{12} are discussed below.

Assume that $\Phi_a^*(1)\Phi_b^*(2)\Phi_a(2)\Phi_b(1)$ is positive, such that the wave functions Φ_a and Φ_b have no nodes in the regions where their overlap is significant. It is then possible to have a positive sign of J_{12} provided that the contributions from the positive terms exceed that of the negative terms in the Hamiltonian. For the Hamiltonian of equation (2.38) the term e^2/r_{12} is large when r_{12} is small, i.e. for wave functions which are large midway between the nuclei. The other terms $-e^2/r_{1b}$ and $-e^2/r_{2a}$ in equation (2.38) are smallest for wave functions which are small near the nuclei. This condition is satisfied when the interatomic spacing r_{ab} is large compared to the radii of the orbitals. As a consequence, the exchange integral J_{12} is most likely to be positive for d and f wave functions, as in the case of Fe, Ni and Co. Equations (2.36) and (2.37) can be expressed in the operator form

$$E = K - \frac{1}{2}J_{12} - 2J_{12}\boldsymbol{s_1} \cdot \boldsymbol{s_2}. \tag{2.44}$$

where $\boldsymbol{s_1} \cdot \boldsymbol{s_2}$ is the scalar product of two-spins. From equation (2.44) it may appear that neighbouring spins are directly coupled, however the interaction is electrostatic

in origin. The spin-dependent term of equation (2.44) is all that will be used in this thesis, because it is sufficient for typical ferromagnetic problems.

2.2.2 Static energy terms

Static micromagnetic models can be used to calculate the spatial distribution of the magnetisation of a ferromagnetic body at equilibrium by minimizing the total magnetic energy [26]. Equilibrium of the magnetisation configuration is reached when we have the condition

$$\mathbf{M} \times \mathbf{H}_{\text{eff}} = 0 \tag{2.45}$$

where $\mathbf{H}_{\text{eff}}$ is the total effective magnetic field. The total effective field can be expressed in terms of the functional derivative of the free energy density W with respect to the magnetisation

$$\mathbf{H}_{\text{eff}} = -\frac{\delta W}{\delta M} \tag{2.46}$$

where the free energy density W is comprised of the following terms

$$W = w_{ex} + w_z + w_{ms} + w_{ani} \tag{2.47}$$

and $w_{ex}, w_z, w_{ms}, w_{ani}$ are the exchange, Zeeman, magnetostatic and magnetocrystalline anisotropy energy contributions. The details of these energy terms are outlined below.

2.2.2.1 Magnetostatic energy

The magnetostatic field is a long-range dipole-dipole interaction between atomic moments within a ferromagnetic body. It is commonly known as the *demagnetising* field to reflect the fact that it tends to oppose the magnetisation of the magnetic material. In the magnetostatic approximation, the time variation of the electric field is neglected and the demagnetising field can be calculated using only two of Maxwell's

equations, namely

$$\nabla \times \mathbf{H} = j_f \quad \text{and} \quad \nabla \cdot \mathbf{H} = -\nabla \cdot \mathbf{M} \tag{2.48}$$

where j_f is the free current density and $\mathbf{H}$ is the magnetostatic field. The general solution of (2.48) can be expressed in terms of a 6-fold integral for the volume and surface magnetostatic charges

$$U(r) = -\int_{\text{volume}} \frac{\nabla' \cdot \mathbf{M(r')}}{|\mathbf{r} - \mathbf{r'}|} dV' + \int_{\text{surface}} \frac{\mathbf{n} \cdot \mathbf{M(r')}}{|\mathbf{r} - \mathbf{r'}|} dS' \tag{2.49}$$

where the integrals dV and dS are taken over the volume and surface of the ferromagnetic body, respectively. As this field involves two integrals which must be calculated over the entire volume and surface of the ferromagnetic material, calculation of the 6-fold integral (2.49) is the most computationally intensive part of numerical micromagnetics. The magnetostatic energy w_{ms} can be calculated from the expression

$$w_{ms} = -\frac{\mu_0}{2} \int_{volume} \mathbf{M} \cdot \mathbf{H} dV \tag{2.50}$$

where the integral dV is taken over the volume of the material. When the electric current density is zero, it is also possible to obtain a solution to eqns. (2.48) by solving the differential equations

$$H_d = -\nabla U \quad \text{and} \quad \nabla^2 U = \nabla \cdot \mathbf{M} \tag{2.51}$$

subject to the boundary conditions

$$U_{in} - U_{out} = 0 \tag{2.52}$$

$$\frac{\partial U_{in}}{\partial \mathbf{n}} - \frac{\partial U_{out}}{\partial \mathbf{n}} = \mathbf{M} \cdot \mathbf{n} \tag{2.53}$$

where U_{in} and U_{out} are scalar potentials inside and outside the ferromagnetic body and $\mathbf{n}$ is the surface normal. The potential outside the material must be regular at infinity

to ensure that the magnetic energy is finite. This approach is often more convenient for analytical work. However, the equations are only tractable for a limited number of cases, and often numerical computations are required to accurately calculate the demagnetising field.

The preference for the magnetisation to be oriented along a particular axis of a sample so that the magnetostatic energy can be minimised is called shape anisotropy. In the case of a spherical specimen with no preferred orientation, the same applied field will magnetise it to the same degree in any direction. However, in the case of a non-spherical structure, it will be easier to magnetise it along certain directions. In general, the field inside a uniformly magnetised ellipsoidal ferromagnet is itself uniform. As a result, it is possible to define the demagnetising field

$$\mathbf{H}_{in} = -N \cdot \mathbf{M} \tag{2.54}$$

where N is known the *demagnetising factor*. The demagnetising factor is a tensor which depends on the shape of the material. Extensive tabulation of this factor has been provided for ellipsoids, whereas volume and mid-plane averaged demagnetising factors are available for non-ellipsoidal geometries.

2.2.2.2 Exchange energy

In a ferromagnetic material neighbouring magnetic moments tend to align parallel to each other due to the quantum mechanical exchange interaction. For the purpose of numerical computations, the exchange energy can be approximated by a classical expression given by

$$E_{ex} = \frac{A}{M_s^2} \int_V \Big[(\nabla M_x)^2 + (\nabla M_y)^2 + (\nabla M_z)^2 \Big] dV \tag{2.55}$$

where A is the exchange constant representing the strength of the coupling between neighbouring spins and $\mathbf{M}$ represents the components of the magnetisation. It follows

from the condition $||\mathbf{M}||^2 = 1$ that $\mathbf{M} \cdot \partial\mathbf{M}/\partial x = \mathbf{M} \cdot \partial\mathbf{M}/\partial y = \mathbf{M} \cdot \partial\mathbf{M}/\partial z = 0$. Using the general relation $|\nabla f|^2 = \nabla \cdot (f\nabla f) - f\nabla^2 f$ equation (2.55) can be expressed as

$$E_{ex} = -\int_V A\mathbf{M} \cdot \left(\frac{\partial^2 \mathbf{M}}{\partial x^2} + \frac{\partial^2 \mathbf{M}}{\partial y^2} + \frac{\partial^2 \mathbf{M}}{\partial z^2} \right) dV. \tag{2.56}$$

Using the standard variational procedure, it can be shown [26] that the exchange effective field is given by

$$H_{ex} = \frac{2A}{\mu_0 M_s} \nabla^2 M_s \tag{2.57}$$

This approximation assumes that the exchange interaction is a nearest neighbour interaction, i.e. the wavefunctions of the electrons in the atoms of the ferromagnetic material only overlap with those of nearest neighbour atoms. Equation (2.57) further assumes that the angle between neighbouring atomic moments is small. Therefore, to obtain accurate numerical results it is important that the maximum spin angle is kept as small as possible in every region of the simulation grid. The exchange energy is minimised when neighbouring atomic moments align in the same direction, and an energy penalty is incurred when the angle between neighbouring moments increases.

2.2.2.3 Zeeman energy

The potential energy of a ferromagnetic sample in the presence of an external static magnetic field is known as the *Zeeman* energy. The magnetisation will tend to align with the external magnetic field in order to minimise the overall energy of the system. The potential energy increases when the magnetisation deviates from the direction of the external DC field. This increase in energy is proportional to the angle between the magnetisation and the field

$$w_Z = -\mathbf{M} \cdot \mathbf{H} \tag{2.58}$$

where w_Z is the Zeeman energy per unit volume, $\mathbf{M}$ is the magnetisation and $\mathbf{H}$ is the magnetic field, which can be static or time-varying.

2.2.2.4 Magnetocrystalline anisotropy

When an external field is applied to a ferromagnetic sample in different directions, the hysteresis of the material may vary depending on the orientation of the applied field. When this preferred direction is due to the principal axes of the crystal lattice, it is known as the magnetocrystalline anisotropy. This form of magnetic anisotropy originates from the spin-orbit interaction of electrons. Phenomenological expressions for the magnetocrystalline anisotropy energy can be obtained by expanding the anisotropy contribution as a power series in the direction cosines α, β and γ of the magnetisation vector $\mathbf{M}$, given by

$$\mathbf{M} = M_x i + M_y j + M_z k \tag{2.59}$$

$$\alpha = \frac{M_x}{||M_x||} \quad \beta = \frac{M_y}{||M_y||} \quad \gamma = \frac{M_z}{||M_z||} \tag{2.60}$$

To obtain simplified expressions for the purpose of numerical computations, the series expansion is normally truncated after the first two terms. The anisotropy of crystal systems with a single axis of high symmetry is known as uniaxial anisotropy. The uniaxial crystalline anisotropy energy can be represented by

$$E_{uniaxial} = K_{u0} + K_{u1} \sin^2 \theta + K_{u2} \sin^4 \theta + ... \tag{2.61}$$

where K_{u0}, K_{u1}, $K_{u2}, ...$ are the crystalline anisotropy energy constants, and θ is the angle between the anisotropy easy axis and magnetisation vector. The anisotropy energy is minimised when the magnetisation is aligned with the anisotropy easy axis, and maximised when the magnetisation is aligned along a hard axis. For a cubic

crystal, the anisotropy energy density E_{cubic} is given by

$$E_{cubic} = K_1(\alpha^2\beta^2 + \beta^2\gamma^2 + \gamma^2\alpha^2) + K_2\alpha^2\beta^2\gamma^2 \tag{2.62}$$

where the constants K_1 and K_2 are determined experimentally and vary with temperature. When the second term is negligible, the easy axes are the $< 100 >$ axes for $K_1 > 0$ and the $< 111 >$ directions for $K_1 < 0$. When K_2 is non-zero, the easy axes depend on both magnetocrystalline anisotropy constants K_1 and K_2. The effective anisotropy field can be calculated from the derivative of the energy density with respect to the magnetisation vector.

2.2.2.5 Surface anisotropy

Néel first recognised the importance of the reduced symmetry at the surface of a ferromagnet. The exchange energy in the bulk cannot be the same at the surface because the surface spins of a particle have nearest neighbours only on one side. When the surface is deposited with a non-magnetic layer the surface spins see a different environment again, as is the case at the interface between two different ferromagnetic layers. From a phenomenological perspective, any surface anisotropy term should reflect the tendency for the surface spins to lie either parallel or perpendicular to the surface, similar to thin films. As a result, the surface anisotropy energy term takes the form

$$E_s = \frac{1}{2}K_s \int (\mathbf{n} \cdot \mathbf{M})^2 dS \tag{2.63}$$

where $\mathbf{M}$ is the magnetisation, $\mathbf{n}$ is a unit vector parallel to the normal pointing out of the surface and the integration is taken over the surface of the material. The coefficient K_s is the surface anisotropy constant which can be measured experimentally or calculated from first principles using numerical computation.

2.3 Critical sizes and domains

2.3.1 Equilibrium configurations

The equilibrium magnetisation configuration of a ferromagnetic material is determined by the competition between the free energy parameters described in Section 2.2. In contrast with planar elements, the equilibrium states of ferromagnetic spheres always include two out-of-surface vortices with antipodal vortex cores [27]. The long-range magnetostatic interaction forces the magnetisation distribution to lie tangential to the surface by eliminating surface and volume magnetostatic charges, whereas the exchange interaction favours out-of-surface vortex cores to prevent anti-parallel alignment of spins. The skyrmion number determines the topological properties of a 3D vector field on a closed surface and depends on the polarities of the two vortex cores. For magnetically soft spherical shells, the vortex ground state is reached where one core is directed inward and another is directed outward the shell (see Figure 2.2). The ground state of the shell may be either meridional (vortex) or parallel (onion) depending on the geometrical and material properties.

In this section the discussion of ground states is limited to the single, 3D onion and vortex domains (see Figure 2.2) because they are part of the π_2-topological class which contains the energetically preferable states. Following Sloika et al. [27], these magnetisation configurations can be described by the shape function

$$f(\theta, \lambda) = \frac{\pi}{2}\left(\frac{e^{-\theta/\lambda} - e^{-\theta\,-\,\pi/\lambda}}{1 - e^{\pi/\lambda}}\right) \tag{2.64}$$

where θ is the polar angle and λ is the core-parameter which describes the core-size of a single vortex. It varies from an entirely in-surface vortex ($\lambda = 0$) to the single domain distribution ($\lambda = \infty$). When λ is non-zero and the polar angle is in the range $\pi/2 < \theta < \lambda$ the magnetisation is homogeneous (single domain) for a solid sphere and primarily tangentially orientated (onion domain) for a thin shell.

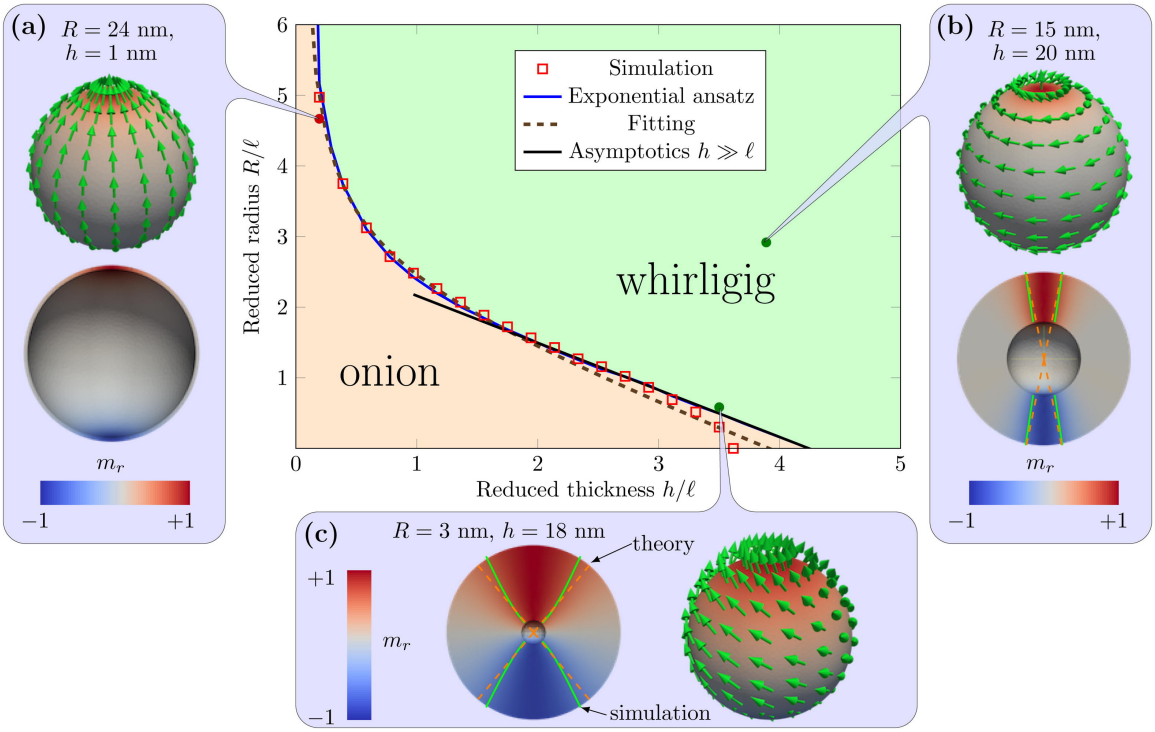

Figure 2.2: Phase diagram of equilibrium magnetisation structures in the spherical shell. Symbols correspond to the boundary between the onion and the whirligig states computed using micromagnetic simulations. Reproduced from [27].

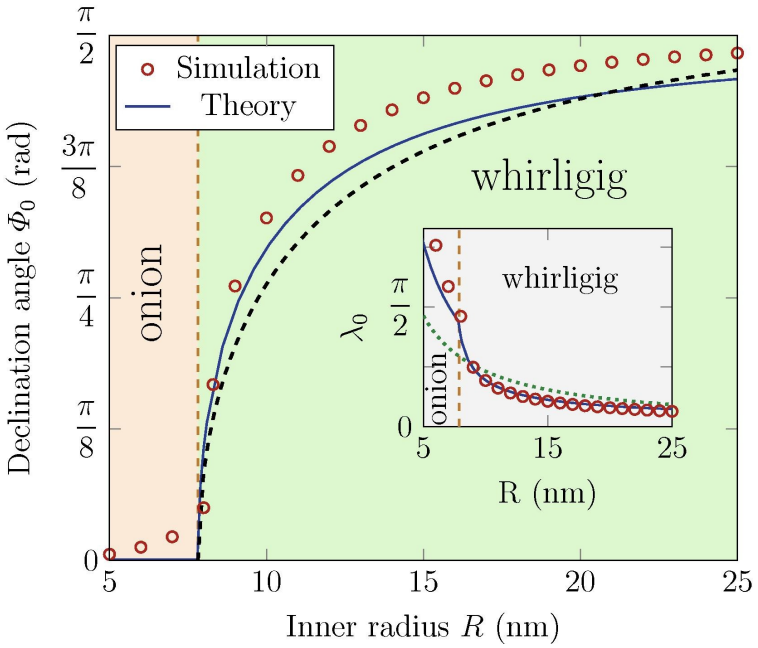

Figure 2.3: The declination angle as a function of inner radius for spherical shell with thickness $h = 10$ nm. Reproduced from [27].

The critical size of domain transitions in spherical particles can be calculated by considering the total energy of different states. For simplicity only the magnetostatic and exchange energy contributions will be considered here. The exchange energy can be calculated using the expressions provided in reference [14] for an arbitrary curved shell. The magnetostatic energy can be calculated by the Legendre polynomials technique used in previous studies [28].

$$\mathscr{E}(\epsilon,\omega;\lambda,\Phi) = \mathscr{E}(\epsilon,\omega;\lambda)+\mathscr{E}(\epsilon,\omega;\lambda)\sin^2(\frac{\Phi}{2}) + \mathscr{E}(\epsilon,\lambda)\sin^4(\frac{\Phi}{2}) \tag{2.65}$$

where ϵ is the ratio of the shell thickness h to the inner radius R, ω is the reduced exchange length and the parameter Φ is the declination angle which represents the slope of the magnetisation with respect the meridian direction. The reduced exchange length is written

$$\omega = l/R \tag{2.66}$$

where $l = \sqrt{A/4\pi M_s}$. Equilibrium magnetisation states can be found by minimiz-

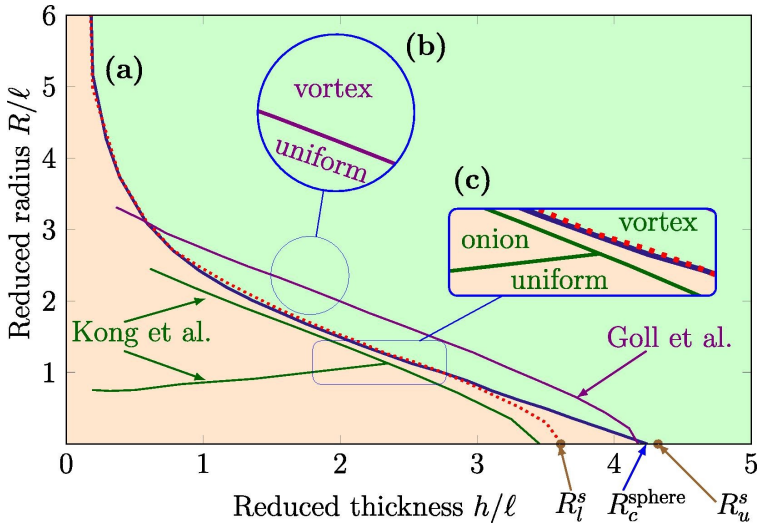

Figure 2.4: Equilibrium magnetisation states according to different models. Reproduced from [27].

ing the energy $\mathscr{E}$ with respect to the variational parameters, where the equilibrium condition of the core parameter λ must be evaluated numerically. This parameter is plotted in Figure 2.3 as function of the inner shell radius. For a planar disk the vortex core size is given by the expression $l^{disk} = \sqrt{2}l$ when $h \leq l$. This can be used to provide a reasonable estimate for the vortex core parameter size in a spherical shell. The vortex parameter of a planar disk is given by $\lambda^{disk} = l^{disk}/R = \omega\sqrt{2}$ which according to numerical simulations corresponds reasonably well with that of the thin shell (see Figure 2.3).

The critical curve separating onion and vortex domains can be calculated analytically in the limit of a thin shell or solid sphere. In the latter case it is possible to use the single domain limit. This leads to the equation [27]

$$\frac{R_c}{l} \approx 2\sqrt{2} - \frac{2}{3}\frac{h}{l} \tag{2.67}$$

This critical curve is represented by the solid line in Figure 2.2. In the other extreme

of a very thin shell the critical behaviour is described by the equation

$$\frac{R_c}{l} \approx 1.59\left(\frac{l}{h}\right)^{2/3} \tag{2.68}$$

It can be seen from (2.68) that for any given thickness h there always exists a critical radius R_c below which the onion state is the ground state. Similarly, there always exists some radius $R > R_c$ such that the vortex domain is the ground state (see Figure 2.4).

2.3.2 Domain walls

The minimum-energy state of bulk ferromagnets is normally comprised of multi-domains. At the interface between two domain regions, it is energetically favourable for spins to alter their direction gradually rather than abruptly. This leads to the formation of transition regions of finite length between any two domains. These transition regions are known as *domain walls* and are determined by the free energy parameters, in addition to local imperfections and the geometry of the ferromagnetic material. In a bulk ferromagnet the direction of the magnetisation within the domain wall changes such that the component of the magnetisation normal to the plane of the wall is constant [29]. Thus, the spins rotate about an axis perpendicular to the wall. These domain walls are known as *Bloch walls*. This occurs because the exchange energy cost would be very high if the variation in the magnetisation were abrupt between any two domains. The width of the domain wall is determined primarily by the competition between the exchange and anisotropy energy contributions. The exchange interaction tends to increase the width of the wall because a wider domain wall can accommodate a more gradual change in the magnetisation. However, this can result in an increase in the anisotropy energy if the direction of the spins are not aligned with the easy axis of the magnetocrystalline anisotropy. The specific wall energy of a Bloch wall γ_w is defined as the total energy per unit area of the wall,

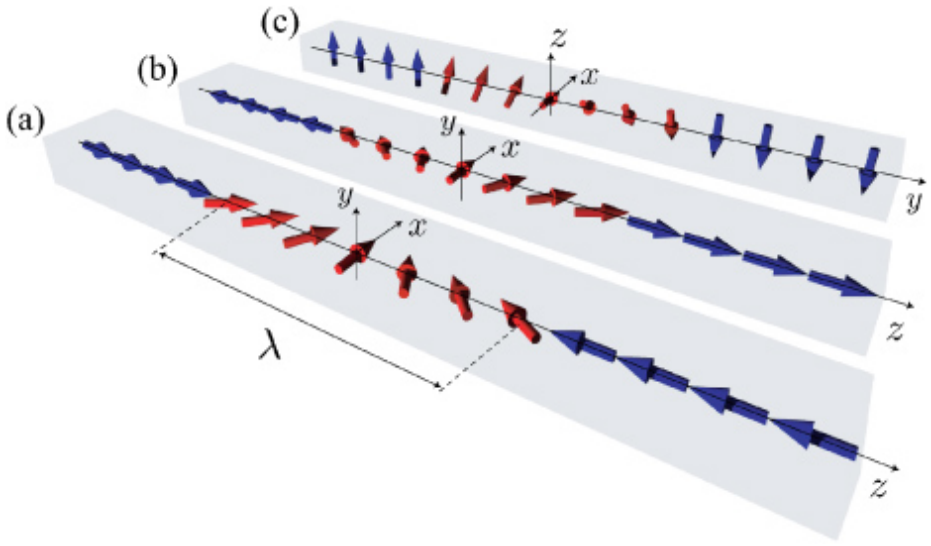

Figure 2.5: Schematic of magnetic domain wall. The arrows represent the magnetisation vector **M** for (a)-(b) Néel walls and (c) Bloch wall. Reproduced from [30].

given by the expression

$$\gamma_w = 4\sqrt{AK} \tag{2.69}$$

where A and K are the exchange and anisotropy constants, respectively. The most commonly used definition for the width of a Bloch domain wall δ_B is given by

$$\delta_B = \pi\sqrt{\frac{A}{K}} \tag{2.70}$$

The length scales lie in the range of $\delta_B \approx 100 - 1000$ nm and $\delta_B \approx 5$ nm for magnetically soft and hard materials, respectively. In the other extreme of a very thin film, it may be energetically favourable for the magnetisation to lie in plane rather than out of plane. In this situation the stray fields at the surfaces are only separated by a distance which is equal to the thickness of the film. As a result, the magnetisation will rotate about an axis which is perpendicular to the plane of the film leading to the formation of a *Néel wall*. For thin films the primary difference between these two kinds of domain walls is their dependence on film thickness. At a specific critical thickness the energy of the Néel wall becomes less than the energy of the Bloch wall and a transition between the two regimes occurs [29].

2.4 Hysteresis

In this section the concept of hysteresis in ferromagnetic materials is introduced, beginning with a discussion of the nucleation modes in ferromagnetic spheres. Nucleation theory describes the size ranges under which specific reversal mechanisms take place in ellipsoidal particles and has a close relationship to the dynamical equations which govern spherical particles. The curling and coherent rotation modes will be reviewed as they are the only possible reversal modes in a homogenous ferromagnetic sphere in the absence of surface anisotropy. In the final section of this chapter, the Stoner-Wohlfarth model is used to calculate the magnetic hysteresis loop of a single domain particle.

2.4.1 Nucleation

Consider a ferromagnetic material which is placed in a magnetic field that is sufficiently large to saturate the sample. Allow the magnetic field to be decreased slowly, in order to avoid dynamic effects. During this process, the sample will reach a point at which it is no longer stable along the initial direction of saturation. The point at which this instability begins is known as the *nucleation field*. The nucleation process can be studied by linearising Brown's differential equations which neglects the higher-order contributions to the magnetisation in directions perpendicular to the applied field. These linearised differential equations can be written [29]

$$\Big(C\nabla^2 - 2K_1 - M_s(H_a - N_z M_s)\Big)M_x = M_s\frac{\partial U_{in}}{\partial x} \tag{2.71}$$

and

$$\Big(C\nabla^2 - 2K_1 - M_s(H_a - N_z M_s)\Big)M_y = M_s\frac{\partial U_{in}}{\partial y} \tag{2.72}$$

inside the ferromagnetic body, where C is the exchange constant, H_a is the applied field and K_1 is the magnetocrystalline anisotropy constant. For simplicity, assume

that a homogeneous magnetic field is applied parallel to the major axis of an ellipsoid, which is also an easy axis of either cubic or uniaxial magnetocrystalline anisotropy. If z is chosen as the direction of the magnetic field, it is readily seen that to first order in M_x and M_y,

$$-\frac{\partial \omega_u}{\partial M_x} + \frac{M_x}{M_z}\frac{\partial \omega_c}{\partial M_z} = -2K_1 M_x, \tag{2.73}$$

where w_u and w_c are the uniaxial and volume magnetocrystalline anisotropy densities, respectively. The demagnetising field of a saturated ellipsoid is homogeneous and is given by the equations

$$H_x = -\frac{\partial U}{\partial x}, H_y = -\frac{\partial U}{\partial y}, \tag{2.74}$$

$$H_z = H_a - N_z M_s - \frac{\partial U}{\partial z}, \tag{2.75}$$

where N_z is the demagnetising factor in the z-direction for an ideally saturated ellipsoid and U is the potential at the point of nucleation, which is the order of M_x and M_y. The boundary conditions, in the absence of surface anisotropy, are given by

$$\frac{\partial M_x}{\partial n} = \frac{\partial M_y}{\partial n} = 0 \tag{2.76}$$

on the surface. Equations (2.71) and (2.72) need to be solved together with the boundary conditions (2.76) and the equations which define the potential U. To first order, the differential equations in this case are

$$\nabla^2 U_{in} = 4\pi M_s \left(\frac{\partial M_x}{\partial x} + \frac{\partial M_y}{\partial y} \right), \tag{2.77}$$

and

$$\nabla^2 U = 0, \tag{2.78}$$

with boundary conditions

$$U_{in} = U_{out} \tag{2.79}$$

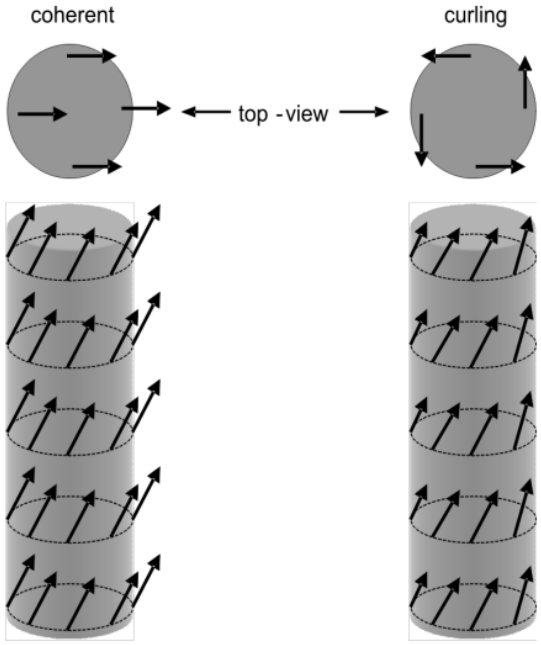

Figure 2.6: Schematic of magnetisation reversal by coherent rotation (left) and curling (right) in a long cylinder. Reproduced from [31].

and

$$\frac{\partial U_{in}}{\partial n} - \frac{\partial U_{out}}{\partial n} = 4\pi M_s \mathbf{M} \cdot \mathbf{n}, \tag{2.80}$$

on the surface, where the function for the potential is regular at infinity. It is necessary to solve these equations for the complete eigenvalue spectrum of the applied field H_a. However, only the largest nucleation field has any physical meaning, because smaller nucleation fields can never be reached during reversal of the magnetisation. Furthermore, it can be shown that only three reversal modes are possible for an ellipsoid of revolution, namely the *coherent rotation*, *curling* and *buckling* modes. A fourth reversal mode is strictly forbidden, because no other eigenvalue can ever lead to the largest value of the nucleation field H_a. The nucleation theory is important for determining the size ranges under which specific magnetisation reversal processes take place, and is a useful guide for numerical computations. As will be shown in later sections, the nucleation theory also has a close relationship to the dynamical equations which govern spherical particles.

2.4.1.1 Coherent rotation

If the components of the magnetisation M_x and M_y are constant then equation (2.76) is fulfilled, the volume change is zero and the equation for the potential becomes $\nabla^2 U = 0$ both inside and outside the ferromagnetic material. The problem is then reduced to that of a uniformly magnetized ellipsoid,

$$\frac{\partial U_{in}}{\partial x} = N_x M_s M_x \tag{2.81}$$

and

$$\frac{\partial U_{in}}{\partial y} = N_y M_s M_y, \tag{2.82}$$

where N_x and N_y are the demagnetizing factors. Equations (2.71) and (2.72) are then given by

$$\left(\frac{2K_1}{M_s} + H_a + (N_x - N_z)M_s\right)M_x = \left(\frac{2K_1}{M_s} + H_a + (N_y - N_z)M_s\right)M_y = 0 \tag{2.83}$$

reducing the nucleation problem to just two equations. For the saturated state, the components of the magnetisation which are orthogonal to applied field are zero $M_x = M_y = 0$ before nucleation. Nucleation occurs when either component of the magnetisation becomes non-zero. For this mode, the magnetisation reverses in unison and the rotation angle is the same everywhere inside the ferromagnetic body. Hence, this mode has been named *coherent rotation*. For the case of a sphere the demagnetizing factors are equal in all directions, leading to the nucleation field

$$H_n = -\frac{2K_1}{M_s} \tag{2.84}$$

2.4.1.2 Curling

For the curling mode, the magnetisation nucleates by forming a vortex configuration and the demagnetising field vanishes as a result. This particular reversal mode has a

close relationship to the exchange resonance condition in nanoparticles, which neglects the demagnetising field as a first approximation. In cylindrical coordinates ρ, z and ϕ, the curling mode is the solution of Brown's equations for the following constraints

$$M_x = -A(\rho, z)\sin\phi \tag{2.85}$$

$$M_y = A(\rho, z)\cos\phi \tag{2.86}$$

$$U_{in} = U_{out} = 0. \tag{2.87}$$

When transforming to spherical coordinates r, θ, ϕ, the linearised equations can be written

$$\left[C\left(\frac{\partial^2}{\partial r^2}+\frac{2}{r}\frac{\partial}{\partial r}+\frac{1}{r^2}\frac{\partial^2}{\partial\theta^2}+\frac{\cos\theta}{r^2\sin\theta}\frac{\partial}{\partial\theta}-\frac{1}{r^2\sin^2\theta}\right)-2K_1-M_s\left(H_a-\frac{1}{3}M_s\right)\right]A(r,\theta)=0 \tag{2.88}$$

where $N_z = 1/3$ for a sphere. The solution for the magnetisation in this case is given by

$$A \propto j_1(kr)\sin\theta \tag{2.89}$$

where j_1 is the spherical Bessel function of the first kind. The expression (2.89) is a solution of equation (2.88), provided that

$$CK^2 + 2K_1 + M_s\left(H_a - \frac{M_s}{3}\right) = 0. \tag{2.90}$$

and the boundary condition is satisfied if

$$\left(\frac{dj_1(kr)}{dr}\right)_{r=R} = 0, \tag{2.91}$$

where R is the radius of the sphere. Equation (2.91) has an infinite number of solutions, however only the smallest eigenvalue has a physical meaning. From equation

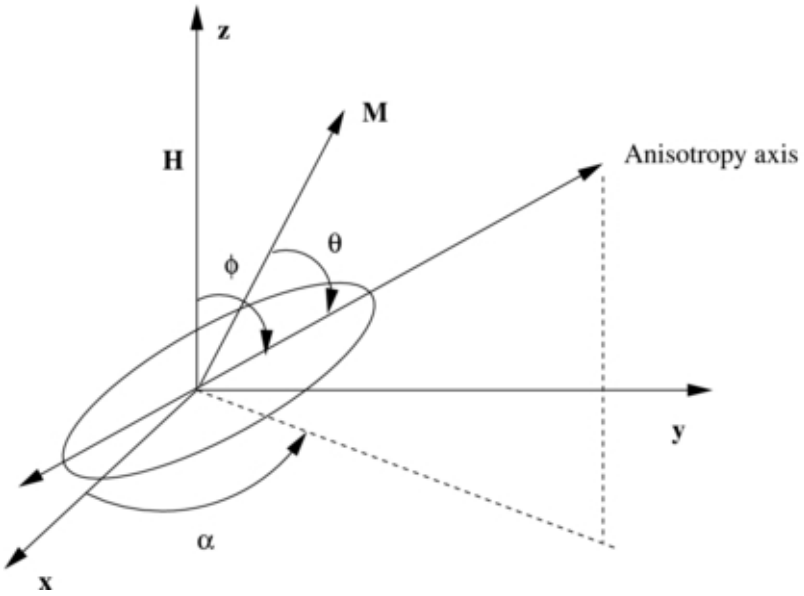

Figure 2.7: Single domain ellipsoid with magnetisation vector **M** in the presence of applied field **H**. Reproduced from [32].

(2.90), the nucleation field can then be written

$$H_n = -\frac{2K_1}{M_s} - \frac{Cq_2^2}{R^2 M_s} + \frac{M_s}{3}, \tag{2.92}$$

where q_2 is the smallest solution of (2.91). By equating equation (2.92) with the coherent rotation mode for a sphere (2.84) it is seen that magnetisation reversal in a sphere should start by coherent rotation if $R < R_c$, and by magnetisation curling if $R > R_c$, where

$$R_c = \frac{q_2}{M_s}\sqrt{\frac{3C}{4\pi}}. \tag{2.93}$$

The cross-over from curling to coherent rotation occurs because the exchange energy dominates below the threshold radius (2.93). This transition occurs abruptly unlike the gradual transformation between magnetisation ground states described in section 2.3.1, which is a continuous transformation of the core parameter λ.

2.4.2 Stoner-Wohlfarth model

For ferromagnetic spheres below the threshold radius (2.93) the exchange energy does not tolerate spatial variation in the magnetisation, which leads to a parallel orientation of the spins. As discussed in the previous section, in this situation the exchange energy is constant and does not enter into the energy minimization. As a result, it is sufficient to consider only the magnetocrystalline anisotropy, shape anisotropy and the interaction of the ferromagnetic body with the externally applied field. When the inter-particle interaction is negligible, the model which describes the hysteresis of the ferromagnetic material is known as the *Stoner-Wohlfarth* model. This model can describe the hysteresis of spherical particles when the magnetisation reverses by coherent rotation. When an external field **H** is applied at an angle θ to the easy axis of the uniaxial anisotropy, the magnetisation will rotate at an angle ϕ towards the direction of the applied field. If the magnetisation of a particle is at an angle $\phi - \theta$ to the easy axis z, and a magnetic field **H** is applied along z, then the total energy E is given by

$$E = K_1 V \sin^2(\phi - \theta) - \mu H \cos\phi, \tag{2.94}$$

where K_1 is the magnetocrystalline anisotropy constant, H is the applied field, μ is the magnetic moment and V is the volume. The magnetisation will favour the angle ϕ which minimizes the energy. Differentiating the reduced energy with respect to the angle ϕ leads to the minimum energy, namely

$$\frac{\partial \eta}{\partial \phi} = \frac{1}{2}\sin[2(\phi - \theta)] + h\sin\phi = 0, \tag{2.95}$$

where the reduced energy is defined as $\eta = \dfrac{E}{2K_1V} + const$ with $h = \dfrac{M_s H}{2K_1}$ and the magnetic moment has been replaced by $M_s V$. In Figure 2.8 the hysteresis loop for an ellipsoidal particle calculated with the Stoner-Wohlfarth model is shown for different

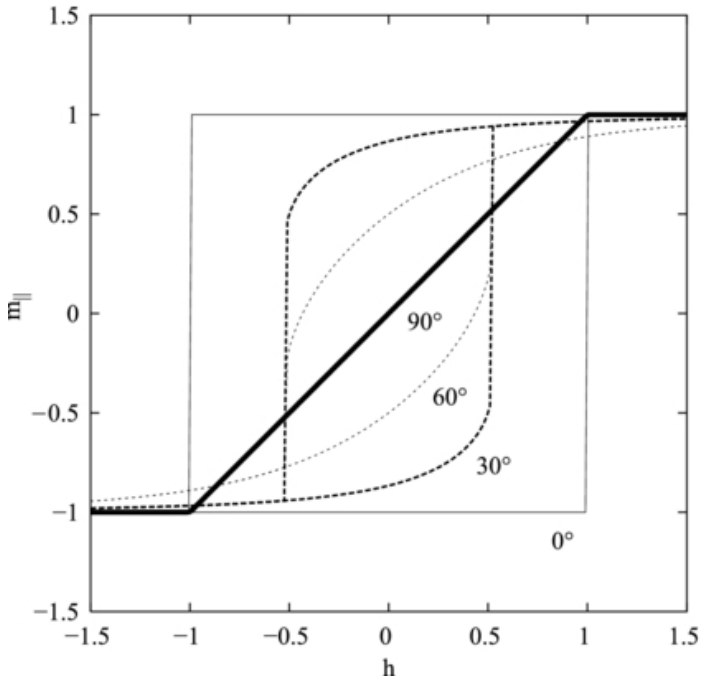

Figure 2.8: Longitudinal hysteresis loop for various angles ϕ of the field **H** with the easy axis. Reproduced from [32].

angles of the external DC field. Hysteretic behaviour is regularly exploited in control systems, when different values of the output are required as the input excitation is varied.

2.5 Ferromagnetic resonance

In the remaining sections of this chapter the dynamical properties of ferromagnetic materials will be introduced and discussed. For simplicity it will be assumed that a large DC field is present to saturate the sample, so that it possesses a single domain. Precession of the magnetisation about the equilibrium configuration can occur when an excitation field is applied perpendicular to the direction of saturation. This behaviour is known as *ferromagnetic resonance* (FMR) and is a characteristic feature of ferromagnetic materials. This precession is often uniform due to the strong exchange interaction between neighbouring magnetic moments. However, under suitable experimental conditions ferromagnetic materials may also undergo non-uniform

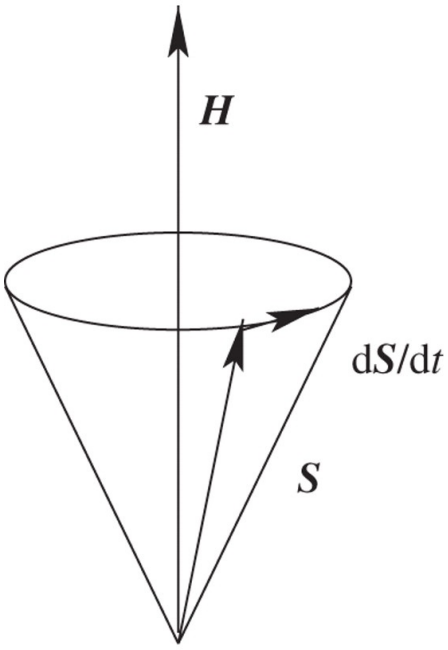

Figure 2.9: Time evolution of a single spin **S** about an effective field when damping is neglected. Reproduced from [33].

magnetisation precession. These non-uniform resonances can play an important role in the high-frequency properties of ferromagnetic materials, and are a central focus of this thesis.

2.5.1 Equation of motion

The Landau-Lifshitz-Gilbert equation, named after Lev Landau, Evgeny Lifshitz and T. L. Gilbert, describes the dynamic precession of a magnetic moment about an effective field. The equation was first proposed by L. D. Landau and E. M. Lifshitz in 1935 and later augmented by T. L. Gilbert in 1955 to account for large damping in ferromagnetic materials. In this section the phenomenological damping term is introduced and the general properties of the Landau-Lifshitz-Gilbert equation are discussed.

Macroscopic equations of motion for the magnetisation can be derived quantum mechanically, beginning with the time evolution of the spin operator. The time

evolution of the spin operator can be described by the Heisenberg equation [33]

$$\frac{d\hat{S}_j}{dt} = \frac{1}{i\hbar}[\hat{S}_j, \hat{H}] \tag{2.96}$$

where $\hat{S}$ is the spin operator and $\hat{H}$ is the Hamiltonian of the system. The Hamiltonian can be expanded in terms of spin operators,

$$[\hat{S}_j, \hat{H}] = -\sum_k \frac{\partial \hat{H}}{\partial \hat{S}_k}[\hat{S}_k, \hat{S}_j] + \mathcal{O}(\hbar^2) \tag{2.97}$$

where the components of the angular momentum are connected by the commutation relations

$$[S_x, S_y] = i\hbar S_z \tag{2.98}$$

$$[S_y, S_z] = i\hbar S_x \tag{2.99}$$

$$[S_z, S_x] = i\hbar S_y \tag{2.100}$$

Inserting equation (2.97) into (2.96) results in the expression for the time derivative of the spin operator

$$\frac{d\hat{S}}{dt} = -\hat{S} \times \frac{\partial \hat{H}}{\partial S} + \mathcal{O}(\hbar) \tag{2.101}$$

In the classical limit, the operators can be replaced with their expectation values and the spin can be replaced with the classical magnetic moment. This leads to the classical expression for the Landau-Lifshitz equation [33]

$$\frac{\partial \mathbf{M}}{\partial t} = -|\gamma_L|\mathbf{M} \times \mathbf{H}_{eff} \tag{2.102}$$

where $\gamma_L \approx 1.761 \times 10^{11}\mathrm{s}^{-1}\mathrm{T}^{-1}$ is the electron gyromagnetic ratio, $\mathbf{H}_{\mathrm{eff}}$ is the total effective field, the expectation value $\hat{H}$ has been replaced with the energy E and the second term $\mathcal{O}(\hbar)$ goes to zero as $\hbar \to 0$. This equation describes the dynamic precession of the magnetisation about an effective field in the absence of damping. In

this thesis, the effective field $\mathbf{H}_{eff}$ is given by

$$\mathbf{H}_{eff} = \mathbf{H}_{ex} + \mathbf{H}_{z} + \mathbf{H}_{ms} + \mathbf{H}_{ani} \tag{2.103}$$

where $H_{ex}, H_z, H_{ms}, H_{ani}$ are the exchange, Zeeman, magnetostatic and magnetocrystalline anisotropy energy contributions.

Equation 2.102 describes an undamped precessional motion about the effective field with no dissipation of the energy. This is not a realistic description of ferromagnetic materials, and so a phenomenological damping term was introduced by Landau and Lifshitz [29]

$$\frac{\partial \mathbf{M}}{\partial t} = -|\gamma_L|\mathbf{M} \times \mathbf{H}_{\text{eff}} - \lambda \mathbf{M} \times (\mathbf{M} \times \mathbf{H}_{\text{eff}}) \tag{2.104}$$

where λ is the phenomenological damping parameter. According to this equation, the speed of precession increases as the damping term increases, which is physically incorrect. As a result, Gilbert introduced another equation, known as the *Landau-Lifshitz-Gilbert* equation, which can account for large damping in ferromagnetic materials.

2.5.1.1 Damping

As discussed in the previous section, equation 2.102 describes a continuous precession of the magnetisation about the effective field at a constant angle and frequency. However, energy dissipation is present in realistic ferromagnetic materials, resulting in a decay of the precessing magnetisation towards the direction of the effective field. The minimum energy condition is reached when the time variation of the magnetisation vanishes. The principle damping term originates from spin-orbit coupling and can be derived from first-principles by non-relativistic expansion of the Dirac equation [34].

Gilbert introduced a phenomenological dissipation term which is proportional to

the time derivative of the magnetisation, given by

$$-\frac{\alpha}{\gamma_0 M_s}\frac{\partial \mathbf{M}}{\partial t} \tag{2.105}$$

where M_s is the saturation magnetisation and α is a dimensionless damping constant arising from the sources of dissipation in the system, e.g. Eddy currents. For ferromagnetic materials, the exact value of α varies with experimental conditions, but is typically of the order of $\approx 10^{-2}$. When the Gilbert damping term is added to the effective field the result is the *Landau-Lifshitz-Gilbert* equation,

$$\frac{\partial \mathbf{M}}{\partial t} = -\gamma_0(\mathbf{M} \times \mathbf{H}_{\text{eff}}) - \frac{\alpha}{M_s}\left(\mathbf{M} \times \frac{\partial \mathbf{M}}{\partial t}\right) \tag{2.106}$$

which describes the time evolution of the dynamic magnetisation including both the precessional and damping term. This equation can be transformed to the Landau-Lifshitz form by applying the cross product of $\mathbf{M}$ to obtain

$$\mathbf{M} \times \frac{\partial \mathbf{M}}{\partial t} = -\gamma_0 \mathbf{M} \times (\mathbf{M} \times \mathbf{H}_{\text{eff}}) - \alpha M_s \frac{\partial \mathbf{M}}{\partial t} \tag{2.107}$$

Inserting equation (2.107) into (2.106) leads to

$$\frac{\partial \mathbf{M}}{\partial t} = -\gamma_L \mathbf{M} \times \mathbf{H}_{eff} - \frac{\alpha'}{M_s}\mathbf{M} \times (\mathbf{M} \times \mathbf{H}_{eff}) \tag{2.108}$$

where the gyromagnetic ratio is $\gamma_L = \gamma_0/(1+\alpha^2)$ and damping constant $\alpha' = \gamma_0\alpha/(1+\alpha^2)$. The Landau-Lifshitz and Landau-Lifshitz-Gilbert equations are only equivalent in the limit of small damping, when the value of the damping constant α is low and the denominator $(1+\alpha^2)$ becomes ≈ 1.

2.5.1.2 Conservation of magnetisation

It follows from the previous section that the magnitude of the magnetisation vector must be conserved as it evolves in time. When the effective field is not explicitly time-dependent, this can be seen by directly evaluating the time derivative of the squared magnetisation

$$\frac{\partial}{dt}|\mathbf{M}|^2 = \frac{\partial}{dt}(\mathbf{M}\cdot\mathbf{M}) = 2\mathbf{M}\cdot\frac{\partial\mathbf{M}}{\partial t} \tag{2.109}$$

and substituting equation (2.108) into (2.109) to give

$$\frac{\partial}{\partial t}|\mathbf{M}^2| = 2\mathbf{M}\cdot\left(-\gamma_L\mathbf{M}\times\mathbf{H}_{\text{eff}} - \frac{\alpha'}{M_s}\mathbf{M}\times(\mathbf{M}\times\mathbf{H}_{\text{eff}})\right) = 0 \tag{2.110}$$

Therefore, for a ferromagnetic body made of the same material the absolute value of the magnetisation is constant everywhere. Conservation of the magnitude of the magnetisation vector is a necessary condition for any numerical computation to produce physically meaningful results. However, this condition is often not satisfied due to the accumulation of numerical error when solving the non-linear LLG equation. As a result, micromagnetic solvers must actively preserve the vector through one of several numerical schemes, such as renormalisation (magpar), self-correcting LLG (nmag) and the 4th order Runge-Kutta method (OOMMF).

2.5.1.3 Energy decay

A second important criterion is that the total energy of the system decays in time. To verify that this is the case, it is convenient to re-write the normalised Landau-Lifshitz-Gilbert equation in the following form

$$\frac{\partial\mathbf{M}}{\partial t} = -\mathbf{M}\times\left(\mathbf{H}_{\text{eff}} - \alpha\frac{\partial\mathbf{M}}{\partial t}\right) \tag{2.111}$$

Multiplying both sides of this equation by $\mathbf{H}_{eff} - \alpha\dfrac{\partial \mathbf{M}}{\partial t}$ leads to the result

$$\frac{\partial \mathbf{M}}{\partial t} \cdot \left(\mathbf{H}_{eff} - \alpha \frac{\partial \mathbf{M}}{\partial t} \right) = 0 \tag{2.112}$$

The expression which relates the time derivative of the free energy E to the effective field is given by [29]

$$\frac{dE}{dt} = \int_V \left(\frac{\delta E}{\delta \mathbf{M}} \cdot \frac{\partial \mathbf{M}}{\partial t} + \frac{\delta E}{\delta \mathbf{H}_{eff}} \cdot \frac{\partial \mathbf{H}_{eff}}{\partial t} \right) dV \tag{2.113}$$

which can also be written

$$\frac{dE}{dt} = \int_V \left(- \mathbf{H}_{eff} \cdot \frac{\partial \mathbf{M}}{\partial t} - \mathbf{M} \cdot \frac{\partial \mathbf{H}_{eff}}{\partial t} \right) dV \tag{2.114}$$

By integrating equation (2.112) over the volume and using the above expression for the free energy, we obtain

$$\frac{dE}{dt} = -\alpha \int_V \left| \frac{\partial \mathbf{M}}{\partial t} \right|^2 dV \tag{2.115}$$

This equation implies that $dE/dt \leq 0$. The rate of energy loss is proportional to the damping constant and the energy is conserved when the damping constant α is set to 0. For the purpose of steady-state numerical calculations, it is a common practise to increase the damping constant to speed up converge towards the equilibrium configuration.

2.5.2 Uniform resonance

The atomic moments of a ferromagnetic material will tend to precess coherently about the equilibrium configuration due to the presence of strong exchange forces. The frequency of the uniform mode of magnetisation precession can be calculated from Kittel's formula, accounting for the various contributions to the effective field. For an ideally saturated ellipsoid the internal magnetic fields are uniform and the

calculation of the ferromagnetic resonance is straightforward. Assuming the presence of a static magnetic field that is sufficiently large to remove the domain structure, then the effective field of a uniformly magnetized ellipsoid can be written as

$$H_{eff} = H_0 - NM + H_k \tag{2.116}$$

where H_0 is the external static field applied along an axis defined here as the z-axis, NM is the demagnetising field and H_k is the anisotropy field. The expression for the resonance frequency is the same for a uniaxial or cubic magnetocrystalline anisotropy. When M and H are parallel, the magnetisation M can be written as [35]

$$\begin{aligned}\frac{dM_1(t)}{dt} = -\gamma[M_s \times H_1(t) + M_1(t) \times H + M_s M_{1y}(t)(N_y - N_z)i \\ -M_s M_{1x}(t)(N_x - N_z)j + M_1 \times H_k]\end{aligned}$$

where we have the expression $N \cdot M_1(t) = N_x M_{1x}(t)i + N_y M_{1y}(t)j + N_z M_{1z}(t)k$, when second-order quantities and damping are neglected. When the easy and hard axis coincide with the reference axis, the expression for the components can then be written [35]

$$\frac{i\omega M_{1x}(t)}{\gamma} = -M_{1y}[H + M_s(N_y + N_{Ky} - N_z - N_{Kz})] + M_s H_{1y} \tag{2.117}$$

$$\frac{i\omega M_{1y}(t)}{\gamma} = -M_{1x}[H + M_s(N_x + N_{Kx} - N_z - N_{Kz})] + M_s H_{1x} \tag{2.118}$$

and

$$M_{1z} = 0 \tag{2.119}$$

A non-trivial solution exists provided that the determinant of the coefficients vanishes

$$\begin{vmatrix} \dfrac{i\omega_r}{\gamma} & -H_r + M_s(N_y + N_{Ky} - N_z - N_{Kz}) \\ H_r + M_s(N_x + N_{Kx} - N_z - N_{Kz}) & \dfrac{i\omega_r}{\gamma} \end{vmatrix} = 0.$$

Solving this leads to Kittel's equation for the ferromagnetic resonance frequency,

$$\omega_r = -\gamma\sqrt{\big(H_r + (N_y + N_{k_y} - N_z - N_{k_z})M_s\big) \times \big(H_r + (N_x + N_{k_x} - N_z - N_{k_z})M_s\big)}$$
$$= -\gamma H_r$$

where ω_r is the resonance frequency and H_r is the corresponding resonance field. For a ferromagnetic sphere, the demagnetising and anisotropy fields are given by $N_x = N_y = N_z = 1/3$ and the anisotropy field is $N_{Kx} = N_{Ky} = 0$, $N_{Kz} = \dfrac{2K_1}{M_s}$. The frequency for the ferromagnetic resonance of a ferromagnetic sphere is then given by

$$\omega = -\gamma\big(H_r + \frac{2K_1}{M_s}\big) \tag{2.120}$$

The components of the magnetisation can be calculated by solving the equations (2.117)-(2.118) for M_x and M_y, leading to

$$M_{1x} = \frac{\gamma^2 M_s(H + (N_y + N_{Ky} - N_z - N_{Kz})M_s)}{\omega_r^2 - \omega^2}H_{1x} - \frac{i\omega\gamma M_s}{\omega_r^2 - \omega^2}H_{1y}, \tag{2.121}$$

$$M_{1y} = \frac{i\omega\gamma M_s}{\omega_r^2 - \omega^2}H_{1x} + \frac{\gamma^2 M_s(H + (N_x + N_{Kx} - N_z - N_{Kz})M_s)}{\omega_r^2 - \omega^2} \tag{2.122}$$

The magnetic susceptibility $M_1 = \chi_e H_1$ can then be written,

$$M_1 = \chi_e H_1 \tag{2.123}$$

and

$$\chi_e = \begin{pmatrix} \chi_{11} & \chi_{12} & 0 \\ \chi_{21} & \chi_{22} & 0 \\ 0 & 0 & 0 \end{pmatrix} \tag{2.124}$$

for which the elements of the tensor susceptibility are given by

$$\chi_{11} = \frac{\gamma^2 M_s(H + (N_y + N_{Ky} - N_z - N_{Kz})M_s)}{\omega_r^2 - \omega^2}, \tag{2.125}$$

$$\chi_{22} = \frac{\gamma^2 M_s(H + (N_x + N_{Kx} - N_z - N_{Kz})M_s)}{\omega_r^2 - \omega^2}, \tag{2.126}$$

$$\chi_{12} = -\chi_{21} = \frac{i\omega\gamma M_s}{\omega_r^2 - \omega^2}, \tag{2.127}$$

The tensor χ_r is known as the extrinsic susceptibility, as it relates the precessing magnetisation to the externally applied ac field. When the high-frequency susceptibility is expressed in terms of the alternating field inside the sample, it is known as the *intrinsic* susceptibility χ_i, given by

$$\chi_i = \chi_e(1 + N \cdot \chi_i) \tag{2.128}$$

When damping is included the elements of the susceptibility tensor are complex, giving rise to power loss. In this case, the tensor susceptibility for a spherical sample can be written

$$\chi_{11} = \chi_{22} = \frac{\gamma M_s(\gamma H + i\omega\alpha)}{(\omega_r + i\omega\alpha)^2 - \omega^2} \tag{2.129}$$

$$\chi_{21} = -\chi_{21} = \frac{i\omega\gamma M_s}{(\omega_r + i\omega\alpha)^2 - \omega^2} \tag{2.130}$$

when assuming a uniform excitation field and negligible magnetocrystalline anisotropy.

2.5.3 Magnetostatic resonance

In the previous section it was assumed that the atomic dipoles precess in phase. However, it is possible to excite other precessional modes by applying a non-uniform excitation field, or by using a sample with a non-ellipsoidal shape. Such non-uniform resonance modes were succinctly described by Walker for a spherical sample, and first observed experimentally in 1956. In Walker's derivation, the spherical samples

are assumed to be sufficiently large such that the exchange contribution is negligible, and the wavelength is comparable to the dimensions of the sample. Moreover, since there is little propagation of the wave it is sufficient to use a magnetostatic form of Maxwell's equations. Hence, these non-uniform modes are known as the *magnetostatic modes*. A characteristic feature of the magnetostatic modes is that that they are size-independent, so long as the increase in exchange energy with decreasing particle size is small compared to the classical dipole-dipole interaction.

Consider an ellipsoid of revolution with negligible magnetocrystalline anisotropy when an external DC field is applied along the polar axis. It follows from the equations (2.5.2) and (2.5.2) that the dynamic magnetisation components are given by

$$M_{1x} = \chi_{11} H_{1x} + \chi_{12} H_{1y} \tag{2.131}$$

$$M_{1y} = \chi_{21} H_{1x} + \chi_{22} H_{1y}, \tag{2.132}$$

where $\chi_{12} = -\chi_{21}$ and $\chi_{11} = -\chi_{22}$, given that $N_x = D_y$. It is sufficient to use the magnetostatic form of Maxwell's equations when the propagation is negligible, which gives

$$\nabla \times H_1 = 0 \tag{2.133}$$

and

$$\nabla \cdot B_1 = \nabla \cdot (H_1 + 4\pi M_1) = 0. \tag{2.134}$$

When defining a scalar potential φ such that $H_1 = -\nabla\varphi$ equations (2.131) - (2.132) become

$$-M_{1x} = \chi_{11} \frac{\partial \varphi}{\partial x} + \chi_{12} \frac{\partial \varphi}{\partial y} \tag{2.135}$$

and

$$-M_{1y} = \chi_{21} \frac{\partial \varphi}{\partial x} + \chi_{22} \frac{\partial \varphi}{\partial y} \tag{2.136}$$

From Maxwell's equations we have

$$\nabla^2\varphi - 4\pi\nabla \cdot M_1 = 0. \tag{2.137}$$

By eliminating M_1 it can be shown that φ satisfies the differential equation

$$(1 + 4\pi\chi_{11})\left(\frac{\partial^2\varphi}{\partial x^2} + \frac{\partial^2\varphi}{\partial y^2}\right) + \frac{\partial^2\varphi}{\partial z^2} = 0. \tag{2.138}$$

inside the ellipsoid and the Laplace equation

$$\nabla^2\varphi = 0 \tag{2.139}$$

outside the ellipsoid. The result is an eigenvalue problem where the solutions for φ depend on associated Legendre polynomials P_n^m and $e^{im\phi}$, where ϕ is the azimuthal angle. Here n and m indicate the periodicity in the dynamic magnetisation with respect to the angle ϕ. The coordinate r specifies the root of a characteristic equation that results in the resonance frequency. The magnetostatic modes can be situated either above or below the uniform precession line, and are useful for determining the intrinsic magnetic parameters of a sample, such as the g-value, the magnetocrystalline anisotropy constant and the saturation magnetisation.

2.5.4 Exchange resonance

The magnetic properties of fine particles can differ greatly from bulk ferromagnets or ferrites. The source of this difference is the fact that in fine particles exchange and surface effects are not negligible, in comparison with their bulk counterparts. The resonant properties of ferromagnetic nanoparticles was studied by Aharoni accounting for exchange and surface contributions [36, 37]. Assuming the presence of a large DC field applied along the z direction and small perturbation of M_x and M_y, the dynamic

equation can be solved as a *linearized* set of equations

$$\left(\frac{C}{M_s}\nabla^2 - H_z\right)M_x - \left(\frac{i\omega}{\gamma_0}\right)M_y = \frac{\partial V_{in}}{\partial x} \tag{2.140}$$

and

$$\left(\frac{C}{M_s}\nabla^2 - H_z\right)M_y + \left(\frac{i\omega}{\gamma_0}\right)M_x = \frac{\partial V_{in}}{\partial y} \tag{2.141}$$

where M is a unit vector parallel to the magnetisation, $C = 2A$ is the exchange constant, M_s is the saturation magnetisation, γ_0 is the gyromagnetic ratio, H_z is the effective field and V_{in} is the potential due to the M_x and M_y components of the magnetisation. Following Aharoni's solution, the components of the magnetisation are expressed in the cylindrical co-ordinates ρ, ϕ, z and the spatial dependence of the derivatives is expressed in spherical coordinates r, θ, ϕ, namely

$$\left(\frac{\partial^2}{\partial r^2} + \frac{2}{r}\frac{\partial}{\partial r} + \frac{1}{r^2}\frac{\partial^2}{\partial\theta^2} + \frac{\cos\theta}{r^2\sin\theta}\frac{\partial}{\partial\theta} - \frac{1}{r^2\sin^2\theta} - \frac{M_s H_z}{C}\right)m_\phi + \frac{iM_s\omega}{\gamma_0 C}m_\rho = 0$$

and

$$\left(\frac{\partial^2}{\partial r^2} + \frac{2}{r}\frac{\partial}{\partial r} + \frac{1}{r^2}\frac{\partial^2}{\partial\theta^2} + \frac{\cos\theta}{r^2\sin\theta}\frac{\partial}{\partial\theta} - \frac{1}{r^2\sin^2\theta} - \frac{M_s H_z}{C}\right)m_\phi - \frac{iM_s\omega}{\gamma_0 C}m_\rho = \frac{M_s}{C}\left(\sin\theta\frac{\partial}{\partial r} + \frac{\cos\theta}{r}\frac{\partial}{\partial\theta}\right)V_{in}$$

The equations for the potential inside and outside the sphere are given by

$$\left(\frac{\partial^2}{\partial r^2} + \frac{2}{r}\frac{\partial}{\partial r} + \frac{1}{r^2}\frac{\partial^2}{\partial\theta^2} + \frac{\cos\theta}{r^2\sin\theta}\frac{\partial}{\partial\theta}\right)V_{in} = 4\pi M_s\left(\frac{1}{r\sin\theta} + \frac{\cos\theta}{r}\frac{\partial}{\partial\theta} + \sin\theta\frac{\partial}{\partial r}\right)m_\rho \quad \text{if} \quad r \le R$$

$$\left(\frac{\partial^2}{\partial r^2} + \frac{2}{r}\frac{\partial}{\partial r} + \frac{1}{r^2}\frac{\partial^2}{\partial\theta^2} + \frac{\cos\theta}{r^2\sin\theta}\frac{\partial}{\partial\theta}\right)V_{out} \quad \text{if} \quad r \ge R$$

where R is the radius of the sphere. The boundary conditions on the surface of the sphere are given by

$$\frac{\partial m_\rho}{\partial r} = \frac{\partial m_\phi}{\partial r} = 0 \tag{2.142}$$

$$V_{in} = V_{out} \tag{2.143}$$

$$\frac{\partial V_{in}}{\partial r} - \frac{\partial V_{out}}{\partial r} = 4\pi M_s m_\rho \sin\theta \tag{2.144}$$

For sufficiently small ferromagnetic nanoparticles, the exchange energy is much larger than the magnetostatic energy. Therefore, in the exchange approximation the magnetostatic energy term can be neglected altogether by setting $V_{in} = V_{out} = 0$. In this exchange-dominated regime the expression for the resonance frequency is given by the equation

$$\pm\frac{\omega}{\gamma_0} = \frac{C\mu_{kn}^2}{R_2^2 M_s} + H_0 + \frac{2K_1}{M_s} \tag{2.145}$$

subject to the boundary condition

$$\left(\frac{dj_n(\mu_{kn} r/R)}{dr}\right)_{r=R} = 0 \tag{2.146}$$

where ω is the frequency, R_2 is the outer radius, H_0 is the saturation field, M_s is the saturation magnetisation, γ_0 is the gyromagnetic ratio, μ are the eigenvalues of equations (2.149) and (2.150), K_1 is the magnetocrystalline anisotropy constant and j_n is the spherical Bessel function of the first kind. The exchange resonance approximation closely resembles the curling nucleation mode because the demagnetising field vanishes when an ellipsoid nucleates by a vortex configuration. A characteristic feature of the exchange modes is that they are *size-dependent* as can be seen by the $1/R_2^2$ dependence in equation (2.145). In the case of magnetite, the exchange energy dominates over the magnetostatic energy for a radius R_2 below ≈ 20 nm [38]. However, calculations presented by Arias et al. [39] showed that the frequency remains proportional to $1/R_2^2$ to rather good approximation for larger particle sizes.

2.6 Summary

In summary, the background concepts of magnetism which are relevant for this thesis have been introduced. The subject of the chapter converged towards the non-uniform magnetisation ground states and dynamics of ferromagnetic particles in the micrometer, sub-micrometer and nanometer size ranges, which are the central focus of this thesis. In the next chapter the numerical methods used to investigate the precessional magnetisation dynamics of these materials will be discussed.

Chapter 3

Methodology

This section introduces the methodology of numerical micromagnetics which is the basis of the simulations carried out in this thesis. Micromagnetics is a semi-classical continuum approximation of ferromagnetism which considers length-scales that are small enough to accurately resolve magnetic domain walls, but large enough that the atomic structure of the material can be neglected. Micromagnetics can be used to calculate the equilibrium state of magnetic materials by minimizing Brown's equations subject to the appropriate boundary conditions and energy terms. Alternatively, dynamical behaviour can be calculated by solving the time-dependent equation of magnetisation motion. In this chapter, the numerical implementation of the Landau-Lifshitz-Gilbert equation of magnetisation motion and the associated effective field terms will be discussed. Finally, a generalised electromagnetic-micromagnetic approach which incorporates the complete solution of Maxwell's equation is presented.

3.1 Numerical micromagnetics

For the purpose of numerical implementation, the discretized form of the Landau-Lifshitz-Gilbert equation can be written

$$\frac{\partial \mathbf{M}_{ijk}}{\partial t} = \gamma_{ijk}(\mathbf{M}_{ijk} \times \mathbf{H}^{eff}_{ijk}) + \frac{\alpha_{ijk}}{M^{s}_{ijk}}\big(\mathbf{M}_{ijk} \times \frac{\partial \mathbf{M}_{ijk}}{\partial t}\big) \tag{3.1}$$

where ijk is the finite difference notation representing the location of each cell in a regular mesh grid. To integrate the LLG equation, the first order derivative in (3.1) is replaced with its finite difference equivalent and the time domain becomes discretised. In solvers such as OOMMF and Mumax3, the LLG equation can be integrated using the classical Runge-Kutta method where the value of the magnetisation $\mathbf{M}_{ijk}$ is given by

$$\mathbf{M}_{ijk}(t_{n+1}) = \mathbf{M}_{ijk}(t_n) + \frac{1}{6}(k_1 + 2k_2 + 2k_3 + k_4)$$

$$k_1 = f(t_n, \mathbf{M}_{ijk}(t_n))\nabla t$$

$$k_2 = f(t_n + \frac{1}{2}\nabla t, \mathbf{M}_{ijk}(t_n + \frac{1}{2}k_1))\nabla t$$

$$k_3 = f(t_n + \frac{1}{2}\nabla t, \mathbf{M}_{ijk}(t_n) + \frac{1}{2}k_2)\nabla t$$

$$k_4 = f(t_n + \nabla t, \mathbf{M}_{ijk}(t_n) + k_3)\nabla t$$

At each time-step ∇t the numerical error is evaluated. The solver is allowed to proceed to the next time-step if the computed error in each cell is smaller than a predefined threshold value. If the error exceeds this value, then the calculation is repeated using a smaller time-step. In this way the magnitude of the magnetisation

vector is conserved and the absolute value of the numerical error is kept small. For the magnetostatic calculations carried out in this thesis, the discretized equation of magnetisation motion (3.1) is solved using the following torque fields and boundary conditions:

Applied Field

An internal, user-defined field inside the magnetic medium and can be static or transient, uniform or non-uniform. It is used in this thesis to specify the static and dynamic pulse fields in the magnetic material.

Demagnetising Field

In Chapters $5-7$ of this thesis the conventional demagnetising field described in section 2.2.2.1 is used to calculate the long-range magnetic fields inside and outside the ferromagnetic material. In Chapter 8 the long-range fields due to currents and magnetic sources are generated from the full solution of Maxwell's equations including demagnetising fields, Eddy current fields and scattering fields.

Exchange Field

A numerical implementation of the exchange interaction must use a discretized form of either (2.55) or (2.56) which requires evaluating both the integral and the enclosed derivatives, with special treatment at the boundary of the magnetic material. The Laplace operator in the expression of the exchange energy can be replaced with its finite difference equivalent,

$$E_{ex} = -V_h \sum_{jk} w_j^y w_k^z \sum_{ii'} A_{ijk} w_i^x d_{ii'} \mathbf{M}_{ijk} \cdot \mathbf{M}_{i'jk} \tag{3.2}$$

where we have considered one term in (2.56), $d_{ii'}$ is a discretized form of the operator $\partial^2/\partial x^2$ and w are the weights. The second derivative in equation (2.56) is commonly approximated by the expression

$$f''(x_i) = \frac{1}{h^2}(f_{i-1} - 2f_i + f_{i+1}) + \mathcal{O}(h^2) \tag{3.3}$$

where the index i corresponds to the x-axis. The cell at location i has two nearest-neighbours at the locations $i-1$ and $i+1$. The sum can be expanded into three-dimensions by including the terms $\partial^2/\partial y^2$ and $\partial^2/\partial z^2$ which leads to 6 nearest neighbours for any particular cell, provided that it is not positioned at a boundary. Hence, this numerical implementation is known as the *six nearest neighbour* method.

Anisotropy Field

For numerical computations involving Permalloy the material is assumed to have a negligible uniaxial magnetocrystalline anisotropy in comparison to the shape anisotropy and applied fields. In the case where the uniaxial magnetocrystalline anisotropy is considered, the torque field is given by:

$$H_k = \frac{-2K_u}{\mu_0 M_s^2}(M \cdot u)\mathbf{u} \tag{3.4}$$

where K_u is the anisotropy constant, and u is a unit vector parallel to the anisotropy axis. For iron which has a cubic structure the following cubic anisotropy energy density E_{cubic} is used

$$E_{cubic} = K_1(\alpha^2\beta^2 + \beta^2\gamma^2 + \gamma^2\alpha^2) + K_2\alpha^2\beta^2\gamma^2 \tag{3.5}$$

where the constants K_1 and K_2 are the cubic anisotropy constants described in section 2.2.2.

Boundary Conditions

The most commonly utilized boundary condition in micromagnetic solvers is written

$$\frac{\partial \mathbf{M}}{\partial n} = 0 \tag{3.6}$$

where n is normal to the surface. Inclusion of surface anisotropy leads to a modified boundary condition

$$\frac{\partial \mathbf{M}}{\partial n} + \frac{2K_s}{C} = 0 \tag{3.7}$$

where K_s is the surface anisotropy constant and C is the exchange constant. There are several possible contributions to the surface anisotropy energy which can become very important when the surface-to-volume ratio is large, as is the case with spherical nanoparticles. In this thesis, numerical computations are performed with the Neumann boundary condition $\partial \mathbf{M}/\partial n = 0$, i.e. neglecting surface anisotropy. The problem of surface anisotropy is treated analytically in Chapter 4.

3.2 Maxwell-Landau-Lifshitz-Gilbert formulation

Conventional micromagnetic solvers employ a magnetostatic form of Maxwell's equations. As a result, they are not suitable for studying electromagnetic interaction with lossy magnetic material. In this section, the Landau-Lifshitz-Gilbert (LLG) equation is coupled to the complete solution of Maxwell's equations in order to study the interaction between electromagnetic waves from current and charge sources with non-linear magnetic material. This is of particular importance in the simulation of devices containing conductive magnetic and dielectric materials operating at microwave frequencies.

3.2.1 Coupled equations

The system of equations for the non-linear Landau-Lifshitz-Gilbert equation and Maxwell's equations can be written [40, 41]

$$\begin{cases} \epsilon_0 \dfrac{\partial \mathbf{E}}{\partial t} - \nabla \times \mathbf{H} + \sigma \mathbf{E} = 0 \\ \mu_0 \dfrac{\partial \mathbf{H}}{\partial t} + \nabla \times \mathbf{E} = -\mu_0 M_s \dfrac{\partial \mathbf{M}}{\partial t} \\ \dfrac{\partial \mathbf{M}}{\partial t} = |\gamma| \mathbf{H}_T(m) \times \mathbf{M} + \alpha \mathbf{M} \times \dfrac{\partial \mathbf{M}}{\partial t}, \end{cases} \tag{3.8}$$

where $\mathbf{H}$ is the magnetic field, $\mathbf{E}$ is the electric field, σ is the electrical conductivity and ϵ_0 and μ_0 are the vacuum electric permittivity and magnetic permeability, respectively. The magnetic coupling is given by the equation

$$\begin{cases} \mathbf{B} = \mu_0(\mathbf{H} + \mathbf{M}) \quad \text{inside} \\ \\ \mathbf{B} = \mu \mathbf{H} \quad \text{outside} \end{cases} \tag{3.9}$$

The proof of magnetisation conservation in the LLG equation is unchanged from the previous section. The conditions for which the magnetisation $\mathbf{M}$ and the field $\mathbf{H}$ of the coupled system (3.8) are divergence free has been the focus of considerable mathematical analysis. The existence of weak solutions for the coupled Maxwell-Landau-Lifshitz-Gilbert (MLLG) formulation has been rigorously proven under the following constraints [41]

$$\nabla \cdot (\mathbf{H}_0 + \mathbf{M}_0) = 0 \implies \nabla \cdot (\mathbf{H} + \mathbf{M}) = 0, \forall t \geq 0, \tag{3.10}$$

and

$$\nabla \cdot \mathbf{E}_0 = 0 \implies \nabla \cdot \mathbf{E} = 0, \forall t \geq 0, \tag{3.11}$$

where $\mathbf{E}_0, \mathbf{H}_0$ and $\mathbf{M}_0$ are the initial conditions. Thus, any solution of the coupled equations is divergence-free for all time, provided that the initial input data is divergence free.

3.2.2 Electromagnetic energy

It can be shown that the electromagnetic energy of this coupled system of equations decays in time [42]. Starting from Maxwell's equations and multiplying across by $\mathbf{E}$ and $\mathbf{H}$ leads to the expression

$$\mathbf{E} \cdot (\nabla \times \mathbf{H}) - \mathbf{H} \cdot (\nabla \times \mathbf{E}) = \epsilon_0 \mathbf{E} \cdot \frac{\partial \mathbf{E}}{\partial t} + \mu_0 \mathbf{H} \cdot \frac{\partial \mathbf{H}}{\partial t} + \mu_0 \mathbf{H} \cdot \frac{\partial \mathbf{M}}{\partial t} \tag{3.12}$$

By integrating over the volume and applying Green's formula, we have

$$\int_V \nabla \cdot (\mathbf{E} \times \mathbf{H}) dx = \int_V \left(\epsilon_0 \mathbf{E} \cdot \frac{\partial \mathbf{E}}{\partial t} + \mu_0 \mathbf{H} \cdot \frac{\partial \mathbf{H}}{\partial t} \right) dx + \mu_0 \int_V \mathbf{H} \cdot \frac{\partial \mathbf{M}}{\partial t} dx = 0 \tag{3.13}$$

By adding $\mathbf{H}_{eff}$ to $\mathbf{H}$ equation (3.13) can be re-written as

$$\frac{d}{dt} \left[\frac{\epsilon_0}{2} ||\mathbf{E}||^2 + \frac{\mu_0}{2} ||\mathbf{H}||^2 \right] - \mu_0 \int \mathbf{H}_{\text{eff}}(\mathbf{M}) \cdot \frac{\partial \mathbf{M}}{\partial t} d\mathbf{x} = -\mu_0 \int \mathbf{H}_T(\mathbf{H},\, \mathbf{M}) \cdot \frac{\partial \mathbf{M}}{\partial t} d\mathbf{x} \tag{3.14}$$

where $\mathbf{H}_T(\mathbf{H}, \mathbf{M})$ has been introduced for convenience. In (3.14) the term involving the effective field can be expressed as

$$\mu_0 \int_V \mathbf{H}_{eff}(\mathbf{M}) \cdot \frac{\partial \mathbf{M}}{\partial t} d\mathbf{x} = -\frac{d}{dt} \left(\mathcal{E}_a(\mathbf{M}) \right) \tag{3.15}$$

where $\mathcal{E}_a$ is the energy due to the effective field. Taking the vector product of the LLG equation with respect to $\partial \mathbf{M}/\partial t$,

$$\frac{\partial \mathbf{M}}{\partial t} \times \frac{\partial \mathbf{M}}{\partial t} = 0 = |\gamma| \left(\mathbf{H}_T(\mathbf{H},\mathbf{M}) \cdot \frac{\partial \mathbf{M}}{\partial t} \right) \mathbf{M} - \frac{\alpha}{|\mathbf{M}|} \left| \frac{\partial \mathbf{M}}{\partial t} \right|^2 \mathbf{M}. \tag{3.16}$$

Rearranging equation (3.16) leads to the expression

$$\mathbf{H}_T(\mathbf{H},\mathbf{M}) \cdot \frac{\partial \mathbf{M}}{\partial t} = -\frac{\alpha}{|\gamma|}\frac{1}{|\mathbf{M}|}\left|\frac{\partial \mathbf{M}}{\partial t}\right|^2 \tag{3.17}$$

Combining (3.16) and (3.17) with (3.14) leads to the time decay of the electromagnetic energy

$$\frac{d}{dt}\left[\frac{\epsilon_0}{2}||\mathbf{E}||^2 + \frac{\mu_0}{2}||\mathbf{H}||^2 + \mathcal{E}_a(\mathbf{M})\right] = -\mu_0\frac{\alpha}{|\gamma|}\int \frac{1}{|\mathbf{M}|}\left|\frac{\partial \mathbf{M}}{\partial t}\right|^2 dx \tag{3.18}$$

Equation (3.18) elucidates why the ferromagnetic material is absorbing, because the electromagnetic energy decay is determined by the damping constant α of the magnetic material. Moreover, as a consequence of this energy decay, the time derivatives of $(\mathbf{E}, \mathbf{H}, \mathbf{M})$ must vanish at equilibrium,

$$\frac{\partial \mathbf{E}}{\partial t} = \frac{\partial \mathbf{H}}{\partial t} = \frac{\partial \mathbf{M}}{\partial t} = 0 \tag{3.19}$$

Thus, the coupled system (3.8) reduces to the magnetostatic field described previously

$$\begin{cases} \nabla \times \mathbf{H} + \sigma \mathbf{E} = 0, \\ \nabla \times \mathbf{E} = 0, \\ \mathbf{H}_{T(M)} \times \mathbf{M} = 0. \end{cases} \tag{3.20}$$

This formulation allows the inclusion of anisotropy and exchange effects, while the electromagnetic fields due to magnetic and/or electric charges and currents are evaluated through the solution of Maxwell's equations. Hence, this approach allows for the steady-state and dynamic simulation of complete magnetic based devices with dielectric and conductive layers. In the above formulation, it is important to note that the fields at equilibrium are independent of both the damping constant α and conductivity σ. As a result, they can be increased in order to accelerate convergence of the magnetisation towards the steady-state solution.

3.3 Numerical implementation

3.3.1 Finite-difference time-domain (FDTD) method

3.3.2 Maxwell's equations

This thesis focuses on the transverse-magnetic mode with respect to the z dimension (TMz) for simplicity. Nevertheless, the work presented here is applicable to the transverse-electric (TEz) and full three-dimensional Maxwell's equations. In the TMz mode, Maxwell's curl equations reduce to:

$$\frac{\partial B_x}{\partial t} = -\frac{\partial E_z}{\partial y} \tag{3.21}$$

$$\frac{\partial B_y}{\partial t} = -\frac{\partial E_z}{\partial x} \tag{3.22}$$

$$\epsilon \frac{\partial E_z}{\partial t} = \frac{\partial H_y}{\partial x} - \frac{\partial H_x}{\partial y} - \sigma E_z \tag{3.23}$$

The detailed implementation of Maxwell's equations and the LLG equation within the FDTD method can be found elsewhere [43], and only fundamental and relevant parts will be repeated and expanded here for completeness. Figure 3.1 shows the basic unit cell (or the Yee cell) in the FDTD method in the TMz mode. In this arrangement, each **E** field component in the centre of the cell is evaluated from the curl of the four surrounding magnetic field components, while each **H** field component is evaluated using the curl of the two neighbouring **E** components. The electric and magnetic fields are not co-located in space and displaced from each other by half a cell length. This field arrangement naturally enforces the electromagnetic boundary conditions of Maxwell's equations at the interfaces of different materials [44]. The convention used here to represent the discretised field component f in two dimensions is $f|^n_{i,j} = f(i\delta x, j\delta y, n\delta dt)$ where the subscripts i and j are integers representing spatial

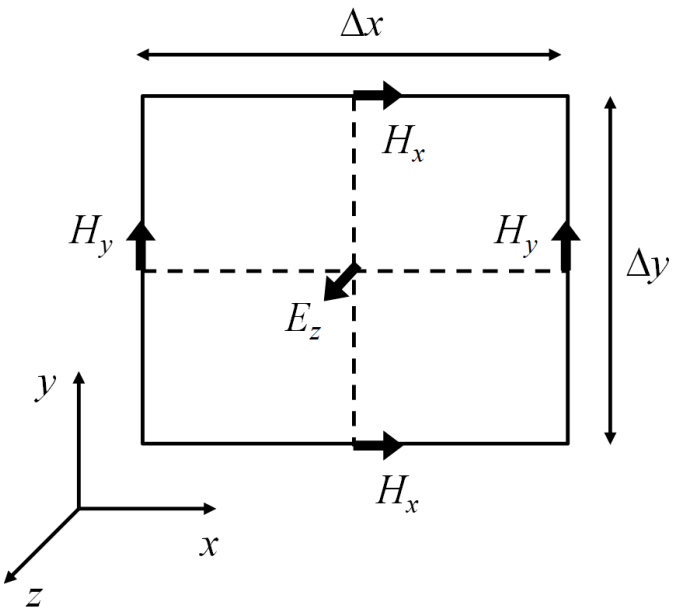

Figure 3.1: Two-dimensional unit cell in the FDTD TMz grid.

grid locations in the x and y direction respectively, and the superscript n is an integer representing the increment of the time step δt. For simplicity and since the geometry of the objects modelled in this work exhibits symmetry, square cells are used in this work where $\delta x = \delta y$. Second-order accurate central differences are used here; for example, the spatial discretisation of (3.21) around time step n yields:

$$\frac{\partial B_x}{\partial t}|^n_{i+1/2,j} \approx -\left(\frac{E_z|^n_{i+1/2,j+1/2} - E_z|^n_{i+1/2,j+1/2}}{\delta x}\right) \tag{3.24}$$

Time integration is achieved using a second-order accurate leapfrog algorithm where the magnetic flux density $\mathbf{B}$ is evaluated at time step n, which is then used to evaluate the electric field $\mathbf{E}$ at time step $n + 1/2$, and so forth. Applying this discretisation scheme and evaluating the time average of the electric field from:

$$E_z|^{n+1/2} = \frac{E_z|^n + E_z|^{n+1}}{2} \tag{3.25}$$

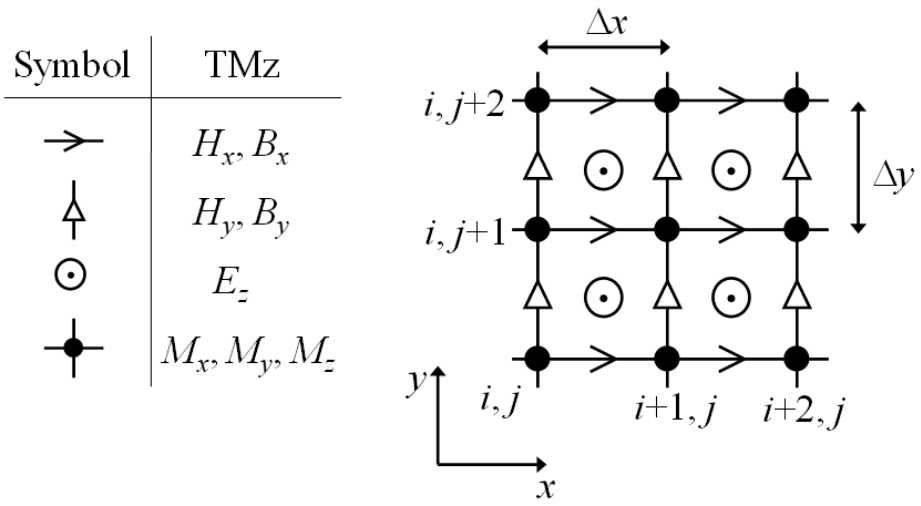

Figure 3.2: Efficient implementation of the magnetisation vector within the FDTD grid.

yields the explicit, discretised update equations for the TMz field components of equations:

$$\frac{\partial B_x}{\partial t}|^{n+1/2}_{i+1/2,j} = B_x|^{n-1/2}_{i+1/2,j} - \frac{\Delta t}{\Delta x}[E_z|^n_{i+1/2.j+1/2} - E_z|^n_{i+1/2,j-1/2}] \tag{3.26}$$

$$\frac{\partial B_y}{\partial t}|^{n+1/2}_{i+1/2,j} = B_y|^{n-1/2}_{i+1/2,j} + \frac{\Delta t}{\Delta x}[E_z|^n_{i+1/2.j+1/2} - E_z|^n_{i-1/2,j+1/2}] \tag{3.27}$$

$$E_z|^{n+1}_{i+1/2,j+1/2} = \left(\frac{1+\sigma\Delta t/(2\epsilon)}{1-\sigma\Delta t/(2\epsilon)}E_z|^n_{i+1/2,j+1/2} + \frac{\Delta t}{\Delta x(1+\sigma\Delta t/(2\epsilon)}\times\begin{bmatrix} H_y|^{n+1/2}_{i+1,j+1/2} - H_y|^{n+1/2}_{i,j+1/2} \\ -H_x|^{n+1/2}_{i+1,j+1/2} - H_x|^{n+1/2}_{i+1/2,j}\end{bmatrix} \tag{3.28}$$

where σ and ϵ are located in space at the same point as their respective field components and are therefore spatially varient. The magnetic field $\mathbf{H}$ in (3.28) is computed from (3.26) and (3.27) using the constitutive relation:

$$H^{n+1/2} = \begin{cases} \dfrac{B^{n+1/2}}{\mu_0} - M^{n+1/2} & \text{inside magnetic material} \\ \dfrac{B^{n+1/2}}{\mu_0\mu_r} & \text{outside magnetic material} \end{cases}$$

where μ_r is the relative permeability. The constitutive relation requires $\mathbf{M}$ to be

located at the same location in space as **H** and **B** (which are displaced by half-cell lengths in the FDTD grid). This requirement is in contradiction with the localised nature of the LLG equation where the magnetisation and field components need to be evaluated at the same location in space. If **M** is positioned at the same location in space as **H** and **B** then four-point spatial interpolations would be necessary to determine the **M** components at each of the half-cell displaced neighbouring field locations in the Yee cell [45, 46, 47]. This procedure is less accurate and makes the numerical implementation of magnetic boundary conditions more complex as the boundary of the magnetic material is not well defined.

A more efficient and simpler approach was developed by Aziz [43] where the magnetisation vector **M** is positioned at the corners of the Yee cell as indicated in Figure 3.2. For example, to determine the value of M_x at the same location as H_x or $B_x(i+1/2, j)$, the following two-point interpolation is used:

$$M_x|_{i+1/2,j}^{n+1/2} = \frac{M_x|_{i,j}^{n+1/2} + M_x|_{i,j}^{n+1/2}}{2}. \tag{3.29}$$

Similar interpolations can be carried out to evaluate the remaining magnetisation components at the same location as the magnetic field components for the FDTD update equations. Placing the magnetisation vectors at the corners of the FDTD cells, moreover, allows the same simple two point interpolations to be used in TEz and three-dimensional FDTD grids.

3.3.3 Numerical integration of the LLG equation and FDTD-LLG iterative algorithm

The time derivatives in the LLG equation at time step n may be approximated using central differences yielding:

$$\frac{\mathbf{M}^{n+1/2} - \mathbf{M}^{n-1/2}}{\Delta t} = -|\gamma|\left(\mathbf{M}^n \times \mathbf{H}_{eff}^n \mathbf{M}^n\right)\right) + \frac{\alpha}{M_s}\left(\mathbf{M}^n \times \frac{\mathbf{M}^{n+1/2} - \mathbf{M}^{n-1/2}}{\Delta t}\right) \tag{3.30}$$

Rewriting the time derivative term on the right-hand-side as:

$$\frac{\mathbf{M}^{n+1/2} - \mathbf{M}^{n-1/2}}{\Delta t} = \frac{\mathbf{M}^{n+1/2} + \mathbf{M}^{n+1/2} - 2\mathbf{M}^{n-1/2}}{\Delta t} \tag{3.31}$$

and expressing the magnetisation at time step n using the average:

$$\mathbf{M}^{n} = \frac{\mathbf{M}^{n+1/2} + \mathbf{M}^{n-1/2}}{2} \tag{3.32}$$

yields a second-order accurate update equation for the magnetisation at time step n:

$$\mathbf{M}^{n} = \mathbf{M}^{n+1/2} - \mathbf{M}^{n} \times \left(\frac{|\gamma|\Delta t}{2} \mathbf{H}_{eff}^{n}(\mathbf{M}^{n}) + \frac{\alpha}{M_s} \mathbf{M}^{n-1/2} \right) \tag{3.33}$$

where the effective field H_{eff} is defined as in previous sections of this thesis.

Equation (3.33) cannot be solved explicitly since the evaluation of the effective field requires M_n on the right-hand-side which is not available. The non-linear system of Maxwell and LLG equations therefore cannot be solved using an explicit scheme (unless anisotropy and exchange fields are ignored). An explicit numerical scheme based on extrapolation has been proposed in [48], however this scheme was found to be inherently unstable for small damping and is therefore not appropriate for dynamic and steady-state simulations. An implicit and stable iterative algorithm was proposed by Aziz [43] by combining the efficient grid implementation of the Maxwell-LLG equations and the implicit LLG solution in [42] and [49]. This FDTD-LLG numerical scheme proceeds as follows:

1) Evaluation of $\mathbf{B}_{n+1/2}$ from Maxwell's equations (3.26) an (3.27) using the previous computed values of the electric field $\mathbf{E}_n$ and magnetic flux density $\mathbf{B}_{n-1/2}$. Then the magnetic flux density at time step n can be computed from the time average:

$$\mathbf{B}^{n} = \frac{\mathbf{B}^{n+1/2} + \mathbf{B}^{n-1/2}}{2} \tag{3.34}$$

2) Evaluation of $\mathbf{B}_n$ at the grid locations of $\mathbf{M}$ (i.e. cell corners) using interpolations. For example, $\mathbf{B}_x$ is determined at the cell corner where $\mathbf{M}_x$ is located using the two-point spatial interpolation:

$$\mathbf{B}_x|^n_{i,j} = \frac{\mathbf{B}_x|^n_{i+1/2,j} + \mathbf{B}_x|^n_{i-1/2,j}}{2} \tag{3.35}$$

Similar interpolation is performed to determine $\mathbf{B}_y|^n_{i,j}$.

3) Iterative solution of the discretised LLG equation, re-written here in terms of the iteration number r:

$$[\mathbf{M}^n]^r = \mathbf{M}^{n-1/2} - [\mathbf{M}^n]^r \times \left(\frac{|\gamma|\Delta t}{2} \mathbf{H}^n_{eff}([\mathbf{M}^n]^{r-1} + \frac{\alpha}{M_s}\mathbf{M}^{n-1/2} \right) \tag{3.36}$$

with initial values $\mathbf{M}_n = \mathbf{M}_{n-1}$ and $\mathbf{H}_{eff} = \mathbf{H}^{n-1}_{eff}$.

Begin iteration r:

i) Solve equation (3.33) explicitly for $[M^n]^r$, using previous values $\mathbf{H}_{eff}([\mathbf{M}^n]^{r-1})$ and $\mathbf{M}^{n-1/2}$ as constants, at the grid corners using [42]:

$$\mathbf{M}^n = \frac{\mathbf{M}^{n-1/2} + (\mathbf{a} \cdot \mathbf{M}^{n-1/2}\mathbf{a} - \mathbf{a} \times \mathbf{M}^{n-1/2})}{1 + |\mathbf{a}|^2} \tag{3.37}$$

where

$$\mathbf{a} = -\left(\frac{|\gamma|\Delta t}{2} \mathbf{H}_{eff}([\mathbf{M}^n]^{r-1}) + \frac{\alpha}{M_s}\mathbf{M}^{n-1/2} \right) \tag{3.38}$$

ii) Update the exchange boundary conditions (in the absence of surface anisotropy) at the magnetic material interfaces using second-order central difference. For example, on the left hand boundary of the TMz grid in Figure 3.2, the magnetic boundary condition can be approximated by:

$$\frac{\partial \mathbf{M}}{\partial x}|_{i,j} \approx \frac{\mathbf{M}|_{i+1,j} - \mathbf{M}|_{i-1,j}}{2\Delta x} = 0 \tag{3.39}$$

This yields the boundary condition:

$$\mathbf{M}|_{i+1,j} = \mathbf{M}|_{i-1,j} \tag{3.40}$$

which is used for the finite-difference approximation of the exchange fields.

iii) Evaluate the exchange field using second-order accurate, central finite-difference approximations:

$$\mathbf{H}_{ex}|_{i,j} = \frac{2A}{\mu_0 M_s^2 \Delta x^2}\Big(\mathbf{M}|_{i+1,j} + \mathbf{M}|_{i-1,j} + \mathbf{M}|_{i,j+1} + \mathbf{M}|_{i,j-1} - 4\mathbf{M}|_{i,j}\Big) \tag{3.41}$$

where the last term on the right-hand-side of due to the spatially invarient magnetisation in the z-direction in the two-dimensional TMz mode. The magnetisation points located in free space on one side of the boundary are substituted using the exchange boundary condition.

iv) Update the effective field $\mathbf{H}^n_{eff}([\mathbf{M}^n]^r)$ using the computed values of $\mathbf{M}^n$ for the next iteration. The internal, Maxwell's field is computed using:

$$\mathbf{H}^n([\mathbf{M}^n]^r) = \mathbf{B}^n/\mu_0 - [\mathbf{M}^n]^r \tag{3.42}$$

End iterations.

4) Evaluation of $\mathbf{M}^{n+1/2}$ using extrapolation: $\mathbf{M}^{n+1/2} = 2\mathbf{M}^n - \mathbf{M}^{n-1/2}$

5) Evaluation of $\mathbf{M}^{n+1/2}$ at the locations of the $\mathbf{B}^{n+1/2}$ using two-point spatial interpolations, as described earlier, and then calculations of the magnetic field from:

6) Finally, evaluation of the electric field $\mathbf{E}^{n+1}$.

The iteration number r in the above algorithm was controlled to satisfy the convergence criterion that $|\bar{\mathbf{M}}^r|/|\bar{\mathbf{M}}^{r-1}| - 1 \leq \Gamma$ where the overbars indicate spatial averages over the magnetic material, and Γ is a small number representing the tolerance of the numerical solution of the magnetisation and is set equal to 1×10^{-6} in this work. This convergence criterion was satisfied using $2 - 6$ iterations; values of Γ less than

1×10^{-6} made negligible difference to the results. This scheme was found to be stable and limited only by the Courant stability limit of the FDTD method discussed next.

3.3.4 Numerical stability

The spatial increment Δx in the FDTD grid is normally chosen to sufficiently sample the shortest wavelength expected in the simulation (determined by the bandwidth of the source), and/or to accurately model the smallest dimension and/or physical and electromagnetic feature in the simulated materials (such as skin depth, exchange length or domain wall width in a magnetic material).

The numerical stability of the FDTD leapfrog time marching scheme is then well understood and imposes the following restriction on the time step size, known as the Courant limit, for stable time integration of Maxwell's equations [7,20]:

$$\Delta t \leq \frac{\Delta x}{c\sqrt{dim}} \tag{3.43}$$

where c is the speed of light in vacuum, and dim is the dimensionality of the system and is equal to 2 for the TMz mode considered here. The Courant stability criterion is normally more stringent to provide a small time step to ensure stability of the LLG solver and therefore of the complete FDTD-LLG iterative solver. Nevertheless it is useful to understand the correlation between the time step size necessary for the stability of the LLG equation finite-difference discretisation and the micromagnetic parameters of the material.

The stability analysis of the discretised LLG equation is complicated by the dependence on the sample shape, size and excited resonance modes in the material. Therefore simplified analysis are carried out here that consider mainly the exchange fields responsible for generating the high-frequency modes in the material, and therefore providing insight into the smallest time step needed for the stable numerical integration of the LLG equation. For this exercise, a semi-infinite (in the x and y

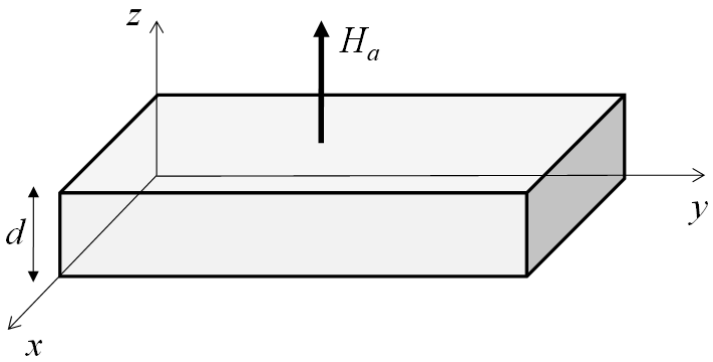

Figure 3.3: Magnetic thin-film geometry used in the numerical stability analysis of the Landau-Lifshitz equation.

directions) thin-film geometry with thickness d as shown in Figure 3.3 is considered for simplicity and to include dimensional parameters. A saturating, uniform static magnetic field H_a is applied normal to the surface of the film parallel to the z-axis as shown in 3.3, producing small pertubations in the magnetisation in the x and y directions with non-uniform spatial magnetic variations along the z-axis only. In this case, the Landau-Lifshitz equation without damping (where the focus here is on the undamped frequency modes) can be written as:

$$\frac{\partial \mathbf{M}}{\partial t} = \gamma \mathbf{M} \times \left(H_z \mathbf{z} + \frac{2A}{\mu_0 M_s^2} \frac{\partial^2 \mathbf{M}}{\partial z^2} \right) \tag{3.44}$$

where $\mathbf{M} = M_x\mathbf{x} + M_y\mathbf{y} + M_s\mathbf{z}$ with the small magnetisation perturbations M_x and M_y, and H_z is the effective field in the z-direction including the sum of the applied static field and demagnetising field normal to film plane. To proceed with the complex frequency analysis of the numerical stability of the Landau-Lifshitz equation, the following complex solutions of the magnetisation are assumed:

$$M_x = m_{x_0} e^{j(\omega t - kz)} \tag{3.45}$$

$$M_y = m_{y_0} e^{j(\omega t - kz)} \tag{3.46}$$

where ω is the complex angular frequency and k is the wavenumber along the thickness of the film. Substitution of the solutions (3.45)-(3.46) in Figure (3.44) and application of the exchange (unpinned) boundary condition $\partial \mathbf{M}/\partial z = 0$ in the absence of surface anisotropy yields the eigenvalues [35] $kd = p\pi$ where $p = 0, 2, 4, 6, ...$ with the first mode ($p = 0$) representing the fundamental or ferromagnetic resonance mode in the absence of exchange interactions.

Discretising (3.44) using second-order central differences and substituting (3.45)-(3.46) yields the two coupled equations:

$$j \sin(\omega \Delta t) m_{x0} = \gamma \Delta t m_{y0} \left[H_z - \frac{4A}{\mu_0 M_s \Delta^2} \big(-1 + \cos(k\Delta) \big) \right] \tag{3.47}$$

$$j \sin(\omega \Delta t) m_{y0} = -\gamma \Delta t m_{x0} \left[H_z - \frac{4A}{\mu_0 M_s \Delta^2} \big(-1 + \cos(k\Delta) \big) \right] \tag{3.48}$$

where Δt is the time increment and Δ is the space increment in the finite-difference approximation. The coupled equations can be solved for the complex frequency and yield:

$$\omega = \frac{1}{\Delta t} \sin^{-1} \Gamma \tag{3.49}$$

where:

$$\Gamma = \gamma \Delta t \left| H_z - \frac{2 L_x^2 M_s}{\Delta^2} (-1 + \cos(k\Delta) \right| \tag{3.50}$$

and $L_x = \sqrt{2A/\mu_0 M_s^2}$ is the exchange length. The complex frequency solutions for the magnetisation in (3.45)-(3.46) indicate that ω needs to be real with zero imaginary part for a stable (bounded) time evolution. This requires that $0 \leq \Gamma \leq 1$ which imposes the sampling time criterion for stability:

$$\Delta t \leq \frac{1}{\gamma \left| H_z - \dfrac{2 L_x^2 M_s}{\Delta^2} (-1 + \cos(k\Delta) \right|} \tag{3.51}$$

where the eigenvalues $kd = p\pi$ and p is an even integer. In the absence of exchange

interactions ($A = 0$) or at the fundamental mode $p = 0$, the sampling time is correctly determined by the ferromagnetic (precession) resonance frequency $\omega_0 = \gamma H_z$.

To compare the relative magnitudes of the time steps for stability in the FDTD and LL equations, the ratio of the Courant limit and (3.51) is evaluated at the same spatial increment of $\Delta = L_x$, and assuming that the magnetic material thickness is an integer multiple of the exchange length (i.e. $d = nL_x$). This ratio can be written as:

$$\frac{\Delta t_{FDTD}}{\Delta t_{LL}} \leq \frac{L_x}{c\sqrt{dim}}\gamma|H_z - 2M_s\big(-1 + \cos(p\pi/n)\big)| \tag{3.52}$$

Here, it can be seen that the ratio is well-below 1, indicating that the FDTD scheme is the primary limiting factor in determining the speed of the numerical algorithm.

Chapter 4

Exchange resonance in multilayered spherical particles

4.1 Introduction

There has been great interest in how surface anisotropy will alter the fundamental magnetic properties of nanostructures, which may emerge due to embedding magnetic particles in nonmagnetic matrices [50, 51], crystallographic arrangement on the surface [52], expansion and contraction of the lattice structure [53], among numerous other physical and chemical effects [54, 55]. As a consequence, surface magnetism of nanoparticles has been the subject of rigorous experimental [56, 57, 58] and theoretical [59, 60, 61] investigation. For example, surface anisotropy may be responsible for the high perpendicular magnetic anisotropy observed experimentally in thin epitaxial films of hcp cobalt [62, 63] and other multilayered ferromagnetic materials [64, 65]. When the surface anisotropy constant K_s is negative and of sufficiently large absolute value, the magnetisation vector can be orientated perpendicular to the film surface despite the presence of large demagnetizing fields, a phenomenon which is potentially useful for perpendicular magnetic recording.

Surface anisotropy may also play an important role in the size-dependent prop-

erties of ferromagnetic nanospheres. As discussed in the introduction, the dynamic permeability measurements of these spherical particles exhibit several narrow resonance bands which have been attributed to exchange resonance modes. These modes have been a source of great research interest due to their negligible eddy current loss [66] and have been adopted in the analysis of a wide range of material composites [67, 68, 69, 70, 71] in order to extract the magnetic parameters and estimate the surface contributions to the resonance frequency. The formula for exchange resonance modes was first derived by neglecting the magnetostatic contribution to the resonance, resulting in resonance frequencies which possess a $1/R_2^2$ dependence on the particle size, where R_2 is the outer radius of the sphere. This approximation is justified for sufficiently small particles when the exchange energy dominates over the magnetostatic energy, in contrast to the magnetostatic approximation in large particles, for which the exchange term is neglected.

Recently, the microwave properties of core-shell and magnetically hollow particles have been the subject of considerable interest [71, 72, 73, 74, 75] and the size dependent permeability of hollow nickel [76] and carbonyl iron [77] particles has been measured. A core-shell or multilayered particle offers tuneable electromagnetic properties, lighter weight and a wide frequency bandwidth at the cost of increased sensitivity of the ferromagnetic shell to surface imperfections.

Here, the exchange resonance theory is generalized within a rigorous micromagnetic framework in order to study the effect of surface anisotropy and a multilayered structure on the resonance frequency. This can provide detailed understanding into the high-frequency dynamics and improve accuracy when fitting measured permeability spectra to theoretical resonance curves.

4.2 Surface anisotropy

Néel proposed a phenomenological model of the magnetic surface anisotropy [78] to account for the breaking of crystallographic symmetry at the particle surface. Macroscopic expressions for the surface anisotropy energy density were later suggested by Brown [35] and Aharoni [79]. Here, we consider a uniaxial anisotropy density w_s of the form

$$w_s = K_s(1 - M_z^2) \tag{4.1}$$

where M_z is the z-component of the magnetisation. If the magnetisation $\mathbf{M}$ is assumed to be parallel to z before nucleation, the micromagnetic boundary conditions of (4.1) are given by the equations

$$\frac{\partial M_x}{\partial n} + \frac{2K_s}{C} M_x = 0 \tag{4.2}$$

$$\frac{\partial M_y}{\partial n} + \frac{2K_s}{C} M_y = 0 \tag{4.3}$$

where C is the exchange constant, K_s is the anisotropy constant and n is normal to the surface, which for a spherical particle is given by the spherical coordinate r. The linearised differential equations for the exchange modes are given by [80]

$$\left(\nabla^2 - \frac{M_s H_z}{C}\right) M_y + \frac{M_s}{\gamma_0 C} \frac{\partial M_x}{\partial t} = 0 \tag{4.4}$$

$$\left(\nabla^2 - \frac{M_s H_z}{C}\right) M_x - \frac{M_s}{\gamma_0 C} \frac{\partial M_y}{\partial t} = 0 \tag{4.5}$$

where M_s is the saturation magnetisation and C is the exchange constant. Assuming that a sufficiently large DC field is present to saturate the particle, then the expression H_z is given, for the case of a solid sphere, by

$$H_z = H_0 + \frac{2K_1}{M_s} \tag{4.6}$$

where H_0 is the external DC field applied parallel to an anisotropy easy axis, K_1 is the anisotropy constant for either uniaxial or cubic volume anisotropy, γ_0 is the gyromagnetic ratio, t is time. The boundary conditions for each surface, in the presence of surface anisotropy, are given by

$$\left(\frac{\partial M_x}{\partial r} - \frac{2K_{s_1}}{C}M_x\right)_{r=R_1} = 0 \tag{4.7}$$

$$\left(\frac{\partial M_y}{\partial r} - \frac{2K_{s_1}}{C}M_y\right)_{r=R_1} = 0 \tag{4.8}$$

$$\left(\frac{\partial M_x}{\partial r} + \frac{2K_{s_2}}{C}M_x\right)_{r=R_2} = 0 \tag{4.9}$$

$$\left(\frac{\partial M_y}{\partial r} + \frac{2K_{s_2}}{C}M_y\right)_{r=R_2} = 0 \tag{4.10}$$

Here, two surface anisotropy constants K_{s_1} and K_{s_2} are introduced, corresponding to the inner and outer boundaries, respectively. The general solution for the magnetisation components can be obtained by separation of the variables in terms of the spherical coordinates r, θ and ϕ, given by

$$M_x = e^{i\omega t}e^{is\theta}P_n^s(\cos\theta)\left(A_1 j_n\left(\frac{\mu r}{R_2}\right) + A_2 y_n\left(\frac{\mu r}{R_2}\right)\right) \tag{4.11}$$

$$M_y = e^{i\omega t}e^{is\theta}P_n^s(\cos\theta)\left(B_1 j_n\left(\frac{\mu r}{R_2}\right) + B_2 y_n\left(\frac{\mu r}{R_2}\right)\right) \tag{4.12}$$

where A, B, ω and μ are real constants, s and $n \geq s$ are integers and P_n^s is the Legendre function. Substituting equations (4.11) and (4.12) into equations (4.4) and (4.5) gives,

$$\left(\frac{\mu^2}{R_2^2} + \frac{M_s H_z}{C}\right)A_j + \frac{i\omega M_s}{\gamma_0 C}B_j = \frac{i\omega M_s}{\gamma_0 C}A_j - \left(\frac{\mu^2}{R_2^2} + \frac{M_s H_z}{C}\right)B_j = 0 \tag{4.13}$$

for $j = 1$ and 2. The determinant of the coefficients of A_j and B_j must be zero if (4.13) has a common, nonzero solution. Equating the determinants to zero gives,

$$\big(M_s H_z/C + \mu^2/R_2^2\big)^2 = (\omega M_s/\gamma_o C)^2 \tag{4.14}$$

The resonance frequencies ω are then given by,

$$\omega = \pm\gamma_0\big(C\mu^2/R_2^2 M_s + H_z\big) \tag{4.15}$$

Now, it is only necessary to fulfil the boundary conditions. At first there are four equations to solve, however the problem can be simplified by noting that the substitution of (4.14) into (4.13) gives,

$$iB_1 \pm A_1 = 0 \quad \text{and} \quad iB_2 \pm A_2 = 0 \tag{4.16}$$

The terms to be substituted into the boundary conditions can be calculated from the expressions (4.2) and (4.3), namely

$$\frac{\partial M_x}{\partial r} \pm \frac{2K_s}{C} M_x = e^{i\omega t} e^{is\theta} P_n^s(\cos\theta)\left(\frac{\mu}{R_2} A_1 \frac{\partial j_n(\mu r/R_2)}{\partial(\mu r/R_2)} + \frac{\mu}{R_2} A_2 \frac{\partial y_n(\mu r/R_2)}{\partial(\mu r/R_2)} \right.$$

$$\left. \pm \frac{2K_s}{C} A_1 j_n\left(\frac{\mu r}{R_2}\right) \pm \frac{2K_s}{C} A_2 y_n\left(\frac{\mu r}{R_2}\right) \right)$$

and

$$\frac{\partial M_y}{\partial r} \pm \frac{2K_s}{C} M_y = e^{i\omega t} e^{is\theta} P_n^s(\cos\theta)\left(\frac{\mu}{R_2} B_1 \frac{\partial j_n(\mu r/R_2)}{\partial(\mu r/R_2)} + \frac{\mu}{R_2} B_2 \frac{\partial y_n(\mu r/R_2)}{\partial(\mu r/R_2)} \right.$$

$$\left. \pm \frac{2K_s}{C} B_1 j_n\left(\frac{\mu r}{R_2}\right) \pm \frac{2K_s}{C} B_2 y_n\left(\frac{\mu r}{R_2}\right) \right)$$

Substituting the above two equations into (4.7-4.10) and using the relations (4.16) to substitute for B_1 and B_2, it is readily seen that to fulfil all boundary conditions, it is necessary and sufficient to fulfil only

$$e^{i\omega t}e^{is\theta}P_n^s(\cos\theta)\left(\frac{\mu}{R_2}A_1\frac{\partial j_n(\gamma)}{\partial\gamma}+\frac{\mu}{R_2}A_2\frac{\partial y_n(\gamma)}{\partial\gamma}\right.$$

$$\left.-\frac{2K_{s_1}}{C}A_1 j_n(\gamma)-\frac{2K_{s_1}}{C}A_2 y_n(\gamma)\right)_{\gamma=\frac{\mu R_1}{R_2}}$$

$$=e^{i\omega t}e^{is\theta}P_n^s(\cos\theta)\left(\frac{\mu}{R_2}A_1\frac{\partial j_n(\mu)}{\partial\mu}+\frac{\mu}{R_2}A_2\frac{\partial y_n(\mu)}{\partial\mu}\right.$$

$$\left.+\frac{2K_{s_2}}{C}A_1 j_n(\mu)+\frac{2K_{s_2}}{C}A_2 y_n(\mu)\right)$$

where we have defined $\gamma=\mu R_1/R_2$. By cancelling the $e^{i\omega t}e^{is\theta}P_n^s(\cos\theta)$ term and equating A_1 and A_2, these expressions can be re-written as

$$A_1\left(\frac{\mu}{R_2}\frac{\partial j_n(\gamma)}{\partial\gamma}-\frac{2K_{s_1}}{C}j_n(\gamma)\right)_{\gamma=\mu R_1/R_2}+A_2\left(\frac{\mu}{R_2}\frac{\partial j_n(\gamma)}{\partial\gamma}-\frac{2K_{s_1}}{C}j_n(\gamma)\right)_{\gamma=\mu R_1/R_2}$$
$$=A_1\left(\frac{\mu}{R_2}\frac{\partial j_n(\mu)}{\partial\mu}+\frac{2K_{s_2}}{C}j_n(\mu)\right)+A_2\left(\frac{\mu}{R_2}\frac{\partial j_n(\mu)}{\partial\mu}+\frac{2K_{s_2}}{C}j_n(\mu)\right)=0$$

Such a pair of equations has non-zero solution for A_1 and A_2 provided the determinant of their coefficients vanishes, leaving

$$\left(\frac{\mu}{R_2}\frac{\partial j_n(\mu)}{\partial\mu}+\frac{2K_{s_2}}{C}j_n(\mu)\right)\left(\frac{\mu}{R_2}\frac{\partial y_n(\gamma)}{\partial\gamma}-\frac{2K_{s_1}}{C}y_n(\gamma)\right)_{\gamma=\mu R_1/R_2}$$
$$-\left(\frac{\mu}{R_2}\frac{\partial y_n(\mu)}{\partial\mu}+\frac{2K_{s_2}}{C}y_n(\mu)\right)\left(\frac{\mu}{R_2}\frac{\partial j_n(\gamma)}{\partial\gamma}-\frac{2K_{s_1}}{C}j_n(\gamma)\right)_{\gamma=\mu R_1/R_2}=0.$$

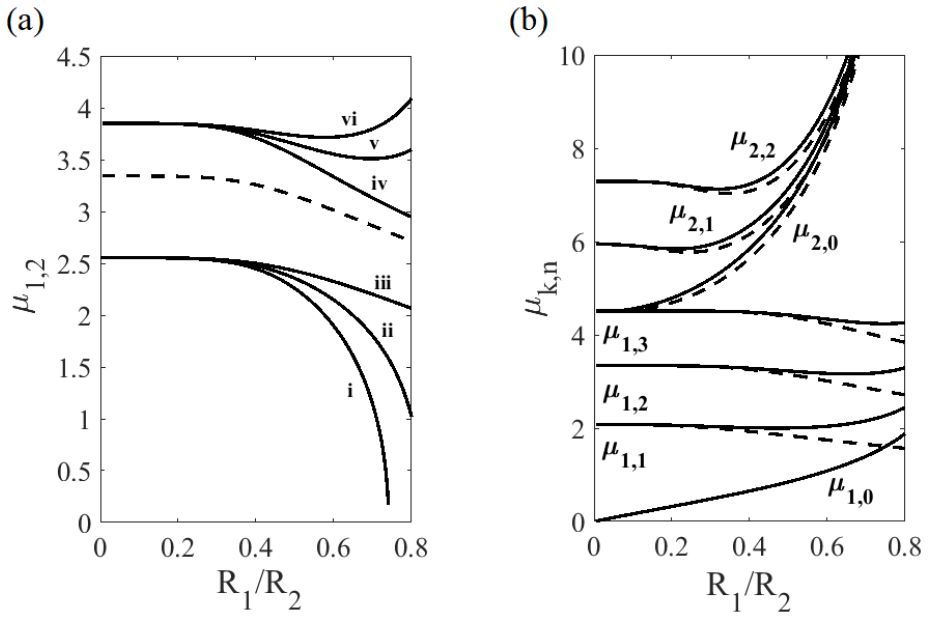

Figure 4.1: (a) $\mu_{1,2}$ plotted against the ratio R_1/R_2 for the condition $K_{s_2} = -4 \times 10^{-4}\,\mathrm{J\,m^{-2}}$ with (i) $K_{s_1} = -4 \times 10^{-4}\,\mathrm{J\,m^{-2}}$, (ii) $K_{s_1} = 0\,\mathrm{J\,m^{-2}}$ and (iii) $K_{s_1} = 4 \times 10^{-4}\,\mathrm{J\,m^{-2}}$ and $K_{s_2} = 4 \times 10^{-4}\,\mathrm{J\,m^{-2}}$ with (iv) $K_{s_1} = -4 \times 10^{-4}\,\mathrm{J\,m^{-2}}$, (v) $K_{s_1} = 0\,\mathrm{J\,m^{-2}}$ and (vi) $K_{s_1} = 4 \times 10^{-4}\,\mathrm{J\,m^{-2}}$ (b) μ_{kn} plotted against the ratio R_1/R_2 for $K_{s_2} = 0$, $K_{s_1} = 4 \times 10^{-4}\mathrm{J\,m^{-2}}$. In all cases the dashed line represents $K_{s_2} = K_{s_1} = 0$.
Reproduced from [81].

The eigenvalues μ_{kn} can be calculated from the transcendental equation above for different values of the outer radius R_2 and ratio R_1/R_2. For the case that $K_{s_1} = K_{s_2}$, when no surface anisotropy is present at either boundary, the expression reduces to

$$\left(\frac{\partial j_n(\mu)}{\partial \mu}\right)\left(\frac{\partial y_n(\gamma)}{\partial \gamma}\right)_{\gamma=\mu R_1/R_2} - \left(\frac{\partial y_n(\mu)}{\partial \mu}\right)\left(\frac{\partial j_n(\gamma)}{\partial \gamma}\right)_{\gamma=\mu R_1/R_2} = 0 \qquad (4.17)$$

which is the expression for the eigenvalues of the exchange resonance modes in a hollow ferromagnetic sphere when surface anisotropy is not present. It is readily seen that equation (4.17) introduces a dependence of the eigenvalues on the outer radius R_2, in addition to the ratio R_1/R_2.

4.3 Shell thickness

Here, we consider the case of iron particles with exchange constant $\frac{1}{2}C = 2.1 \times 10^{-11}$ J/m and $R_2 = 50$ nm. In thin films, absolute values of K_s have been found in the range $K_s = 0.6 - 4.5 \times 10^{-4}$ J/m^2 for FePt films [82] and $K_s = 1.7 - 9.6 \times 10^{-4}$ J/m^2 for different interfaces of iron at room temperature [83]. In this work, the surface anisotropy constants were chosen within the range of reported values for iron $K_s = 2 - 4 \times 10^{-4}$ J/m^2. The dependence of $\mu_{1,2}$ on shell thickness is shown in Figure 4.1(a) for different values of K_s. In the absence of surface anisotropy, the eigenvalues $k = 1, n = 1, 2, 3$ decrease with increasing R_1/R_2 (see Figures 4.1(a),(b)). This behaviour is modified for non-zero K_s, such that the eigenvalues can either increase or decrease with increasing R_1/R_2. In Figure 4.1(a), the mode rapidly tends to 0 with decreasing shell thickness when K_s is opposing the resonance. The situation is different for $k = 2$ eigenvalues (see Figure 4.1(b)). Here, surface anisotropy plays a less significant role in determining the dependence of the eigenvalues on shell thickness, because the eigenvalue equation (4.17) overwhelms the surface contribution even for large values of K_s .

In Figure 4.1(b), several of the eigenvalues μ_{kn} are plotted as a function of the ratio R_1/R_2 . The first eigenvalue $\mu_{1,0}$ is degenerate with the ferromagnetic resonance unless surface anisotropy is present. This eigenvalue is independent of the shell thickness for $K_s = 0$ but has an approximately linear dependence on R_1/R_2 in the range $R_1/R_2 = 0 - 0.6$ (see Figure 4.1(b)). In addition to shifting the frequency, surface anisotropy can deviate the magnetisation away from a homogenous single domain distribution. In Figure 4.1(b), the first $n = 0$ mode can be expected to gradually separate from the ferromagnetic resonance as the deviation from the single domain becomes more pronounced with decreasing shell thickness.

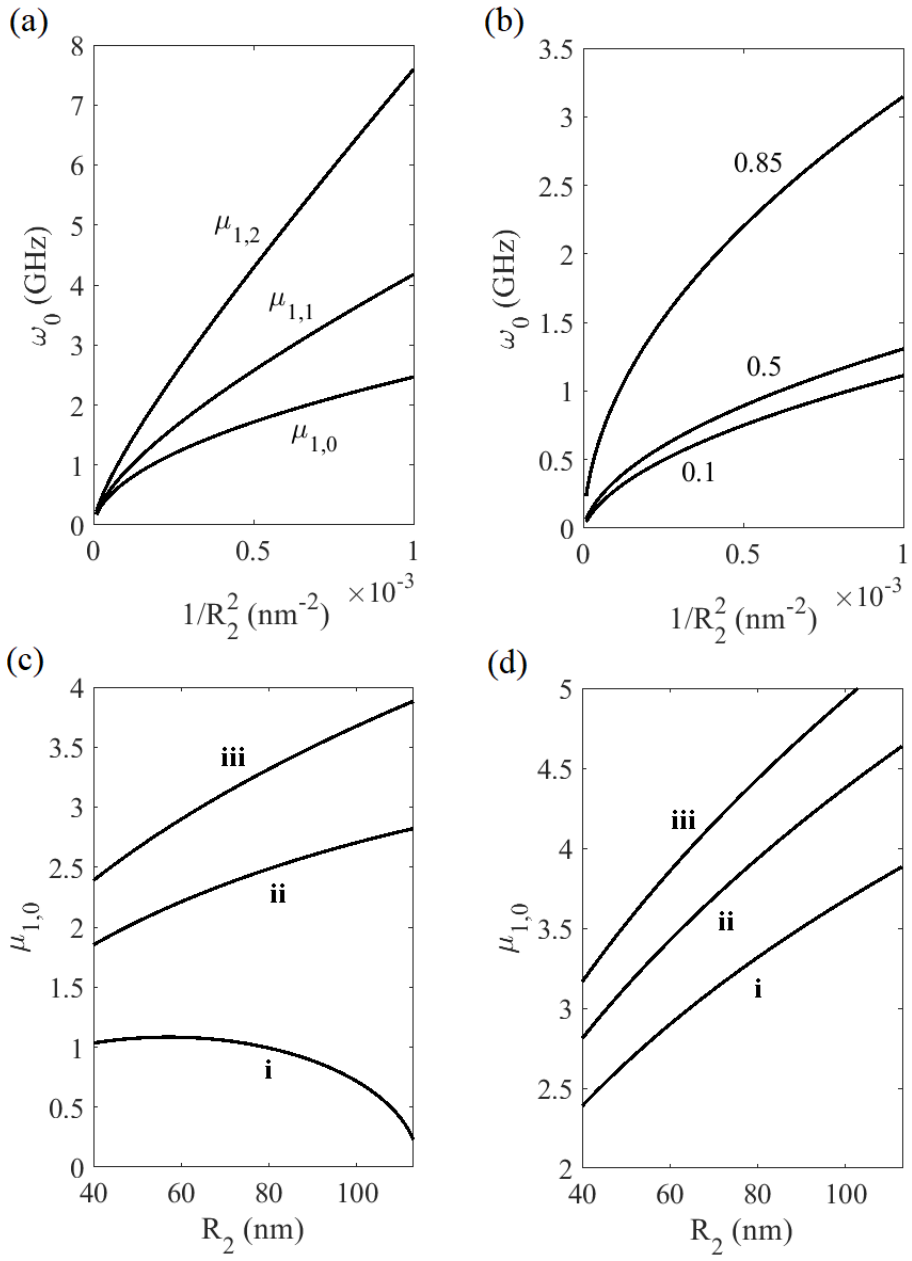

Figure 4.2: (a) $\mu_{1,n}$ plotted against $1/R_2^2$ for $K_{s_2} = 4 \times 10^{-4}\,\mathrm{J\,m^{-2}}, K_{s_1} = 0$ and $R_1/R_2 = 0.8$, where $\omega_0 = \gamma_0 C \mu_{1,n}/R_2^2 M_s$, (b) $\mu_{1,0}$ plotted against $1/R_2^2$ for $K_{s_2} = 4 \times 10^{-4}\,\mathrm{J\,m^{-2}}, K_{s_1} = 0$ and different values of R_1/R_2 , (c) $\mu_{1,0}$ plotted against R_2 for $R_1/R_2 = 0.85$, $K_{s_2} = 4 \times 10^{-4}\,\mathrm{J\,m^{-2}}$ and varying values of K_{s_1} (i) 0 $\mathrm{J\,m^{-2}}$, (ii) $-2 \times 10^{-4}\,\mathrm{J\,m^{-2}}$ and (iii) $-4 \times 10^{-4}\,\mathrm{J\,m^{-2}}$ and (d) the eigenvalue $\mu_{1,0}$ plotted against the outer radius R_2 for $R_1/R_2 = 0.85$, $K_{s_2} = 4 \times 10^{-4}\,\mathrm{J\,m^{-2}}$ and varying values of K_{s_1} (i) $0\,\mathrm{J\,m^{-2}}$, (ii) $2 \times 10^{-4}\,\mathrm{J\,m^{-2}}$ and (iii) $4 \times 10^{-4}\,\mathrm{J\,m^{-2}}$.
Reproduced from [81].

4.4 Size dependence

The eigenvalues μ have no dependence on R_2 when surface anisotropy is absent. A dependence on R_2 is introduced when the constants K_{s_2} and K_{s_1} are non-zero, such that the resonance frequencies are no longer strictly proportional to $1/R_2^2$. The deviation from the $1/R_2^2$ size dependence is shown in (see Figure 4.2(a),(b)) when surface anisotropy is present only at the outer boundary, which could correspond to the case when a coating is applied on the outer surface. In this situation, the dependence of the eigenvalues on R_2 decreases with decreasing particle size. Although the shift in the eigenvalues is decreasing with decreasing R_2, the shift in the frequency is greatly increasing due to the $1/R_2^2$ denominator in the expression for the frequency. However, the competition between different forms of surface anisotropy at each boundary can lead to more complex effects. In Figure 4.2(c), the surface anisotropy has a small impact on the eigenvalue $\mu_{1,0}$ for $R_2 = 115$ nm ($\mu_{1,0} \sim 0$) , but the dependence on R_2 becomes more pronounced with decreasing particle size. This is in contrast to the solid sphere for which the dependence of the eigenvalues on R_2 always decreases with decreasing particle size.

In Figure 4.2(b), the size dependence of the lowest exchange mode is shown for different values of the shell thickness. The size dependence of $\mu_{1,0}$ is close to that of the solid sphere for $R_1/R_2 = 0.5$ in Figure 4.2(b), but shows large deviation from the solid sphere for $R_1/R_2 = 0.85$. In Figure 4.2, the size dependence of this mode becomes pronounced as the shell thickness is decreased (see Figure 4.2(b)), particularly when supported by surface contributions at the inner boundary (see Figure 4.2(d)). As a result, the $\mu_{1,0}$ mode can potentially reach high frequencies in spherical shells due to the possibility of tuning the thickness.

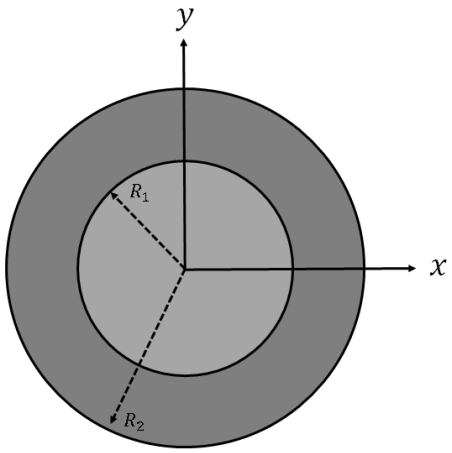

Figure 4.3: Simplified schematic of a core-shell particle.

4.5 Multilayered particles

The dynamical properties of ferromagnetic multilayers have been a source of interest for both fundamental research and for application in microwave devices. For example, multilayered spherical particles comprised of alternating concentric layers of iron and iron-carbide exhibit large permeability in the RF band, and are very sensitive to the microstructure of the multilayer [84]. In terms of device applications, having a multilayer instead of a single layer offers more degrees of freedom for controlling the instrinic electromagnetic properties. In order to understand the role of a multilayered structure on the resonance properties, here the exchange resonance theory is generalised to a core-shell particle.

Consider a homogeneous ferromagnetic sphere which occupies the region $0 \leq r \leq R_1$ and outer shell which occupies $R_1 \leq r \leq R_2$. The solution which satisfies the differential equations and is regular at $r = 0$ is

$$M_\theta = A_1 I_n(\mu r/R_1), \text{ for } 0 \leq r \leq R_1, \tag{4.18}$$

$$M_\theta = A_2 I_n(\mu r/R_1) + A_3 K_n(\mu r/R_1), \text{ for } R_1 \leq r \leq R_2, \tag{4.19}$$

where I_n and K_n are the modified spherical Bessel functions of the first and second

kind, respectively. Substituting the expressions for M_θ into the linearised differential equations (4.4)-(4.5) leads to the usual expression for the frequency, namely;

$$\omega = \gamma_0 \left(\frac{C\mu_i}{M_s R_1^2} + H_z \right) \tag{4.20}$$

It is convenient to express the eigenvalues μ_i in terms of the frequency,

$$\mu_1 = S_1(\omega - H_z)^{1/2} \text{ for } 0 \leq r \leq R_1, \tag{4.21}$$

$$\mu_2 = S_2(\omega - H_z)^{1/2} \text{ for } R_1 \leq r \leq R_2, \tag{4.22}$$

where μ_1 and μ_2 are the eigenvalues corresponding to the solid sphere and outer shell, respectively and $S_i = R_1(M_s/C)^{1/2}$. The solution must be continuous on the interface $r = R_1$, leading to

$$A_1 I_n(\mu_1) = A_2 I_n(\mu_2) + A_3 K_n(\mu_2) \tag{4.23}$$

The derivative $\partial M_\theta / \partial r$ must also be continuous at the interface $r = R_1$, hence

$$\mu_1 A_1 \frac{I_n(\mu_1)}{\partial \mu_1} = \mu_2 A_2 \frac{I_n(\mu_2)}{\partial \mu_2} + \mu_2 A_3 \frac{K_n(\mu_2)}{\partial \mu_2} \tag{4.24}$$

Finally, at the outer boundary we have the standard boundary condition $\partial \mathbf{M} / \partial n = 0$. Other assumptions are possible, such as the presence of surface anisotropy, however here this factor is neglected to avoid introducing too many variables. Then,

$$\mu_2 A_2 \frac{I_n(\mu_2 r / R_1)}{\partial x} + \mu_2 A_3 \frac{K_n(\mu_2 r / R_1)}{\partial x} = 0 \tag{4.25}$$

where $x = \mu_2 r / R_1$. Non-trivial solutions satisfying these equations exist if the deter-

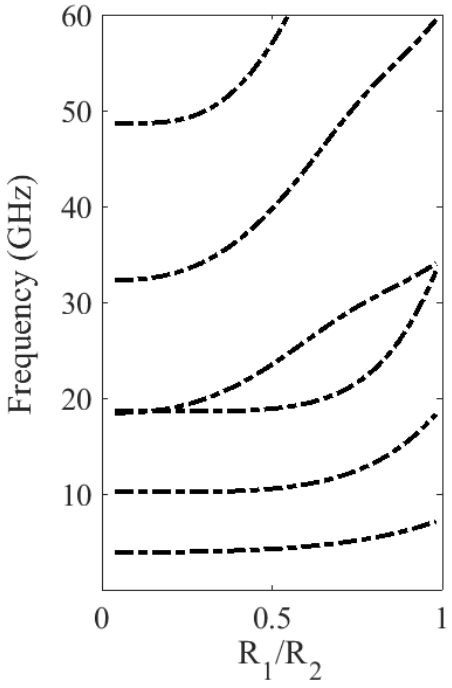

Figure 4.4: The frequency of the first 6 exchange modes plotted against the ratio R_1/R_2 for a core-shell particle of cobalt (core) and iron (shell) with $R_2 = 27.5$ nm. The cobalt core and iron shell have outer radius R_1 and R_2, respectively. R_2 is kept fixed while R_1 is increased, i.e. the cobalt core grows. The material parameters for iron were $M_s = 1.7 \times 10^6$ A/m, $C = 2.1 \times 10^{-11}$ J/m and for cobalt $M_s = 1.4 \times 10^6$ A/m, $C = 3 \times 10^{-11}$ J/m. The crystal structure was neglected for simplicity.

minant of the coefficients A_i vanish; hence,

$$\begin{vmatrix} I_n(\mu_1) & I_n(\mu_2) & K_n(\mu_2) \\ \mu_1 I_n(\mu_1)/\partial\mu_1 & \mu_2 I_n(\mu_2)/\partial\mu_2 & \mu_2 K_n(\mu_2)/\partial\mu_2 \\ 0 & \partial I_n(\mu_2 r/R_1)/\partial x & \partial K_n(\mu_2 r/R_1)/\partial x \end{vmatrix} = 0.$$

The exchange resonance frequency for each mode can be calculated by evaluating the determinant for any given n.

The spin wave spectrum for the first 6 modes is shown in Figure 4.4 for a cobalt-iron core-shell particle. The frequency of the spin wave modes for pure cobalt appear at higher frequencies than iron in accordance with the exchange resonance formula. As a result, an increase in frequency is observed for all modes in Figure 4.4 with increasing cobalt content. The eigenvalues $\mu_{1,3}$ and $\mu_{2,1}$ have very close values for a homogeneous solid sphere of any material property (see Figure 4.1(b)). As a result, they overlap in Figure 4.4 when the core-shell particle is comprised of either solid iron or cobalt. However, these modes separate when the particle is *inhomogeneous* with this separation becoming most pronounced for an inner cobalt radius of approximately 11 nm.

4.6 Summary

The eigenvalues of the exchange resonance modes were derived for the case of the spherical shell when assuming that surface anisotropy is present at both the inner and outer boundaries. The presence of surface anisotropy was found to play an important role in the dynamical properties of saturated nanoshells, and resulted in a range of different behaviours for lower-order ($k = 1$) eigenvalues. Relatively small values of K_s can rapidly drive these eigenvalues towards 0 with decreasing shell thickness, suggesting that surface anisotropy is an important factor to consider in the design of high-frequency microwave devices utilizing spherical shells. For higher-order modes

($k = 2$), surface anisotropy was found to play a more marginal role in determining the variation of the eigenvalues. The presence of surface anisotropy introduced a dependence of the first $n = 0$ mode on shell thickness, which led to a gradual increase in the eigenvalue with increasing R_1/R_2. For this mode, similar size-dependent behaviour to the solid sphere was observed up to a thickness of $R_1/R_2 \sim 0.5$ when surface anisotropy was present only on the outer boundary. However, substantial deviation from the size dependence of the solid sphere was observed as the shell thickness was decreased further. In addition to surface anisotropy, a generalised dynamical theory was presented for a core-shell nanoparticle and the spin-wave spectrum for an iron-cobalt multilayer was computed. The multilayer structure was found to remove the mixing between the eigenvalues $\mu_{1,3}$ and $\mu_{3,1}$ which closely overlap for a homogeneous sphere of any material property.

Chapter 5

Dynamic susceptibility of concentric rings

5.1 Introduction

Precise control of the magnetic susceptibility in the high-frequency range is necessary for microwave devices which require precise tunability of the resonance frequency of the uniform gyromagnetic mode [85]. Many studies have focused on the dynamic behaviour of nanometer size magnetic elements of varying shape [12, 86, 87, 88, 89]. The geometry of the magnetic element can significantly impact the dynamics and the hysteretic behaviour, and a variety of geometries have been investigated with the aim of developing the fastest and most reproducible switching mechanisms. Miniaturization of nanomagnets is of additional importance when designing novel magneto-electronic devices, such as logic or data storage mechanisms that utilise magnetic vortices. In addition to the geometry, the effect of magnetostatic interactions between rings when placed in close proximity, such as adjacent [90], concentric [91], or vertically stacked multilayers [92], can also significantly modify the hysteretic properties and lead to considerable changes in their dynamics.

In sufficiently thin magnetic disks a vortex appears as the ground state, where

the in-plane component of the vortex state is characterized by a clockwise or counter-clockwise magnetisation chirality. The polarity of the vortex is determined by an out-of-plane component of magnetisation at the central core of the vortex with two possible orientations $p = \pm 1$ which can be controlled by an external magnetic field aligned perpendicular to the disk plane. If a central hole is introduced into the disk, thus making it a nanoring, a core is no longer formed, which leads to an increase in the stability of the vortex at even smaller scales [93]. Recently, concentric ring structures have been proposed as multi-bit storage devices for MRAM technology where the vortex chirality (clockwise and counter-clockwise) of each ring can represent 0 or 1 in binary format [94]. Concentric rings have also been considered as contacts in spin injection devices for semiconductors which can utilise the properties of magnetic nanorings, such as low stray fields and high stability [95].

For a single thin-ring structure at remanence, a stable bidomain state called the onion state is observed with head-to-head and tail-to-tail domain walls [96]. When a magnetic field is applied parallel to the plane of the ring, one of the domain walls de-pins and moves toward the other domain until the onion state is annihilated and forms a vortex domain structure. As the magnetic field that is applied parallel to the plane of the ring is increased, the vortex state annihilates and forms an onion state of opposite polarity. A sudden drop in the hysteresis loop represents a cascade in magnetisation as the onion state is destroyed and converted to a vortex domain structure, reducing the overall magnetisation of the system. Onion-vortex and vortex-to-reversed-onion transitions correspond to irreversible jumps in the ferromagnetic resonance (FMR) spectra of thin ferromagnetic rings. In a concentric ring configuration, the magneto-static interactions between the rings determine the alignment of the head-to-head and tail-to-tail domain walls. For a sufficiently large saturation field, all the head-to-head domain walls are aligned in one half of the structure, while the tail-to-tail domains are aligned in the other half. When the external saturation field is decreased, the domain walls of each ring propagate in either clockwise or anticlockwise directions in

order to minimise the overall energy of the system. The annihilation of the clockwise and anticlockwise propagating domain walls then results in the formation of vortex domains of opposite chirality in each ring.

Here, we investigate the dynamic behaviour of concentric nanorings to explore the susceptibility spectrum as a function of geometric parameters of the system. The ferromagnetic resonance of the coupled ring structure is analysed and compared for different values of ring separation and their width. The micromagnetic investigation is carried out with the recently developed graphics processing unit (GPU) based solver MuMax3.

5.2 Hysteresis

In this work standard values of permalloy were chosen where the saturation magnetisation is given by $M_s = 8.6 \times 10^5$ A/m, exchange constant $A = 1.3 \times 10^{11}$ J/m, damping factor $\alpha = 0.01$, and negligible anisotropy with constant $K_1 = 0$. The cell-size was chosen to be $x = y = 4$ nm which is less than the exchange length of permalloy. The cell-size in the z-direction was chosen to be 20 nm as the rings are too thin compared to the other dimensions in the ring structure to support a significant out-of-plane magnetisation component. The effect of magnetostatic coupling on the static behaviour of concentric rings was investigated for an inner ring with an outer diameter of 500 nm, a width of 100 nm, and a thickness of 20 nm with varying outer ring parameters. The rings were initially saturated with an external biasing field applied in the y-direction. The magnetisation M_y was recorded as the field was swept in the region of $H_y = -1000$ Oe and $H_y = 1000$ Oe in steps of 10 Oe. The hysteresis curves for the inner and outer rings of a concentric system are shown individually in Figure 5.1(a). Here, the average normalised magnetisation $M_y = M_s$ for the entire concentric system, which includes both the inner and outer rings, is represented as the dashed black line. As the field is decreased in strength, switching occurs at larger field

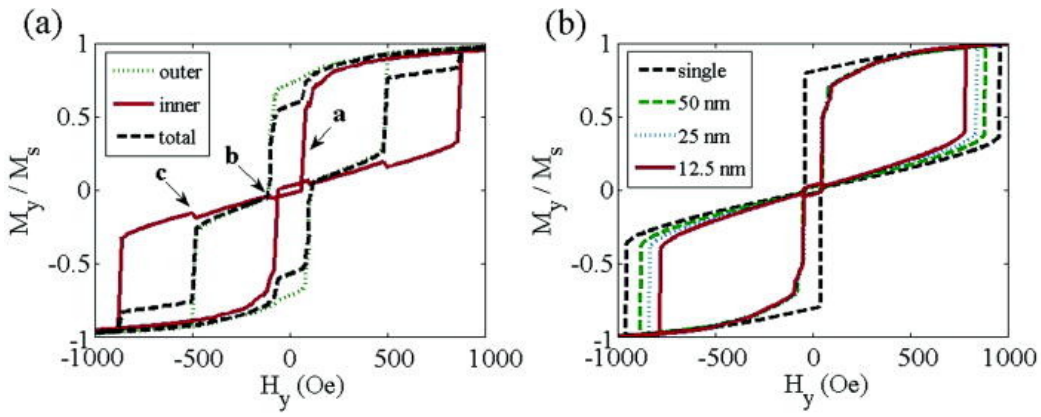

Figure 5.1: (a) Hysteresis loop for the outer ring (green), inner ring (red), and total concentric system (black). The outer ring has an outer diameter of 1000 nm, a width of 200 nm, and a thickness of 20 nm. The inner ring has an outer diameter of 500 nm, a width of 100 nm, and a thickness of 20 nm. (b) Hysteresis loop for a ring of an outer diameter of 500 nm, a width of nm, 100 and a thickness of 20 nm interacting with an outer ring with a width of 100 nm and a thickness of 20 nm for ring separations of 50 nm (green), 25 nm (blue), and 12.5 nm (red). The dashed black line represents a single ring with an outer diameter of 500 nm, a width of 100 nm, and a thickness of 20 nm for which no magnetostatic coupling is present.
Reproduced from [97].

strengths for the inner ring due to the smaller width and increased shape anisotropy when compared with the outer ring. The point "a" in Figure 5.1 (a) corresponds to a mixed onion-vortex state where each of the inner and outer rings possesses vortex and onion domain states, respectively.

This is in contrast to single nanorings for which the onion state exists as a metastable domain structure and onion-vortex transitions require a non-zero external biasing field. As the external field is reversed, the outer ring undergoes a transition from the onion to vortex domain (see point "b" in Figure 5.1 (b)). In addition, small drops and jumps in the hysteresis loop of the inner ring are found to occur at the point of magnetisation switching for the outer ring [see, for example, point "c" in Figure 5.1 (a)] due to the long-range magnetostatic interactions between rings. The effect of different ring separations on the hysteretic behavior is shown in Figure 5.1 (b). Here, the vortex-to-onion transitions can be seen to vary as a function of the ring separation. A decrease in the separation between each ring results in a decrease

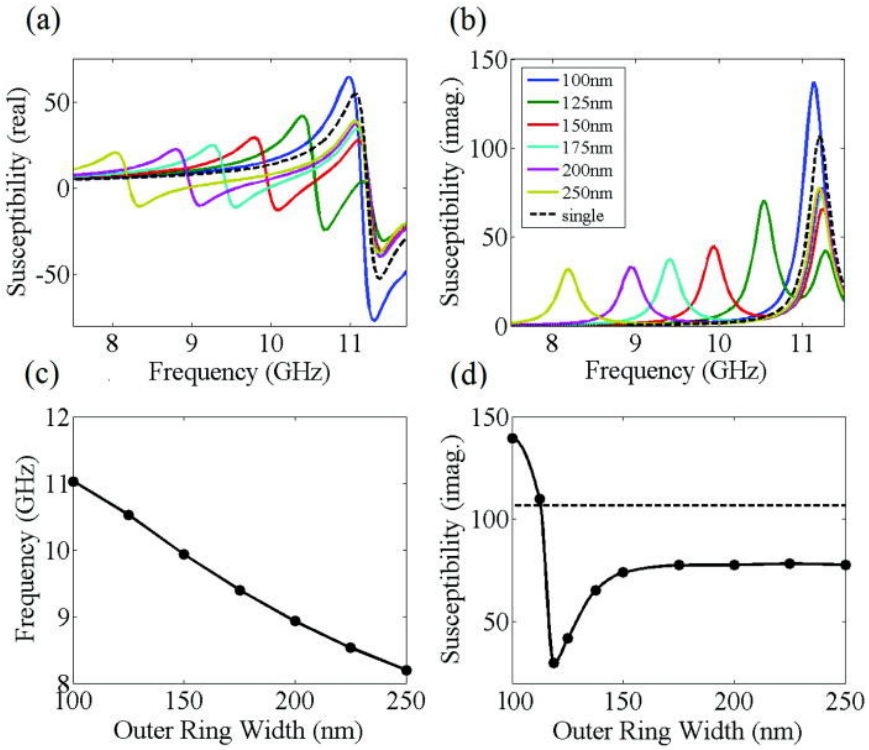

Figure 5.2: (a) Real and (b) imaginary components of the susceptibility for an inner ring with an outer diameter of 500 nm, a width of 100 nm, and a thickness of 20 nm interacting with an outer ring with an inner diameter of 800 nm and a thickness of 20 nm. The inner ring is kept fixed while the width of the outer ring is varied in the region of 100 nm−250 nm. (c) The frequency of the ferromagnetic resonance of the outer ring with an inner diameter of 800 nm and a thickness of 20 nm plotted against the width. (d) The amplitude of the imaginary component of the susceptibility for the inner ring with an outer diameter of 500 nm, a width of 100 nm, and a thickness of 20 nm plotted against the width of the outer ring. The dashed line represents the amplitude of the susceptibility corresponding to the ferromagnetic resonance of the inner ring when no magnetostatic coupling is present.
Reproduced from [97].

in the threshold field strength required to induce switching of the domains.

5.3 Ring width

The impact of magnetostatic coupling on the high-frequency dynamic susceptibility of concentric rings was investigated as a function of the ring width. The concentric rings were relaxed into vortex domains of opposite chirality for an inner ring with an outer diameter of 500 nm, a width of 100 nm, and a thickness of 20 nm that was interacting with an outer ring with an inner diameter of 800 nm, a thickness of 20 nm, and the width varied in the region of 100 nm−250 nm. The stable state of the total system was excited with a Gaussian pulse of strength $H_y = 5$ Oe. The system was excited by applying a Gaussian pulse of width ≈ 5 ps in the y-direction and the evolution of the y-component of the magnetisation $M(t)$ was recorded with respect to time. A weak pulse was chosen ($H_{ext} = 5$ Oe) to ensure excitation occurs within the linear region of the system. The average susceptibility $\chi(\omega)$ was determined from the ratio of the Fourier transform of the y-component of the average magnetisation $M(t)$ and Fourier transform of the applied field,

$$\chi(\omega) = \frac{M(\omega)}{H(\omega)} \tag{5.1}$$

Here $M(\omega)$ and $H(\omega)$ are the Fourier transform of the average magnetisation and applied field, respectively. The spatial susceptibility was calculated from the Fourier transform of the magnetisation along the direction of excitation for every cell in the simulation grid.

The influence of varying the outer ring width on the dynamic susceptibility of the inner ring is shown in Figure 5.2(a) and Figure 5.2(b). The width of the outer ring is varied in the range of 100 nm−250 nm, while all geometric parameters of the inner ring are kept fixed. Two modes are pronounced in the susceptibility spectrum for the inner ring: a lower frequency mode corresponding to the uniform resonance of the

outer ring which stems from magnetostatic interactions between the concentric rings and the second at 11.5 GHz corresponding to the uniform resonance of the inner ring. This can be confirmed analytically by approximating each arm of the inner/outer ring by an elliptic cylinder saturated in the x direction, in which case the uniform resonance frequency can be readily shown to be [35]

$$\omega_r = \gamma M_s \sqrt{N_y N_z} \tag{5.2}$$

where $N_y = T/(W+T)$ and $N_z = W/(W+T)$ are the demagnetising factors of the ring arms with width W and thickness T. Substituting the dimensions of the inner ring yields a resonance frequency of 11.3 GHz, in agreement with micromagnetic simulations.

Increasing the width of the outer ring leads to a decrease in the frequency of the uniform resonance of the outer ring (see Figure 5.2(c)), which in turn leads to a decrease in frequency for the corresponding mode in the susceptibility spectrum of the inner ring (see Figure 5.2(b) and Figure 5.2(c)). The frequency of the uniform resonance mode of the inner ring at 11.5 GHz remains largely unchanged with varying outer ring widths at this separation. However, a large variation in the maximum amplitude of the susceptibility can be observed with varying outer ring widths (see Figure 5.2(d)). For an outer ring width of 100 nm, where the eigenfrequencies of each individual ring are similar, there is enhancement of the amplitude of oscillation corresponding to the uniform resonance of the inner ring (see Figure 5.2(d)). When the system is perturbed by pulse excitation, the demagnetising field acts to align the magnetisation anti-parallel in each adjacent ring, resulting in frequency beating and modulation (see 5.5).

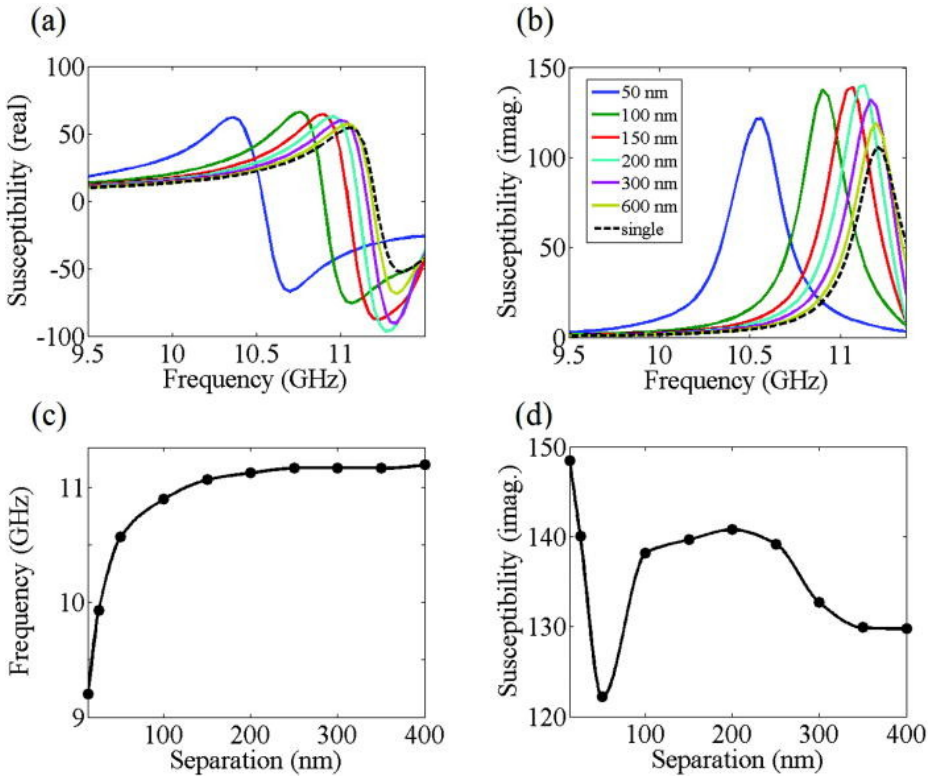

Figure 5.3: (a) Real and (b) imaginary components of the susceptibility for an inner ring with an outer diameter of 500 nm, a width of 100 nm, and a thickness of 20 nm interacting with an outer ring with a width of 100 nm, a thickness of 20 nm, and a ring separation in the range of 50-600 nm. (c) The frequency of the ferromagnetic resonance of the inner ring with an outer diameter of 500 nm, a width of 100 nm, and a thickness of 20 nm plotted against the ring separation. (d) The amplitude of the imaginary component of the susceptibility corresponding to the ferromagnetic resonance for the inner ring plotted against the ring separation.
Reproduced from [97].

5.4 Ring separation

The width of the outer ring is kept fixed at 100 nm to investigate the effect of ring separation for a pair of concentric rings. A thickness of 20 nm is chosen again for each ring, and the separation is varied in the region of $10 - 600$ nm, while all geometric parameters of the inner ring are kept fixed. The initial magnetisation state and dynamic susceptibility were calculated as in the previous section. The amplitude of oscillation corresponding to the uniform resonance of the inner ring is found to depend in a complex way on the ring separation. The imaginary component of the

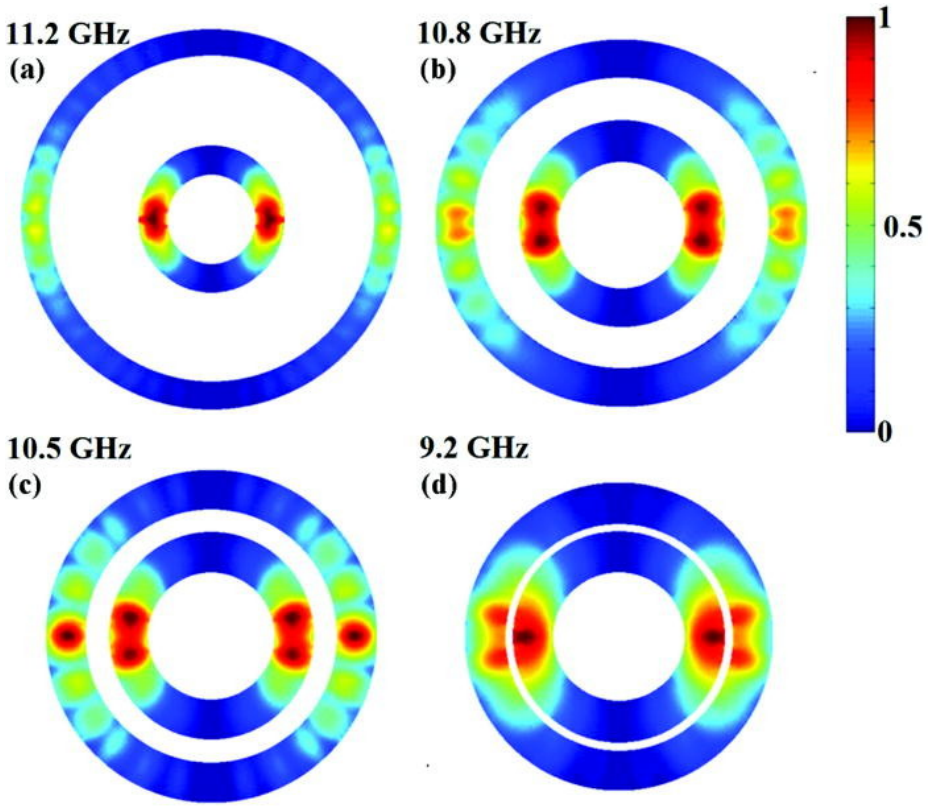

Figure 5.4: normalised spatial Fourier transform of the y-component of the magnetisation following pulse excitation for concentric rings with a width of 100 nm, a thickness of 20 nm, and ring separations of (a) 300 nm, (b) 100 nm, (c) 50 nm, and (d) 12.5 nm. The outer diameter and thickness of the inner ring are kept fixed at 500 nm and 20 nm, respectively. The frequencies shown in (a)-(d) represent the ferromagnetic resonance frequency of the inner ring for each ring separation.
Reproduced from [97].

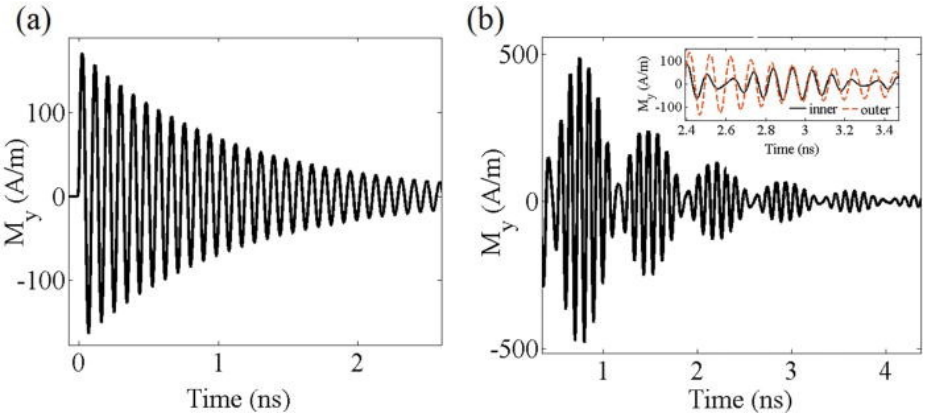

Figure 5.5: (a) The y-component of the magnetisation following pulse excitation for a single ring with an outer diameter of 500 nm, a width of 100 nm, and a thickness of 20 nm. (b) The y-component of the magnetisation following pulse excitation for an inner ring with an outer diameter of 500 nm, a width of 100 nm, and a thickness of 20 nm coupled with an outer ring. The outer ring has an outer diameter of 1000 nm, a width of 150 nm, and a thickness of 20 nm. The magnetisation response $M_y(t)$ of the inner (black) and outer (orange) ring is shown in the inset in (b).
Reproduced from [97].

susceptibility increases in amplitude with reducing separation from 400 nm to 100 nm, reaching a local maximum amplitude at 200 nm, before decreasing and reaching a local minimum at 50 nm (see Figures 5.3(a), 5.3(b), and 5.3(d)). For separations smaller than 50 nm, the susceptibility again increases, reaching a maximum value at 12.5 nm (see Figure 5.3(d)). The shift in the frequency of the uniform resonance mode of the inner ring is found to decrease with increasing ring separation (see Figure 5.3(c)). The frequency of the ferromagnetic resonance mode tends towards the dashed black line (representing a single nanoring) with increasing separation in Figures 5.3(a) and 5.3(b), as the magnetostatic interaction between the concentric rings becomes vanishingly small.

The normalised spatial distribution of the ferromagnetic resonance for the inner concentric ring is shown in Figure 5.4 for varying ring separations. Here, the Fourier transform of the y-component of the magnetisation is calculated following pulse excitation for every cell in the simulation grid. The amplitude of the dynamic susceptibility is found to depend in a complex way on the variation of the spatial

localization of the uniform mode. In Figure 5.4, the frequencies shown in (a)−(d) correspond to the frequency of the ferromagnetic resonance mode of the inner ring, which shifts downwards in frequency with decreasing ring separation. Spatially inhomogeneous resonance modes emerge in the outer ring at these frequencies, resulting from the longrange stray fields which decay across the width of the outer ring.

5.5 Summary

The high-frequency dynamic susceptibility of concentric permalloy nanorings with vortex domain structures with a thickness of 20 nm, a width in the range of 100 nm−250 nm, and a separation in the range of 10 nm−600 nm was investigated by micromagnetic simulations. The frequency of oscillation was found to be significantly impacted by the magnetostatic interaction between concentric nanorings and could be modulated by a variation in the ring separation and width. The variation in amplitude of the real and imaginary components of the dynamic susceptibility was found to correspond to a variation in the spatial distribution of the ferromagnetic resonance mode. An increase in the amplitude of the dynamic susceptibility at the ferromagnetic resonance frequency was observed for concentric nanorings with similar eigenfrequencies and dimensions.

Chapter 6

Role of domain structure in microwave absorption

6.1 Introduction

The microwave properties of ferromagnetic spheres have been the focus of rigorous theoretical and experimental study. Walker developed the theory of magnetostatic modes in ellipsoidal samples for which spheres are a special limiting case [98]. The magnetostatic approximation agreed quantitatively with the early generation of ferromagnetic resonance (FMR) experiments, which were carried out on spheres whose radii were macroscopic, and for which the exchange contribution was negligible. However, the microwave response of very small ferromagnetic nanospheres can be influenced by the exchange interaction when their radii lie in the range of the exchange length [27] $L_{ex} = \sqrt{(2A/\mu_0 M_s^2)}$ where A is the exchange constant and M_s is the saturation magnetisation. A broad range of microwave composites contain spherical particles in this size range. Thus, it became necessary to extend the previous theories of magnetostatic modes in ferromagnetic spheres to include exchange and dipolar interactions [39, 99, 100].

Ferromagnetic hollow spheres exhibit a number of well-defined magnetisation con-

figurations such as the single-domain, two-domain, four-domain and vortex-curling domain [28], where the single and vortex domains are predicted to exist as ground states below a critical radius. As discussed in previous sections, the magnetic vortex appears as a ground state due to competition between short-range exchange interactions and long-range dipolar interactions. In addition to the vortex and single domain, an additional intermediary state was proposed and confirmed as a ground state, where the direction of the magnetisation deviates away from the single domain distribution at each local point [101]. This domain structure is a three-dimensional analogue of the well-known onion state found in ring elements [102]. However, a detailed knowledge of the relationships between particle shape and size distribution, morphology, and the resulting physical properties of nano-sized magnetic structures is still lacking. In particular, the microwave response of the vortex domain is important for size ranges in which it is predicted to exist as the ground state (above $2R \approx 40$ nm) for monodisperse particles.

The majority of studies of magnetic vortex dynamics have focused on thin structures. In relatively thick magnetic structures ($\approx$ 80 nm) the magnetisation can vary non-uniformly across the thickness of the element, resulting in complex three-dimensional dynamics such as non-uniform domain and spin-wave excitations [103, 25]. These fully three-dimensional dynamics are not well described by traditional analytic treatment and require micromagnetic simulations to resolve accurately. Magnetic vortex dynamics have been studied intensively in planar structures, with only recent studies of low frequency vortex dynamics in nanospheres [104, 105]. In this chapter, numerical micromagnetic simulations are used to investigate the dyamical properties of hollow spherical shells with single/onion and vortex domain structures in the linear regime.

6.2 Onion domain

For high permeability microwave applications it is necessary to use materials which possess a large saturation magnetisation such as cobalt, iron or their alloys. In this section standard values of iron were chosen where $M_s = 1.7 \times 10^6$ A/m, $\alpha = 0.01$, exchange constant $\frac{1}{2}C = 2.1 \times 10^{-11}$ J/m and cubic anisotropy constant $K_1 = 4.7 \times 10^4$ J/m^3. The system was excited by applying a Gaussian pulse of width ≈ 5 ps in the y-direction and the evolution of the y-component of the magnetisation $M(t)$ was recorded with respect to time. A weak pulse was chosen ($H_{ext} = 5$ Oe) to ensure excitation occurs within the linear region of the system. The average susceptibility $\chi(\omega)$ was determined from the ratio of the Fourier transform of the y-component of the average magnetisation $M(t)$ and Fourier transform of the applied field

$$\chi(\omega) = \frac{M(\omega)}{H(\omega)} \tag{6.1}$$

Here $M(\omega)$ and $H(\omega)$ are the Fourier transform of the average magnetisation and applied field, respectively. The spatial susceptibility was calculated from the Fourier transform of the magnetisation along the direction of excitation for every cell in the simulation grid.

The higher order modes will be explained using the exchange resonance theory discussed in the previous sections. Assuming that a sufficiently large DC field is present to saturate the particle, then the expression for the exchange resonance frequency is given by

$$\omega = \gamma_0 \left(\frac{C\mu_{kn}}{M_s R_2^2} + H_z \right) \tag{6.2}$$

where $C = 2A$ is the exchange constant, R_2 is the outer radius, M_s is the saturation magnetisation, μ_{kn} are the eigenvalues and H_z is the potential due to the z component of the magnetisation. The expression for H_z is given, for the case of a solid sphere,

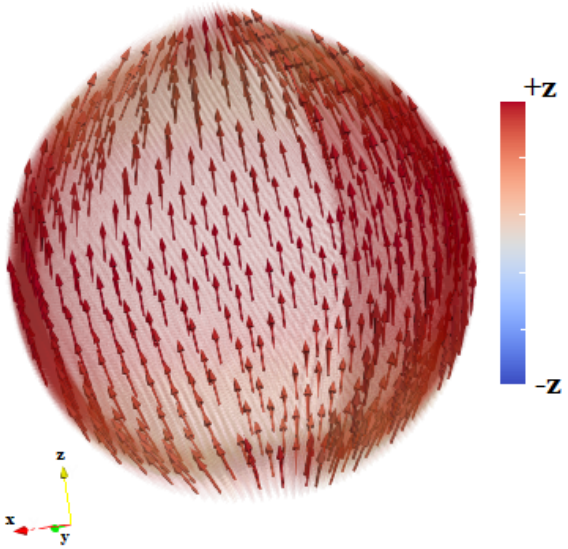

Figure 6.1: Magnetisation configuration for the onion domain structure in a spherical shell of outer diameter 55 nm and ratio $R_1/R_2 = 0.8$ when the external DC field is applied along the z axis. Colorbar represents the normalised z component of the magnetisation.

by

$$H_z = H_0 + \frac{2K_1}{M_s} \tag{6.3}$$

where H_0 is the external DC field applied parallel to an anisotropy easy axis and K_1 is the anisotropy constant for either uniaxial or cubic volume anisotropy. For the spherical shell the eigenvalue equation, in the absence of surface anisotropy, is given by [81]

$$\begin{aligned} &\left(\frac{\partial j_n(\mu)}{\partial \mu}\right)\left(\frac{\partial y_n(x)}{\partial x}\right)_{x=\mu r/R_2} \\ -&\left(\frac{\partial y_n(\mu)}{\partial \mu}\right)\left(\frac{\partial j_n(x)}{\partial x}\right)_{x=\mu r/R_2} \\ &= 0 \end{aligned} \tag{6.4}$$

where j_n and y_n are spherical Bessel functions of the first and second kind, respectively.

The shell particles were saturated by applying a 0.8 T biasing field along the z-axis and pulsing the system in the orthogonal y-direction. The stable magnetisation

configuration is shown in Figure 6.1. An ideal single domain state is forbidden in spherical shells even when a large DC field is applied [27]. As a result, an onion-like magnetisation is present as the stationary configuration (see Figure 6.1). Figure 6.2 shows the spatial Fourier modes and dynamic susceptibility of the hollow sphere when saturated with a 0.8 T field applied in the z-direction. The lowest frequency mode f_1 in Figure 6.2(c) is the ferromagnetic resonance, which corresponds to the largest amplitude in the imaginary component of the numerically calculated susceptibility. The frequency of this mode is simply given by the second term H_z in equation (6.2). Substituting the values for the saturating field and magnetocrystalline anisotropy gives a frequency of 23.97 GHz in agreement with the numerically simulated value of 24 GHz for the ferromagnetic resonance of the solid sphere. Above the ferromagnetic resonance, several non-evenly spaced resonance modes can be observed in Figure 6.2(c) all of which exhibit a $1/R_2^2$ dependence on the outer radius consistent with the exchange resonance equation.

The frequency of the ferromagnetic resonance is independent of the particle size for the solid sphere (see Figure 6.3(b), black line), but shows a size dependence for the shell which becomes increasingly pronounced as the thickness is decreased (see Figure 6.3(b), dashed lines). This size dependence of the ferromagnetic resonance emerges as the magnetisation gradually deviates away from the single domain state with increasing R_1/R_2, forming an "onion-like" domain in shells due to the strong demagnetising field. Here, the contribution of the demagnetising field to the resonance frequency becomes important. The ferromagnetic resonance of the shell tends towards the ferromagnetic resonance of the solid sphere, as the onion state field distribution tends towards that of the single domain with decreasing particle size.

The lowest order exchange mode requires special attention. It is the second solution of $\mu = 0$ with the same frequency as the ferromagnetic resonance. This mode should be independent of R_1/R_2 according to the eigenvalue equation, but shows a gradual increase in frequency with decreasing shell thickness. The degeneracy of this

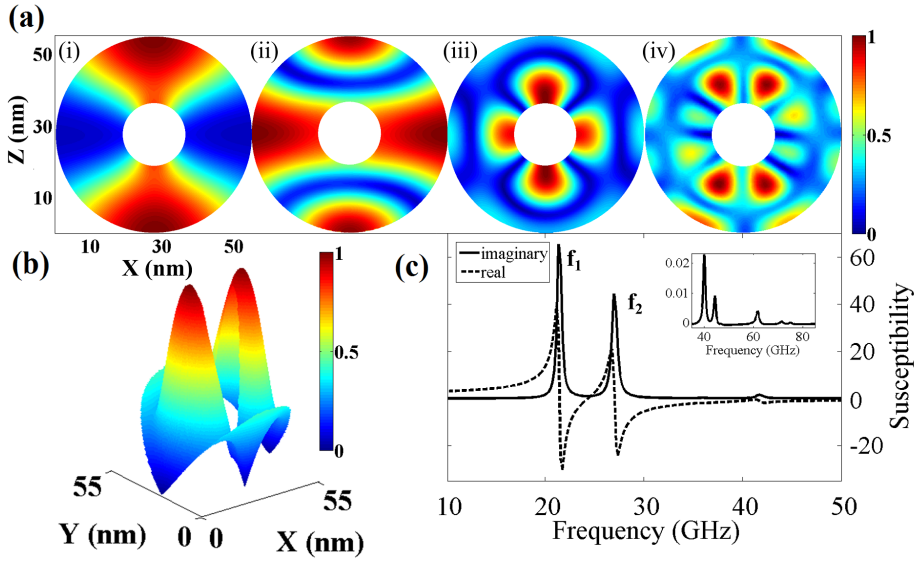

Figure 6.2: (a) Normalised spatial Fourier transform of the y-component of the dynamic magnetisation for a hollow iron sphere with $R_2 = 27.5$ nm and $R_1/R_2 = 0.3$ in the presence of a 0.8 T biasing field applied in the z-direction. The frequencies correspond to (i) 23.1 GHz, (ii) 25.6 GHz, (iii) 63 GHz and (iv) 110 GHz in the xz-plane. (b) Three-dimensional surface plot of the normalised spatial Fourier transform for the xy cross-section at 110 GHz, corresponding to Fig. 1(a), (iv). (c) Real and imaginary components of the average dynamic susceptibility corresponding to the y-component of the dynamic magnetisation for a hollow sphere with $R_2 = 27.5$ nm and $R_1/R_2 = 0.4$ in the presence of a 0.8 T biasing field applied in the z-direction. Inset shows enlargement of the data for the average susceptibility at higher frequencies taken at the cross-section in the xz-plane. f_1 and f_2 correspond to the modes (i) and (ii) in panel (a).

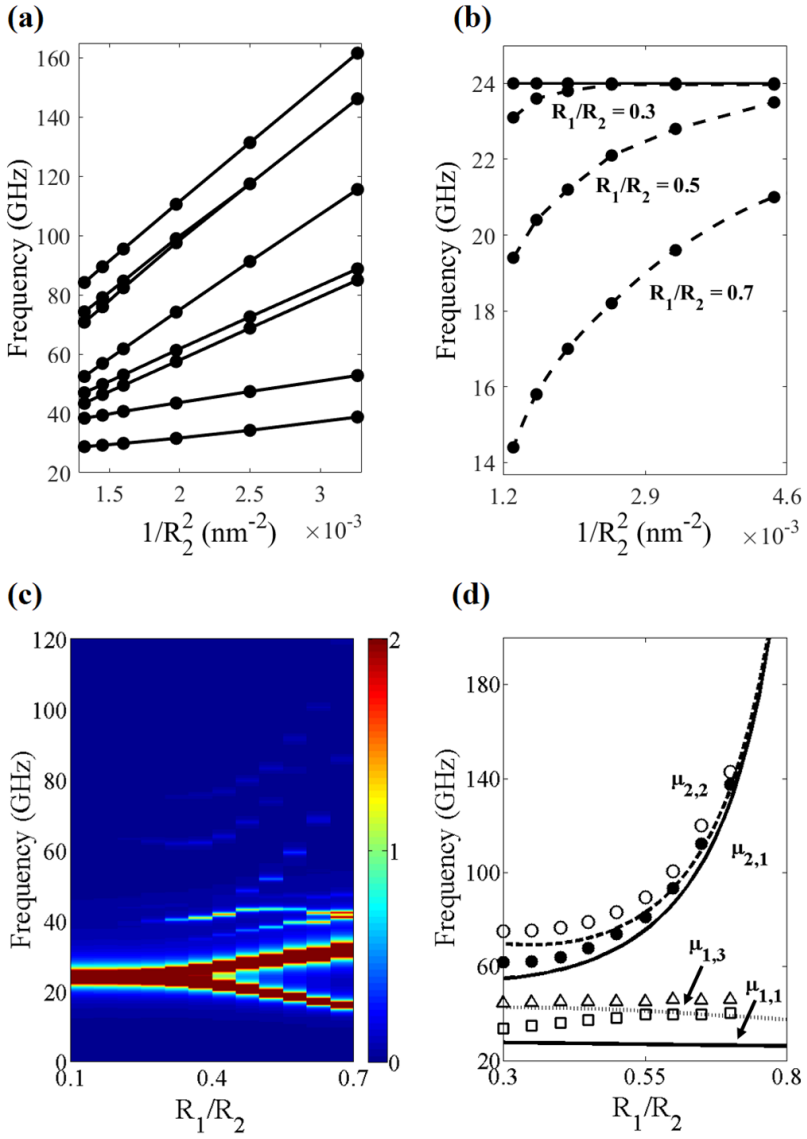

Figure 6.3: (a) The frequency of the numerically simulated resonance modes above the ferromagnetic resonance in Fig. 1(c) plotted against $1/R_2^2$ for $R_1/R_2 = 0.5$. (b) The size dependence of the ferromagnetic resonance for the solid sphere (black line) and the spherical shell with different values of the shell thickness (dashed lines). (c) The imaginary component of the numerically simulated susceptibility plotted against the ratio R_1/R_2. (d) The numerically simulated modes shown in Fig. 1(c) (symbols) plotted alongside the exchange modes calculated from equation (6.2) (lines) with varying shell thickness. The squares and triangles correspond to the numerically calculated modes $\mu_{1,1}$ and $\mu_{1,3}$, respectively.

mode with the ferromagnetic resonance can be broken when the boundary conditions are modified to include other effects, such as surface anisotropy [81]. Under this condition, the eigenvalue is no longer equal to zero and it should start to exhibit a $1/R_2^2$ dependence on the particle radius (this dependence can be observed for the lowest mode in Figure 6.3(a)).

Several of the modes above the ferromagnetic resonance do not show a strong dependence on the inner radius R_1. This behaviour is in agreement with the $k = 1, n \geq 1$ eigenvalues which are broadly independent of the shell thickness, but undergo a marginal decrease in frequency for larger values of R_1/R_2. However, in the numerical simulations the modes show a marginal increase in frequency with increasing R_1/R_2, before under-going a small decrease in frequency or stagnating. This suggests that the $k = 1, n \geq 1$ eigenvalues are also sensitive to the spatial variations of the magnetisation, and that this effect is in competition with the eigenvalue equation which acts to decrease the frequency.

The resonance modes found at higher frequencies exhibit a different kind of behaviour. These modes are roughly independent of the inner radius for $R_1/R_2 = 0.1 - 0.3$ but increase rapidly for $R_1/R_2 > 0.4$, and reach frequencies above 100 GHz for $R_1/R_2 = 0.7$. This is in good agreement with the analytical theory where the higher-order eigenvalues $k = 2$ vary only slightly for $R_1/R_2 = 0.1 - 0.3$, but increase rapidly for larger R_1/R_2. The fit of the theoretical model to the numerical simulations is shown in Figure 6.3(d).

6.3 Vortex domain

To explore ground state dynamics relaxation simulations were performed in the absence of an external DC field. The simulations consistently converged to the stable vortex domain configuration shown in Figure 6.4(a). The corresponding dynamic magnetic susceptibility is shown in Figure 6.4(b) for shells relaxed into the vortex

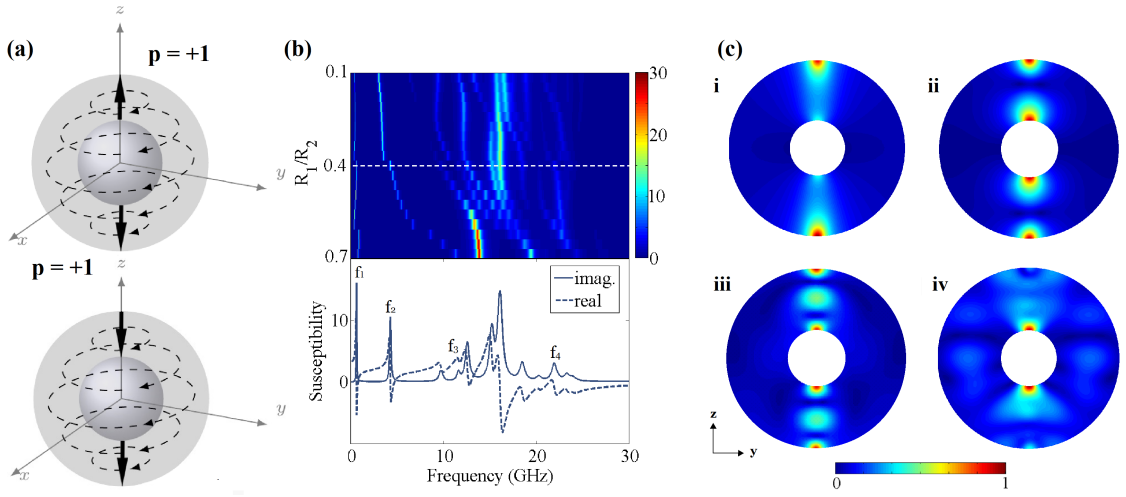

Figure 6.4: Vortex domain structure for spherical shell particles with parallel and anti-parallel orientation of the vortex singularities. (b, top) The imaginary component of the susceptibility (color) for a spherical shell of outer radius 100 nm and varying shell thickness. The white dashed line corresponds to the plot of the susceptibility (b, bottom). (c) normalised spatial Fourier transform corresponding to the y-component of the magnetisation for a shell of outer radius 100 nm and ratio $R_1/R_2 = 0.3$. The modes (i)-(iv) correspond to $f_1 - f_4$ in (b, bottom), respectively.

domain. The frequency f_1 in Figure 6.4(b) (bottom) corresponds to the uniform mode. The higher frequency modes f_2, f_3 and f_4 Figure 6.4, which have comparable magnitude to the fundamental mode, are higher-order flexural resonances [9]. These modes resemble standing modes across the vortex core line. In Figure 6.4(c), the spatial Fourier transform of the resonance flexural modes of the vortex domain are shown for different frequencies. Here, the higher-order flexural modes are pronounced across the entire $10 - 25$ GHz frequency band.

The influence of varying the shell thickness on the dynamic susceptibility is shown in the upper-part of Figure 6.4(b). The lowest frequency mode is the $n = 0(f_1)$ mode, for which the frequency does not vary significantly as a function of the shell thickness. This mode possesses the largest amplitude in the susceptibility spectrum for $R_1/R_2 \geq 0.4$. However, in contrast to the saturated solid sphere for which the ferromagnetic resonance has the largest amplitude for any particle size, the $n = 0$ flexural mode is not necessarily the most intense mode for solid spheres. In circular

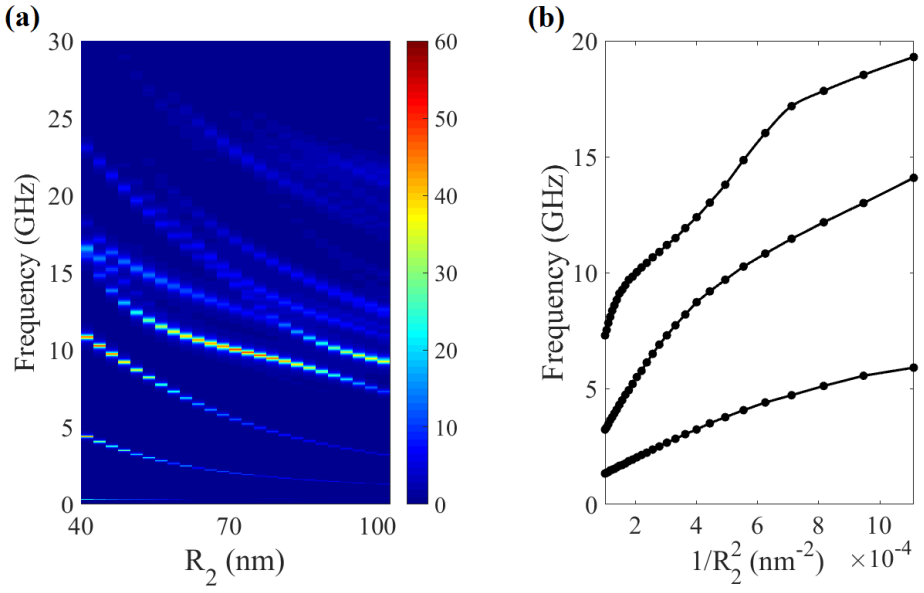

Figure 6.5: The frequency of the resonance modes plotted against R_2 for a solid sphere. The colorbar represents the amplitude of the imaginary component of the dynamic susceptibility (b) The first three modes above the fundamental mode plotted against $1/R_2^2$.

dots, the $n = 1(f_2)$ mode increases in amplitude with increasing thickness, and can obtain amplitudes greater than the $n = 0$ mode for sufficiently thick elements [9]. A similar scenario can be observed in Figure 6.4(b) as the $n = 1$ mode increases in amplitude with decreasing shell thickness, surpassing the amplitude of the $n = 0$ mode for $R_1/R_2 < 0.4$. This fact provides explanation of the measured permeability spectra of monodisperse nanospheres, where the lowest frequency mode can be significantly smaller than the higher-order absorption modes [19, 3].

The size dependence of the resonance modes is shown in Figure 6.5. The frequency of the higher-order modes depends strongly on the radius, whereas the lowest frequency mode is weakly dependent on the particle size. The size dependence is complicated by anti-crossing of the modes at different particle sizes R_2. The modes which closely approximate the $1/R_2^2$ dependence also show deviations from this trend with decreasing particle size. An analytical expression for the vortex flexural modes can be derived from the Thiele form of the Landau-Lifshitz-Gilbert equation without

damping [9]. The eigenfrequencies ω_n along the thickness of the vortex core for the case of a planar film are given by

$$\frac{\omega_n(L)}{\omega_M} \approx \frac{\pi}{8}\left(\frac{L_e}{L}\right)^2\left(\ln\left(\frac{R}{R_c}\right)+\frac{5}{4}\right)n^2 \tag{6.5}$$

where L is the thickness, $L_e = \sqrt{2A}/M_s$, $\omega_M = \mu_0\gamma 4\pi M_s$, R is the radius, $n = 0, 1, 2...$ and $R_c(L) \approx 0.68L_e(L/L_e)^{1/3}$. It can be seen from this equation that the flexural modes depend on both the thickness as $1/L^2$ and the outer radius, with the dependence on the radius being logarithmically weak. For the case of a spherical particle with the thickness taken across the vortex core line, this can lead to more complex size dependences as decreasing the radius would amount to varying L and R simultaneously.

The particles become single domain for $R_2 \approx 20$ nm in the numerical simulations, at which point the higher-order modes are destroyed and one pronounced peak corresponding to the ferromagnetic resonance of the saturated particle remains. The frequency of the ferromagnetic resonance is commonly used to estimate intrinsic magnetic parameters, such as the magnetocrystalline anisotropy constant [3] and particle sphericity [106]. In Figure 6.5, the frequency of the uniform mode in the vortex state is in the range of hundreds of MHz, whereas the ferromagnetic resonance of the saturated particle has a higher frequency of 1.5 GHz in the absence of an external DC field. Only the latter mode is well-described by Kittel's equation for the ferromagnetic resonance, which depends primarily on the magnetocrystalline anisotropy in the absence of an external DC field [107]. Experimental studies of mono-disperse particles have found that the multi-resonance behavior vanishes for a critical size below 50 nm [20]. For this particle size, only a single peak was observed in the permeability spectrum corresponding to the ferromagnetic resonance, which was shifted upwards in frequency when compared to the larger particles. The susceptibility of the higher-order modes is larger than the fundamental mode when the radius is in the range

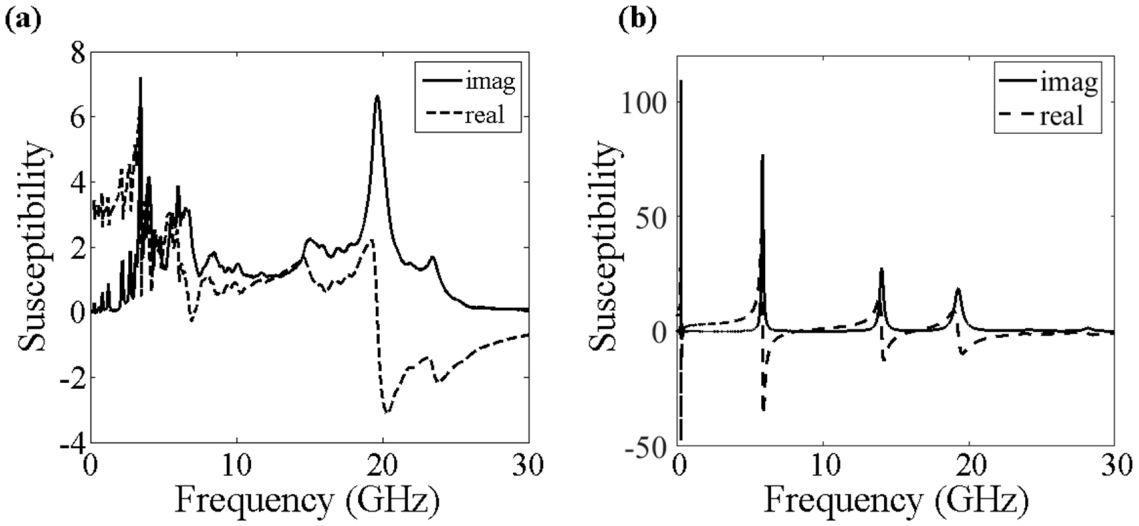

Figure 6.6: Resonances in the nano- and sub-micrometer regimes; Real and imaginary components of the susceptibility corresponding to the y-component of the magnetisation for (a) hollow sphere with $2R_2 = 750$ nm, $R_1/R_2 = 0.3$ and parallel orientation of the singularities, (b) solid sphere with $2R_2 = 60$ nm.

$50 - 100$ nm. However, the uniform mode steadily grows with decreasing particle size and becomes the largest mode for the smaller particles. In the numerical simulations, the fundamental mode of the solid sphere dominates over the higher-order modes when the radius reaches $R_2 \approx 30$ nm. However, it can dominant at significantly larger particle sizes for thin shells. As the particle size is increased into the sub-micrometer regime, the amplitude of the resonances is decreased and the bandwidth is wider. However, pronounced resonance modes remain in the 15-25 GHz region for sub-micrometer sized particles, with a negative real component of the susceptibility. These high-frequency modes are persistent at frequencies of 15-25 GHz as the particle size is increased further, because the exchange interaction is not dominant in this size range. Observations of resonance modes in this frequency range were recently found for carbonyl iron particles [108].

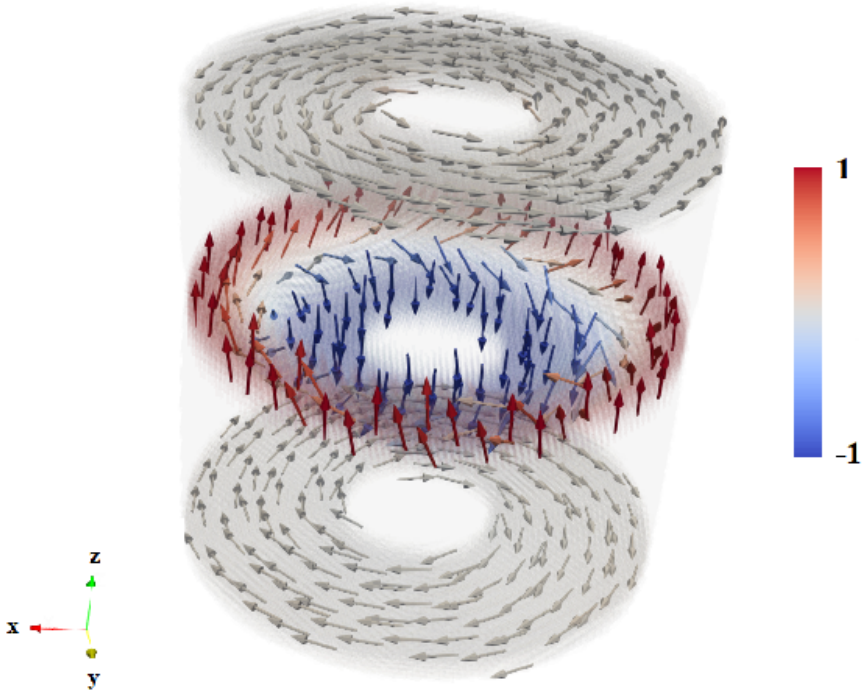

Figure 6.7: Static magnetisation configuration for a cylindrical nanotube of outer radius $R_2 = 250$ nm, ratio $R_1/R_2 = 0.3$ and length $L = 500$ nm. Colorbar represents the normalised z-component of the magnetisation.

6.4 Chiral domain

For thick and soft magnetic nanotubes, the equilibrium magnetisation configuration exhibits two vortices at the end domains with antiparallel chirality [109]. During magnetisation reversal, these two non-uniform vortex configurations grow in size leading to the gradual annihilation of the uniformly magnetized central region, and the formation of either transverse or vortex-like domain walls inside the nanotube. Such reversal modes are a consequence of the curved surface and do not exist in "unrolled" nanotubes, i.e. magnetic strips. The existence of opposite chirality vortices at the end domains of nanotubes during magnetisation reversal has been confirmed experimentally [110, 111]. This chiral effect can be understood by examining the exchange energy density for an arbitrary magnetic shell. When the magnetostatic energy is approximated by a suitable easy-tangential anisotropy, Gaididei et al. [14] showed

that the magnetic energy can be divided into three components (i) the "standard" exchange interaction; (ii) an effective anisotropy and (iii) an effective DMI-like interaction [3]. The first term (i) is minimized when the magnetisation is homogenous, whereas the effective DMI term (iii) favours the formation of inhomogeneous magnetisation configurations. The stabilization of the opposite chirality vortices in Figure 6.7 results from the competition between the three terms (i)-(iii).

For a curved surface parametrized by the coordinates (q_1, q_2), the magnetisation can be written in the form [112]

$$\mathbf{m} = \hat{n}\cos\Theta + \hat{q_1}\sin\Theta\cos\Phi + \hat{q_2}\sin\Theta\sin\Phi \tag{6.6}$$

where $\Theta = \Theta(q_1, q_2)$ and $\Phi = \Phi(q_1, q_2)$ represent the angles of the magnetisation in a curvilinear background and $\hat{n} = \hat{q_1} \times \hat{q_2}$. The exchange energy density for an arbitrary curved magnetic shell can then be written

$$\frac{E_{ex}}{A} = \left(\sin\Theta(\nabla\Phi - \Omega) - \cos\Theta\frac{\partial\Gamma(\Phi)}{\partial\Phi}\right)^2 + \left(\nabla\Theta - \Gamma(\Phi)\right)^2 \tag{6.7}$$

where A is the exchange stiffness constant, $\Gamma(\Phi)$ is a matrix depending on the Gauss and mean curvatures of the nanomagnet and Ω is a modified spin connection. If the magnetic field is pointing along the z-axis with parametrization $(\hat{n} = \hat{z}, \hat{q_1} = \hat{\rho}, \hat{q_2} = \hat{\phi})$, the modified spin connection is given by

$$\Omega(\theta) = -\hat{\phi}/\rho \tag{6.8}$$

and, as a result, a chiral effect must take place according to this parametrization. Here, the chiral interaction produces the opposite chirality vortices shown in Figure 6.7 when the DC-field is applied along the z-direction during the hysteresis cycle.

Multi-domain structures have been found to play an important role in broadening microwave absorption in composite materials [113] and may be an interesting

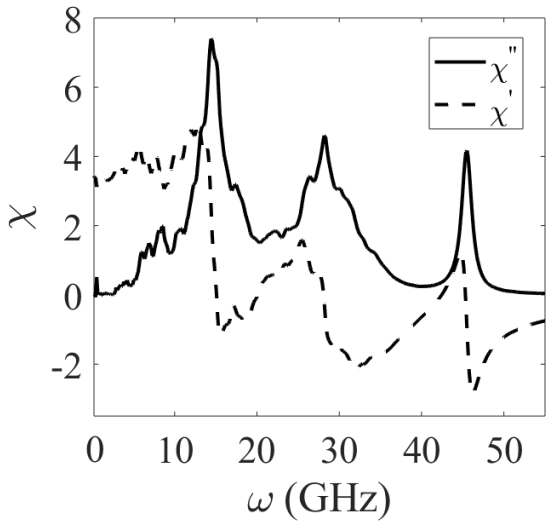

Figure 6.8: Dynamic susceptibility of the y component of the magnetisation where $R_2 = 250$ nm, $R_1/R_2 = 0.3$ and $L = 500$.

way to enhance the permeability at microwave frequencies. In this way the magnetic properties of the material can be treated as the free parameter, when the geometric parameters are limited by technological constraints. To study their role in microwave absorption, micromagnetic simulations of FeCo nanotubes supporting chiral magnetisation textures were carried out for the values $\alpha = 0.01$, $M_s = 1.9 \times 10^6$ A/m, $A = 1.7 \times 10^{-11}$ J/m and negligible magnetocrystalline anisotropy [114].

The complex dynamic susceptibility spectra of a cylindrical shell with outer radius $R_2 = 250$ nm and length $L = 500$ nm supporting a chiral domain state is reported in Figure 6.7. The resonance spectra can be broadly categorized into three frequency bands (i) a low frequency region spanning approximately $10 - 20$ GHz, (ii) a mid-frequency region spanning $25 - 35$ GHz and (iii) a high-frequency peak located at 45 GHz. A notable feature of the observed spectra is that the resonances are smeared out across a very wide frequency band, which is a particularly desirable characteristic for devices requiring broadband resonators [2].

The full three-dimensional maps of the spatial susceptibility are represented in Figure 6.9 as isosurfaces. For the purpose of visualising the mode symmetry, the

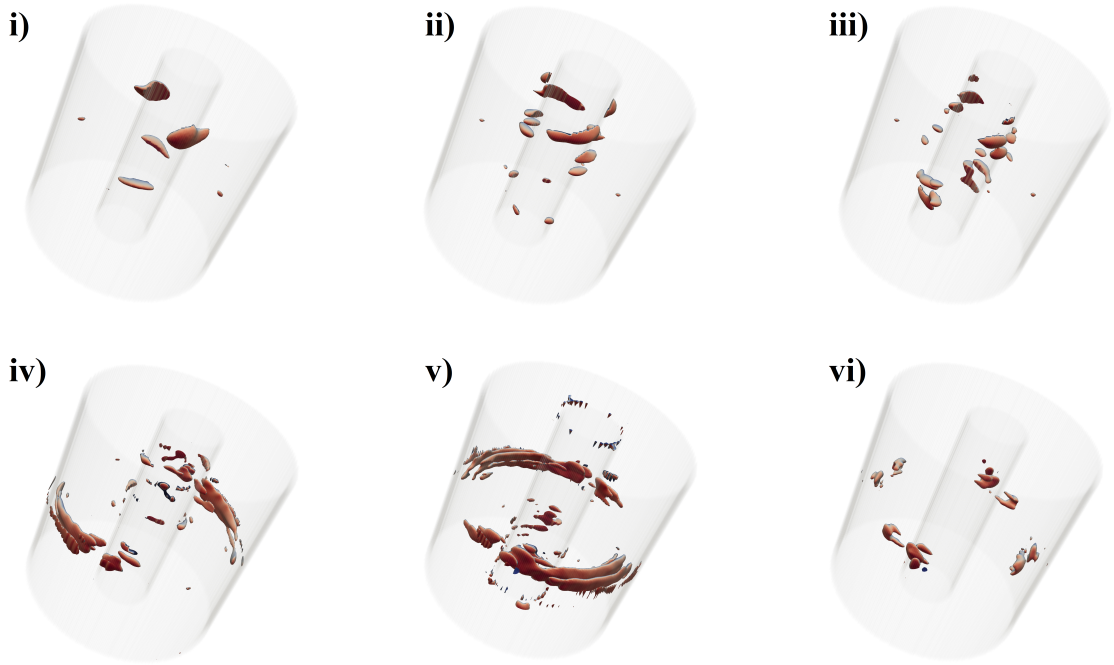

Figure 6.9: Isosurface of the normalised Fourier transform of $M = M_x + M_y$ where $R_2 = 250$ nm, $R_1/R_2 = 0.3$ and $L = 500$ nm. The frequencies correspond to Figure 6.8(a) and are given by (i) 7.7 GHz, (ii), 13.7 GHz (iii) 14.7 GHz, (iv) 28.1 GHz (v), 32.2 GHz and (vi) 45 GHz

normalised Fourier transform of both the x and y magnetisation components are considered, i.e. $M = M_x + M_y$. The spatial distribution of the dynamic susceptibility inside the nanotube exhibits three strongly non-uniform behaviours corresponding to the three spectral regions observed in Figure 6.8. In the low frequency region represented by Figure 6.9(a)-(c) the magnetisation spirals around the internal neck of the cylinder with increasing complexity as the frequency increases. In the mid spectral region shown in Figure 6.9(d)-(e), the resonances are localised at both the inner and outer surface, with the largest excitation occurring close to the particle surface. Finally, the highest frequency mode in Figure 6.9(f) is localised within the central domain region shown in Figure 6.7 with negligible contribution from the upper and lower end domains. A possible route to maximise volume efficiency and increase the susceptibility response of the particle is to minimize the upper and lower end domains, and maximise the central domain region shown in Figure 6.7.

6.5 Summary

The dynamic susceptibility of ferromagnetic spherical shells was investigated as a function of shell size and thickness. The frequency of the higher order modes for saturated nanoshells was found to scale as $1/R_2^2$ in agreement with the exchange approximation. Moreover, it was found that the zeroth exchange mode is not degenerate with the ferromagnetic resonance for a shell, even in the absence of surface anisotropy. Nanoparticles with vortex domain structure and radius $R_2 \leq 100$ nm exhibited a number of narrow, intensive resonance bands ranging in frequency from several hundred megahertz to tens of gigahertz. The amplitude and frequency of these modes showed a strong dependence on shell thickness and size, making ferromagnetic nanoshells promising candidates for use as tuneable microwave absorbers. When the radius was increased to several hundred nanometers, the particles exhibited broad resonance peaks with significantly reduced susceptibility when compared to smaller

nanoparticles. In all cases, the dynamic magnetic response of the vortex domain was primarily due to small regions concentrated at the particle surfaces, such that only a small percentage of the particle volume contributes significantly to the susceptibility. Finally, chiral magnetisation configurations in cylindrical nanotubes were found to exhibit a broad and strongly non-uniform susceptibility spectra in the absence of an external bias field, with frequencies extending beyond that of the spherical vortex domain.

Chapter 7

Three-dimensional domain wall dynamics in permalloy films

7.1 Introduction

The magnetic properties of thin-film elements have been the subject of intense research interest in recent years. In addition to their potential applications in high-density magnetic storage [115] and magnetic vortex generation [116, 117, 118], these magnetic elements are model systems for studying the fundamental spin dynamics in patterned geometries with well-defined static magnetisation configurations [119, 120, 121, 122]. It has been shown that the ground state configuration of ferromagnetic nano-objects depends on the intrinsic material parameters such as the saturation magnetisation and exchange constant, in addition to the geometrical parameters of the element [112, 123, 124, 125]. The interplay between the geometry and intrinsic magnetic parameters leads to a wide range of magnetic states, such as those described previously in Chapter 6. In terms of their dynamic properties, it has been shown that the vortex state supports a translational gyrotropic mode in thin films [116, 118], in addition to higher-order spin wave modes at gigahertz frequencies [126, 127]. The low-frequency translation mode acts as a coherent oscillator and has attracted con-

siderable attention for microwave applications [128, 129, 130]

The main purpose of this chapter is to investigate numerically the static and dynamic properties of relatively thick ($\approx$ 80 nm) square elements in the presence of non-uniform field excitations, and to compare with experimental results. This chapter also serves as a precursor to Chapter 8 where the skin effect and non-uniformity of the excitation field is incorporated rigorously through solution of Maxwell's equations. The details of the experimental technique are beyond the scope of this thesis and can be found in the relevant publication [25]. Here, it is shown by means of numerical micromagnetic simulation that the domain walls support a perpendicular out-of-plane component that can switch dynamically in response to specific pulse parameters. This is achieved by the formation of bullet-like excitations which propagate along the domain walls towards the corners of the square element. The numerical simulations further reveal that four singularities are present at the corners of the square element, resulting from the three-dimensional character of the static magnetisation configuration. The polarity of these singularities can be switched in response to specific magnetic pulse parameters. In the final section of this chapter, the role of an external bias field on the static behaviour is investigated.

7.2 Static magnetisation

In these simulations standard parameters for permalloy (saturation magnetisation $M_s = 8 \times 10^5$ A/m, exchange constant $A = 1 \times 10^{-11}$ J /m and Gilbert damping = 0.008) were chosen with cell-size $x = 2000/512$ nm, $y = 2000/512$ nm, $z = 83/16$ nm and negligible magnetocrystalline anisotropy. Vortex precession was induced by a step pulse with maximum amplitude(s) of 7.7 mT and 10 mT and rise-time $\approx$ 1 ns. The field profile decays as $1/(r_0 + r)$ through the thickness of the square element with $r_0 = 40$ nm representing the half thickness of the antenna. The dot product of the vector magnetisation was calculated with respect to the x-ray vector and the

magnetisation was averaged across the thickness at the corresponding angle.

To provide a realistic comparison with the experimental results, the projection of the magnetisation at 45° (135°) degrees was calculated from the dot product of the magnetisation with respect to the x-ray vector. The intensity is at a maximum when the magnetisation vector points at a 45° (135°) degree angle to the x-ray, leading to the greatest intensity slightly above (or below) the vortex core. Figure 7.1 shows the simulated magnetisation contrast for different layers of the sample. The vortex spin arrangement varies continuously from negative values (red color) to positive ones (blue color) about the vortex axis. Non-uniformity can be observed across the thickness of the element with different spiral structures present at the top and bottom layers. This type of domain deformation was previously reported in thick circular dots [8, 131]. It results from the dipole-dipole interaction and the reduction of surface magnetic charges at the end domains. The vortex core radius also varies with the film thickness, with the smallest radius observed at the top and bottom layers of the sample. The simulated magnetic contrast is shown in Figure 7.1 (a) and Figure 7.1 (b) when the magnetisation is averaged linearly across the thickness and when the averaging is performed at 45°. When the averaging is performed linearly the middle region is predominant in the simulated x-ray projection (see Figure 7.1). When the averaging is performed at 45° a projection of core deformation is present in the simulated image. The precise angle of inclination, either 45° or 135°, determines whether the top or bottom layers become dominant in the simulated projection.

7.3 Core gyration

In Figure 7.2, the core gyration motion is shown when the sample was excited by a step pulse of rise-time $\approx$ 1 ns, which provides sufficient bandwidth for excitation of the vortex core. In the numerical simulations, Gaussian smoothing was applied to the excitation pulse to reflect the realistic capacity of the pulse generator and

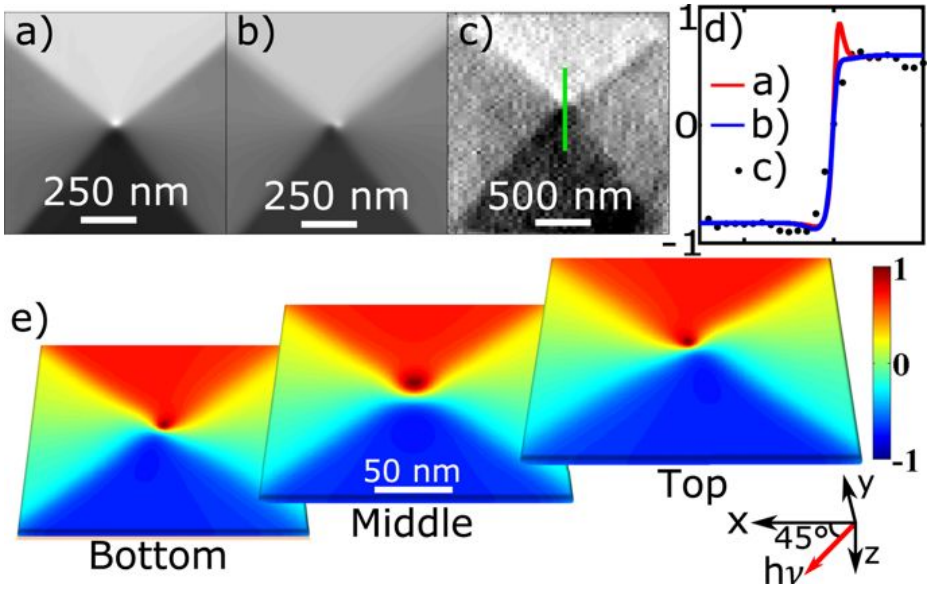

Figure 7.1: Simulated normalised magnetic contrast with averaging out the thickness in (a) perpendicular orientation and (b) over 45° direction. (c) Reconstructed experimental image obtained for the same delay time. (d) Vertical intensity profiles through the centre of the core for all three images a, b and c. Positive values correspond to magnetisation vector parallel to the x-ray wave vector. (e) Simulated images of the magnetic contrast for different layers within the structure. From left to right, the images represent the bottom 1st, middle 8th and top 16th layer of a 16-cell thick simulation grid (cell size is $3.9 \times 3.9 \times 5$ nm^3). Colour coding: Positive (Red) and negative (Blue) normalised magnetic contrast.
Reproduced from [25].

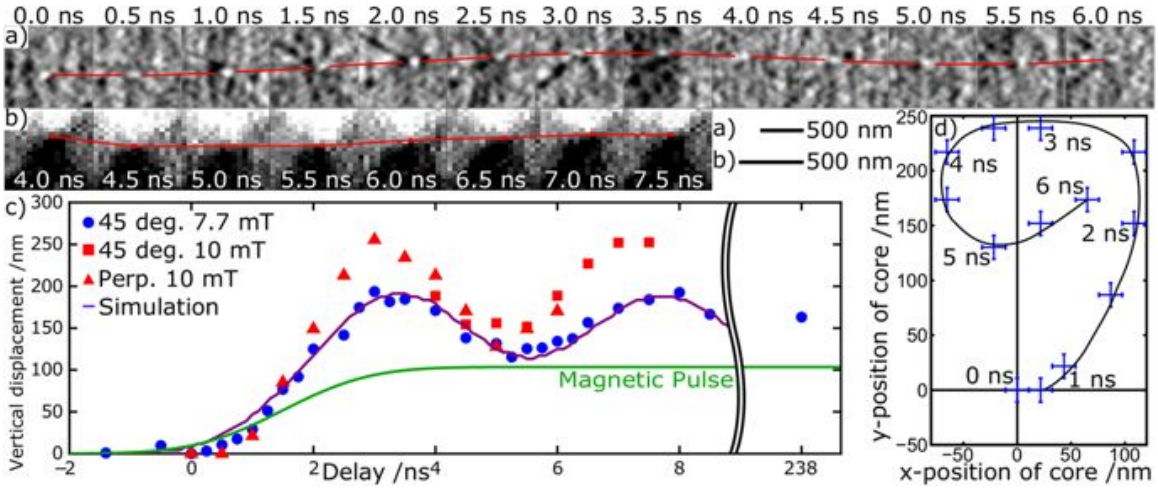

Figure 7.2: Close-up of the reconstructed magnetic contrast around the core taken at different values of the delay time dt for (a) 90° and (b) for 45° (3.7 V pulse) angle-of-incidence. The lines trace the vortex core position. (c) The vertical displacement of the vortex core at different delay times. The purple line shows vertical displacement extracted from micromagnetic simulations. The simulated magnetic pulse profile is shown by the green line. The point at 238 ns delay gives the vertical position of the core after being fully damped. The pulse length for this particular point was increased to 500 ns to allow verifying the vertical position of the core in this case. (d) The position of the vortex core in the xy plane at various delay times imaged in perpendicular orientation.
Reproduced from [25].

transmission lines, which leads to an overall reduction of the core gyration radius. A non-uniform field was also chosen which decays across the thickness of the element according to the relation $B = B_0 r/(r_0 + r)$, where $B_0 = 7.7$ mT is the field at the antenna surface and r_0 represents the half-thickness of the antenna. This non-uniform field gradient is similar to the skin effect described in Chapter 3.

In the initial stages of the gyration, the vortex core is displaced vertically (along the y-axis) and begins to precess about a new equilibrium position. The degree of the displacement is determined by the maximum amplitude A_0 of the applied step pulse. At the new equilibrium position this displacement is equal to that induced by an external DC field of amplitude A_0. It can be seen from Figure 7.2 that close agreement is achieved between numerical and experimental results (gyration frequency ≈ 4.5 ns) when using a standard value of the damping constant for permalloy $\alpha = 0.008$.

In Figure 7.3 the angle of imaging is orientated at 90° to the in-plane sample. In the numerical simulations this means that only the z-component of the magnetisation is present in the simulated projection and the magnetisation is averaged linearly across the thickness of the element. The simulated and experimental projection is shown for different time intervals during the cyclic gyration of the vortex core. In addition to the central core, four domain wall lines are visible in both the simulated and experimental images. These domain walls are present throughout the dynamic precession of the core, indicating that they are a result of the static magnetisation configuration. In the numerical simulations, before the pulse is applied, the static magnetisation shows four domain walls with small out-of-plane magnetisation components which possess the same polarisation as the vortex core. When the step-pulse is applied, the polarity of the domain walls are switched gradually as bullet-like excitations propagate from the core towards the corners of the element. The precise pulse threshold required to switch the corner singularities and domain wall polarity is sensitive to the field gradient, Gaussian smoothing and rise-time of the pulse excitation.

When comparing the simulated and numerical projection of the out-of-plane mag-

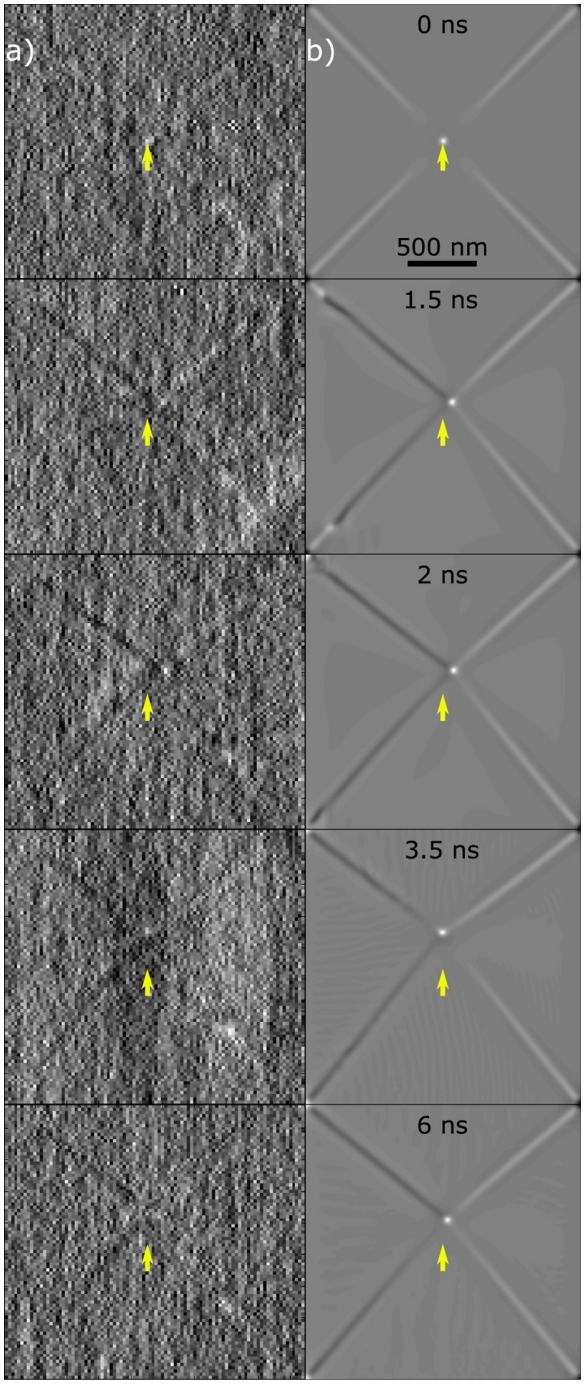

Figure 7.3: (a) Experimental and (b) simulated magnetic contrast of the domain structure imaged in perpendicular orientation at different delay times (from top to bottom): $0.0, 1.5, 2.0, 3.5$ and 6.0 ns. The frames represent different stages of the pulse rise and gyration. The domain walls at the left-hand side in each image are predominantly 'black' (magnetised downwards), whereas those at the right-hand side are always 'white' (magnetised upwards). Yellow arrows have been inserted to point to the equilibrium position of the core.
Reproduced from [25].

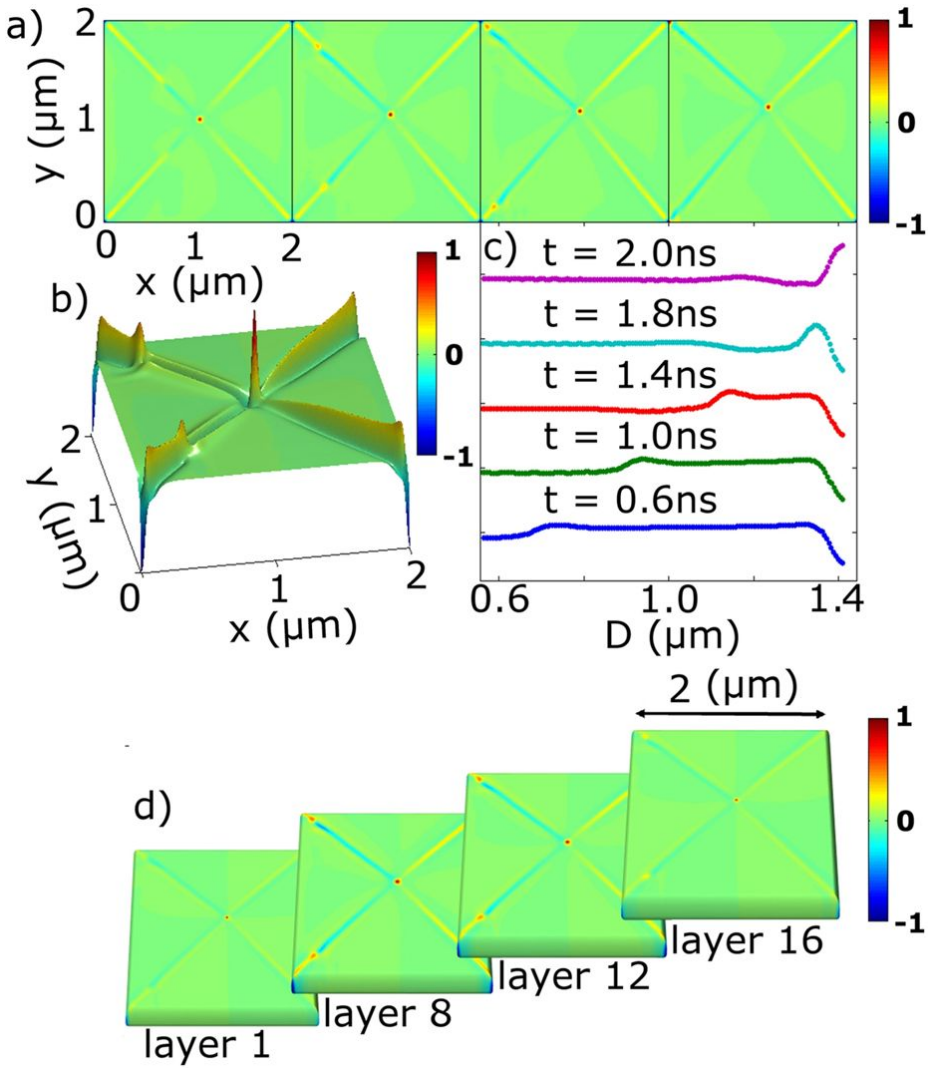

Figure 7.4: (a) Perpendicular component of the magnetisation at different delay times $t_0 = 0.3, 1.3, 1.8$ and 2.3 ns. (b) 3D depiction of the out-of-plane magnetic component at 1.4 ns delay. A localised wave 'bullet' is formed at the edge of the positively polarised part of the domain wall and propagates within the wall towards the corner. (c) Intensity scans within the domain wall for different delay times demonstrating the profile of the 'bullet' as it approaches the singularity at the corner. (d) The simulated structure of the domain walls for different layers throughout the thickness of the element. The wave 'bullet' structure is more pronounced in the middle layers. Reproduced from [25].

netisation component, it is readily seen that the intensity of the corner singularities appear more intense in the numerical simulations. A plausible explanation is lithographic imperfections in the experimental sample, resulting in more rounded edges and broadening of the corner singularities. Figure 7.4(d) also shows that these domain wall features vary as a function of the thickness in a similar manner to the vortex core, with the effect being suppressed towards the top and bottom of the square element. According to numerical simulations, the direction of propagation of the bullets also depends strongly on the field gradient. The bullets propagate either along the left or right domain wall lines depending on whether the amplitude of the field is larger at the top or bottom layers of the element. When the field is uniform the bullets are reflected off the corner boundaries (see supplementary information in reference [25]).

7.4 External bias field

In this section the role of an external bias field on the static and dynamic behaviour of thick elements (≈ 80 nm) is examined. The square elements were relaxed into their ground state configurations and a 30 Oe bias field was applied in the xz-plane. For the thinner elements, the domain region in the direction of the DC field increases and the vortex core gradually moves up towards the boundary of the element. The core is then annihilated and the vortex state switches to a saturated domain configuration. This behaviour is well-understood and has been documented extensively in the literature [132, 133, 134]. For the thicker elements, several distinct features emerge as the amplitude of the static field is increased. First, at a field value of magnitude ≈ 20 mT the needle-like core region is stretched across a wider area, forming an extended boundary between the upper and lower Landau domains (see Figure 7.5). Pronounced out-of-plane components are also present across the domain wall lines with different polarities in the upper and lower sections of the element. In Figure 7.5(a), the out-of-plane (z-component) of the magnetisation is shown for two $2\mu m$ squares with

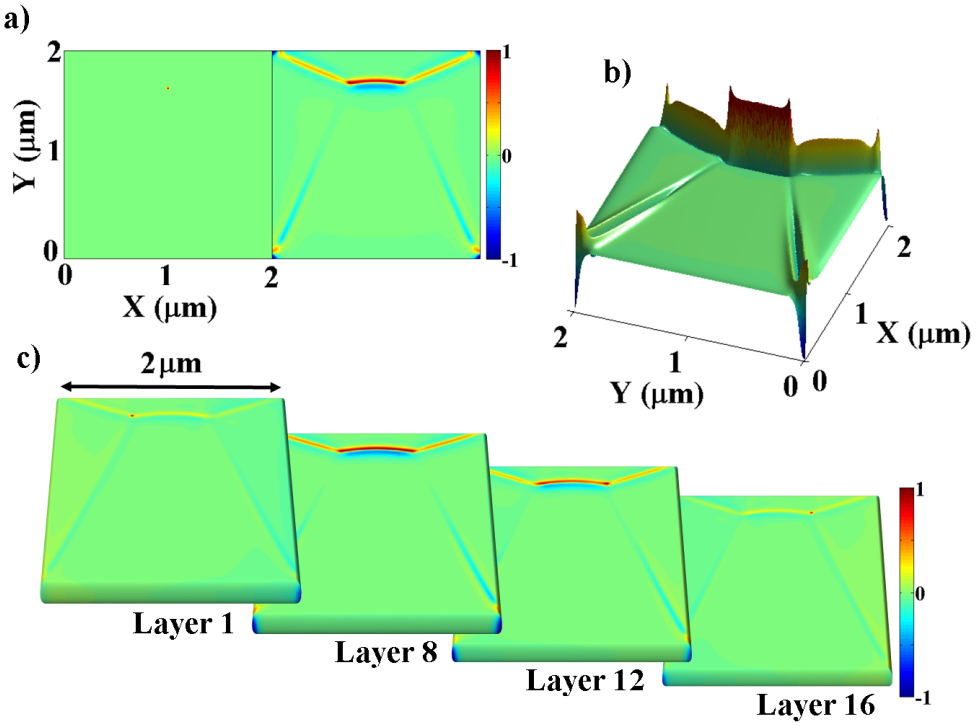

Figure 7.5: (a) Perpendicular component of the magnetisation for a square element of thickness 20 (left) and 80 nm (right) taken at the cross-section. (b) 3D depiction of the out-of-plane magnetisation component at the static equilibrium position. (c) The simulated structure of the domain walls for different layers throughout the thickness of the element. The out-of-plane components are more pronounced in the middle layers.

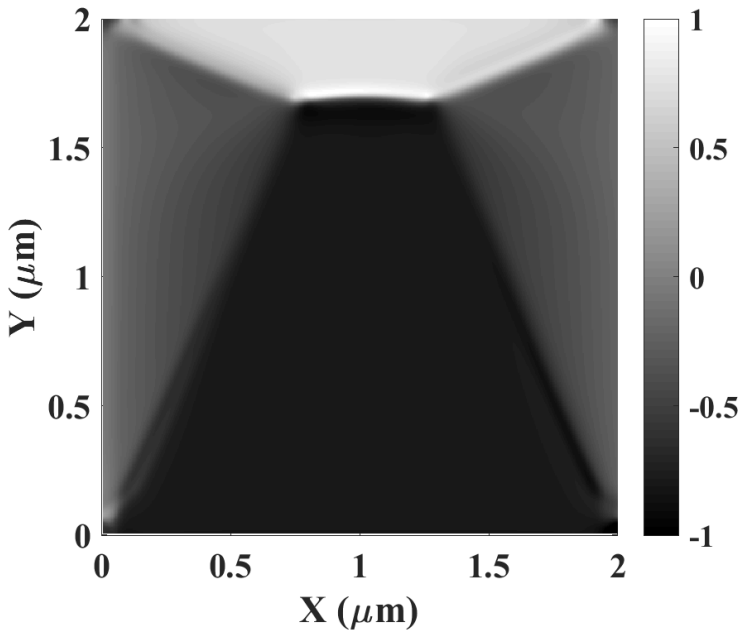

Figure 7.6: Simulated projection for the static magnetisation configuration when the x-ray vector is at an angle of 45° to the in-plane sample and the magnetisation is averaged across the thickness at the corresponding angle.

thickness 20 nm and 80 nm, respectively. For the 20 nm sample, only a small out-of-plane component is present corresponding to the vortex core. For the 80 nm sample, significant out-of-plane components can be found across the four domain walls, in addition to an extended domain wall-like region which has replaced the vortex core. These domain features also vary in a pronounced manner across the thickness of the element (see Figure 7.5(c)). For the bottom layer, the out-of-plane component reaches its maximum intensity towards the left-most extreme of the extended Landau structure, whereas the top layer has a maximum intensity towards the right-most side. Towards the middle layers the out-of-plane component has similar magnitude across the entire central line. In Figure 7.6 the simulated projection is shown for an x-ray vector of 45° when the magnetisation is averaged across the thickness at the corresponding angle. Here, it can be seen that the middle layers are the dominant layers in the projection of the domain structure, with two lines (a peak and dip) clearly visible across the extended Landau structure.

7.5 Summary

In this chapter, the eigenfrequency of the uniform gyrotropic mode was investigated by means of micromagnetic simulation and compared with experimental results. Excellent agreement was found when using standard values of permalloy with damping constant $\alpha = 0.008$. It was shown that the 3D character of the domain and core structure have a direct influence on the domain walls. The out-of-plane component of the domain walls can change polarity following excitation of the vortex core by application of a magnetic pulse. The change in polarisation is achieved by the generation of "bullet-like" excitations, which propagate along the domain wall line towards the corner of the element. The propagating bullet can then flip the polarity of the corner-singularity or reflect off the boundary depending on the specific field gradient and amplitude specified in the numerical simulation. The presence of a static DC field was found to play an important role in the static properties of thick (≈ 80 nm) elements. For a DC field value of magnitude ≈ 20 mT the needle-like core region is stretched across a wider area, forming an extended boundary between the upper and lower Landau domains. Pronounced out-of-plane components were also present across the domain wall lines.

Chapter 8

Wave propagation in metallic structures

8.1 Introduction

There are two main and different approaches for modelling the interaction of magnetic and electromagnetic fields with magnetic materials and the reciprocal reaction of the magnetic material. The first approach focuses on the magnetic energies of the magnetic material, or micromagnetics, to evaluate the magnetisation distribution in response to external, pre-defined magnetic fields from solution of the dynamic Landau-Lifshitz-Gilbert equation (for example [35]). The magnetostatic fields internal and external to the material are then computed from the corresponding volume and surface magnetic charges. The transient Maxwell's equations are not solved in this case, and the consequences of conductive and dielectric material properties and surrounding layers, and of induced currents and charges on perturbing the applied and internal fields and consequently the material magnetisation are not considered. In the other approach, and more traditionally, a macroscopic (compared to the exchange and domain wall dimensions in micromagnetics) scalar or tensor permeability model is used to describe the linear or nonlinear behaviour of the magnetic material as part

of Maxwell's equations and their static and harmonic variants. The **B-H** or **M-H** hysteretic characteristics of the material used in the permeability formulation are modelled using analytical mathematical expressions based on linearised and static micromagnetic solutions or from fitting to experimental data [135].

For transient and harmonic electromagnetic simulations, a frequency-dependent, complex tensor permeability is defined within Maxwell's equations. The origins of this frequency dependent permeability is from linearised solutions of the dynamic Landau-Lifshitz-Gilbert (LLG) equation (damped or undamped), that describe small precessional perturbations of the magnetic moments around an averaged magnetisation direction. The resonance frequency or frequencies in this linearised description may be estimated from theoretical analysis of the effective internal and external fields, or supplied by complex permeability measurements. Thus this frequency dependent permeability provides only a description of the rotation of the magnetic moments due to small perturbing fields, and does not take into account local shape and magnetocrystalline anisotropies, nor exchange and surface energies responsible for the domain nucleation and spin-wave phenomena. As a result, the frequency dependent permeability approach often employed in electromagnetic simulations can not produce or model the spatial distribution of the magnetisation in magnetic materials and their reaction on the magnetic fields generated within and external to the magnetic material in response to impinging electromagnetic fields.

The finite-difference time-domain (FDTD) method, which is the focus of the theoretical analysis in this chapter, through its structure and implementation provides a flexible framework for the simulation of a wide range of electromagnetic phenomena, providing almost infinite bandwidth due to its time domain nature. Thus it offers a natural platform for dynamic and steady-state modelling of the interaction between electromagnetic waves with non-linear magnetic materials. Previous work incorporating the LLG equation within the FDTD method was limited to small signal approximations of the LLG equation [136], which did not include magnetocrystalline

anisotropy and exchange coupling, and used explicit time marching schemes that were either inappropriate or unstable for small damping [45, 137]. To account for the staggered nature of the FDTD grid, cumbersome and less accurate four-point spatial interpolations were used to collocate the magnetisation with the fields in each cell of the grid. The complete form of the LLG equation was included in a stable FDTD implementation in that accounts for anisotropy and exchange energies [42], but used a numerically dispersive unstaggered FDTD grid for the implementation which is not appropriate for studying dynamic wave interaction with magnetic material.

An efficient and stable implementation was developed by Aziz [43] that integrated the complete form of the LLG equation, including the anisotropy and exchange coupling fields, within the FDTD method. This implementation included the development of a new and efficient discretisation scheme locating the magnetisation vectors at the corners of the FDTD cell allowing simple two-point interpolations for the evaluation of the magnetisation at the staggered locations of the magnetic fields without any numerical dispersion. Moreover, the proposed implicit time marching/integration algorithm is stable and accounts for the correct implementation of magnetic boundary conditions and therefore provides consistency between the LLG and FDTD schemes. This stable algorithm was implemented in the literature to study the broadband ferromagnetic resonance of thin-film magnetic nanostructures closely contacting non-magnetic metallic layers in microstrip line structures [138], and as part of an Improved Concurrent Electromagnetic Particle-In-Cell (ICEPIC) code for High Power Microwave (HPM) devices for modelling the interaction of electromagnetic waves with ferrites [139].

Here, the FDTD-LLG method is extended to include plane-wave propagation through semi-infinite permalloy prisms with square cross-sectional areas of sides $250-1000$ nm. This is to investigate the dynamic magnetisation and permeability through the magnetic structures, and corresponding wave transmission and reflection illustrate the importance of the need to include the full micromagnetic details of the magnetic

material in the simulation. Wave propagation and dynamic permeability simulations are presented before closing this chapter in the summary section.

8.2 Plane wave excitation

In this section numerical simulations of conducting semi-infinite permalloy prisms are carried out to illustrate the effects of finite conductivity and electromagnetic wave propagation on the magnetic behaviour. The ferromagnetic sample has saturation magnetisation $M_s = 800$ kA/m, exchange constant A $= 1 \times 10^{-11}$ J/m, electrical conductivity $\sigma = 3.7{\times}10^{-6}(\Omega\text{m})^{-1}$, relative permittivity $\epsilon_r = 7$ and negligible uniaxial magnetocrystalline anisotropy ($K_u = 0$ J/m^3). The damping coefficient was set to $\alpha = 0.01$. The surrounding magnetic region has the relative permeability of free space, i.e. $\mu_r = 1$.

A DC field was applied in the positive z-direction of magnitude 200 Oe, in a direction parallel to the initial magnetisation. The initial condition for the magnetisation was set to $M_x = M_y = 0$ and $M_z = M_s$ which is a stable configuration at the beginning of the simulation. The strong shape anisotropy of the infinite pillar forces the magnetisation to align along the pillar axis, which is defined here as the z-axis. The magnetic precession will then occur primarily in the x-y plane and the z-component of the magnetisation can be expressed as

$$M_z = M_s + m(t) \tag{8.1}$$

where M_s is the saturation magnetisation and $m(t)$ is a small perturbation of the magnetisation in the time-domain. As a result the magnetisation remains stable and divergence free for all time, which ensures that Maxwell's equation is satisfied

$$\nabla \cdot (\mathbf{H} + \mathbf{M}) = 0 \tag{8.2}$$

Here, it should be emphasised that Maxwell's equation (8.2) is not imposed directly as in the case of micromagnetics, but it is satisfied for small excitations about suitably chosen input data.

The permalloy sample was excited with an electromagnetic plane wave of the form

$$E_z(t) = E_z(0)e^{-t^2/\tau^2} \tag{8.3}$$

where $E_z(t)$ is the time-domain profile of the electric field, $E_z(0)$ is the maximum amplitude of the pulse field, t is the simulation time and τ is given by

$$\tau = \frac{1}{\sqrt{2}\pi f dt} \tag{8.4}$$

where f is the frequency of the plane wave and dt is the time-step. Here, the frequency was chosen to be $f = 50$ GHz which provides sufficient bandwidth for the range of frequencies under investigation. The time-step is determined in this case from the equation $dt = dx/2c$, where dx is the cell-size which is set in the nanometer range $5 - 50$ nm depending on the pillar size under consideration. This is far below the wavelength of the propagating plane wave which is of the order of millimetres. In each case the simulation was run for 3 ns to allow for the transient fields to die out.

The plane wave is introduced at the lower interface of the TFSF boundary and removed at the top surface of the TFSF boundary. The one-dimensional plane wave was terminated using a second-order, one-direction wave equation analytical absorbing boundary condition, to sufficiently reduce the reflections from the auxillary plane-wave equation at time steps less than the Courant limit employed in the TMz calculations in this work. The simulation space, including the TFSF boundary, were terminated using a 10 cell perfectly matched layer (PML) to absorb outgoing waves and minimise reflections, implemented using Berenger's split-field formulation [140] with a third-order polynomial grading for the magnetic conductivity and 10^{-8} reflection error.

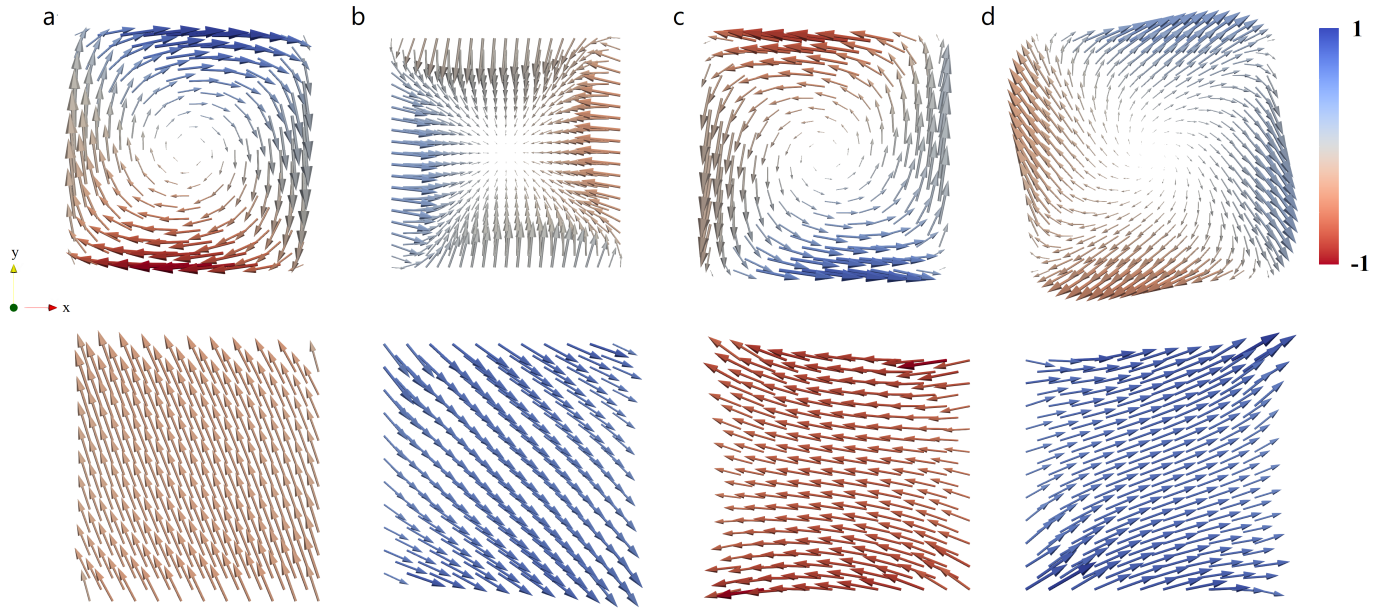

Figure 8.1: Temporal profile of the magnetisation at (a) 0.04 ns, (b) 0.06 ns, (c) 0.08 ns and (d) 0.1 ns for a semi-infinite permalloy prism of length 250 nm following excitation by an electromagnetic wave for conducting (top) and non-conducting (bottom) cases. Arrows represent the x-y component of the normalised magnetisation vector. The colorbar corresponds to the normalised x-component of the magnetisation.

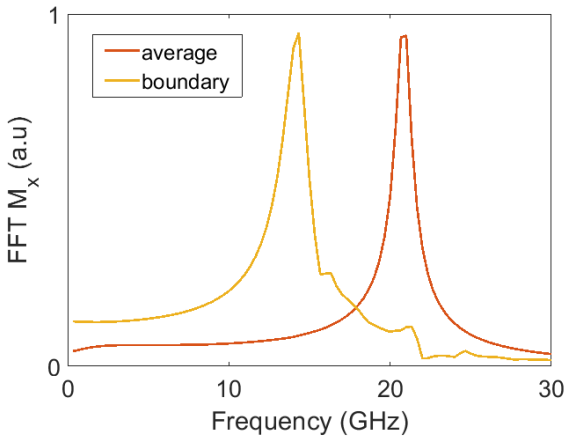

Figure 8.2: FFT of the x-component of the magnetisation following microwave excitation for a semi-infinite pillar of length 750 nm.

8.3 Magnetisation dynamics

In Figure 8.1, the temporal profile of the magnetisation in the x-y plane following excitation by the plane wave is shown at different instances of time for both conducting and non-conducting pillars. For the conducting pillar ($\sigma = 3.7 \times 10^{-6}(\Omega\text{m})^{-1}$) the excitation of the magnetisation is largest at the edges of the pillar and smallest towards the center, where almost no excitation of the magnetic material occurs. The precessing magnetisation exhibits a curling configuration which resembles the circumferential mode in ferromagnetic wires subject to microwave excitation [141]. This mode is strongly excited by the component of the electric field parallel to the long axis of the pillar. Moreover, the average coupling of the circumferential mode with a uniform microwave magnetic field is zero due its axial symmetry. As a consequence, the curling/circumferential mode is not excited in the numerical simulations for the case $\sigma = 0$ because this amounts to a uniform excitation of the magnetic material.

The uniform and non-uniform precession modes in the FDTD-LLG calculations were investigated by calculating the Fast Fourier Transform (FFT) of the magnetisation for the edge and bulk of the pillar. The spectrum for the two cases are shown in Figure 8.2. For the FFT evaluated from the average magnetisation only a single mode is observed at a frequency of 20.6 GHz. For the FFT evaluated at the boundary, an

additional mode is observed at a lower frequency of 14 GHz. It is readily seen from Figure 8.1 that the mode at 20.6 GHz is the ferromagnetic resonance of an axially magnetised pillar due to its uniform character for the case $\sigma = 0$. This mode is excited by the magnetic component of the microwave field. When the radius of a long wire is much larger than the skin depth, the surface impedances of all modes are equal to the surface impedance of a planar halfspace [141]. The excitation then occurs about small regions at the outer surface which behave like the ferromagnetic resonance of a thin film. In this situation, the resonance fields of all modes are identical and equal to Kittel's resonance formula for a planar plate

$$\omega_r = \gamma\sqrt{H_{eff}(H_{eff} + M_s)} \tag{8.5}$$

where H_{eff} is the effective field and M_s is the saturation magnetisation. The resonance frequency of the circumferential mode in wires can be well-described by this resonance equation. Using the same values $H_0 = 200$ Oe and $M_s = 8 \times 10^5$ A/m the frequency of this mode is 13.7 GHz, which is reasonably close to the simulated frequency of 14 GHz for the edge mode. The simulated frequency for the ferromagnetic resonance can be compared with theoretical calculations by evaluating the *magnetometric* demagnetising factor D_z of a homogeneous and uniform square prism magnetised along the pillar axis [142], defined here as the z-axis. The magnetometric demagnetising factor D_z in this case is given by

$$\pi D_z = \left(p - \frac{1}{p}\right)\ln\left(\frac{\sqrt{p^2+2}+1}{\sqrt{p^2+2}-1}\right) + \frac{2}{p}\ln(\sqrt{2}+1) + p\ln\left(\frac{\sqrt{p^2+2}+1}{\sqrt{p^2+2}-1}\right) + 2\arctan\left(\frac{1}{p\sqrt{p^2+2}}\right) + \frac{2(1-p^2)}{3p}\sqrt{p^2+2} + \frac{2(1-p^3)}{3p} - \frac{2^{3/2}}{3p} + \frac{2}{3}\sqrt{p^2+1}\left(2p - \frac{1}{p}\right)$$

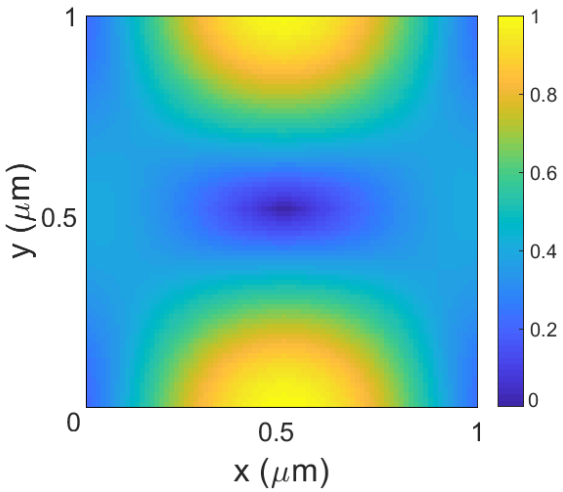

Figure 8.3: Spatial Fourier transform of the x-component of the magnetisation at 14 GHz for a semi-infinite prism of length 750 nm.

where $p = d/x$ is the ratio of the long axis to the side length. This equation is subject to the constraint

$$D_x + D_y + D_z = 1 \tag{8.6}$$

where D_x and D_y are the magnetometric demagnetising factors along the x and y directions. In the limit of an infinite prism $p \to \infty$ the magnetometric demagnetising factor along the z-axis tends to zero $D_z \to 0$. From equation (8.6) the other two magnetometric demagnetising factors are $D_x = D_y = 1/2$. The result is similar to the infinite circular cylinder. When the length of the prism is smaller than the skin depth, the resonance frequency is then to fair approximation given by the standard Kittel formula

$$\omega = \gamma\big(H_0 + \frac{M_s}{2}\big) \tag{8.7}$$

where ω is the frequency, H_0 is the DC field and M_s is the saturation magnetisation. For the values $H_0 = 200$ Oe and $M_s = 8 \times 10^5$ A/m the frequency is 19.7 GHz which again is reasonably close to the simulated value of 20.6 GHz. A degree of error invariably enters into the numerical computation due to the mesh resolution of the magnetic material, which is only 20^2 cells in this case. To investigate the spatial

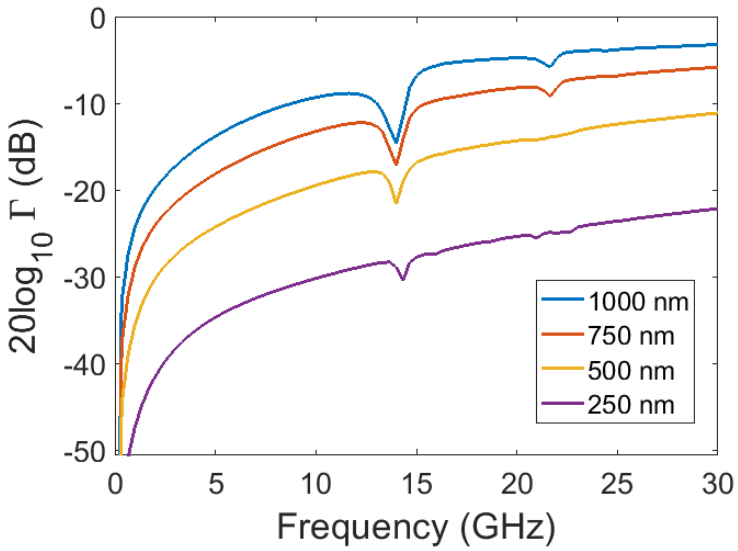

Figure 8.4: Reflection loss in dB plotted against frequency for semi-infinite pillars with sizes in the range $250 - 1000$ nm.

distribution of the edge mode in the prism, the spatial Fast Fourier Transform (FFT) was evaluated. This is achieved by calculating the Fourier transform of the magnetisation for every cell populated with magnetic material. The spatial distribution of the edge mode is shown in Figure 8.3 where it is clearly localised at the boundaries. The excitation of this mode is weakest towards the center, resulting in the spiral pattern shown in Figure 8.1 (top). As mentioned previously, this effect stems from the partial penetration of the microwave into the material.

8.4 Reflection loss

To understand the role that these modes play in microwave absorption the reflection loss was calculated for pillar sizes in the range $250 - 1000$ nm. In Figure 8.4 it can be seen that the circumferential (curling) mode at 14 GHz is the dominant mode for all sizes. This can be understood by examining the FFT plot in Figure 8.2 where the magnetic response of the curling mode is larger than the ferromagnetic resonance at the boundary of the pillar. Given that the microwave decays in amplitude towards the center of the conducting material, it is reasonable to expect that the magnetic

response at the boundary plays a larger role than the bulk. This effect can also explain why the flexural modes in spherical shells are well-excited in coaxial line experiments, given that they are localised close to the particle surface.

The additional peaks above the ferromagnetic resonance for the smallest samples can be attributed to non-uniform spin-wave modes. These modes were not found to contribute significantly to microwave absorption for the particular case of the TMz mode studied here. However, this is largely due to the choice of the Neumann boundary condition $\partial \mathbf{M}/\partial n = 0$ in the numerical simulations, resulting in unpinned surface spins at the air/metal interface. The spin-wave intensity can be substantially increased when a strong surface anisotropy is present. When the microwave field penetrates to the pillar axis it has been suggested that the curling magnetisation configuration can also increase the exchange energy [141], resulting in further shifts of the resonance fields.

8.5 Summary

In this chapter a hybrid electromagnetic and micromagnetic method was proposed based on the finite-difference time-domain (FDTD) Maxwell's equation framework. The novel FDTD-LLG algorithm was extended to model electromagnetic wave interaction with metallic magnetic nano-structures. The proposed numerical technique allows for the inclusion of exchange and anisotropy without imposing any simplification of the magnetic material, such as linearisation of the Landau-Lifshitz-Gilbert equation. The model was used to simulate the microwave response of semi-infinite metallic permalloy prisms in the size range $250 - 1000$ nm. It was found that microwave absorption results primarily from an edge mode localised close to the pillar surface. The spatial distribution and frequency of this mode was investigated and showed good agreement with a simplified analytical model. The results highlight the importance of the combined electromagnetic-micromagnetic numerical approach

to account for the full micromagnetic details within Maxwell's equations. With respect to finite materials, the assumption of *infinite* length is a good approximation whenever the magnetic surface charges at the ends of the pillar are negligibly small. Therefore, similar effects to those described here are expected for any finite prism of sufficient length.

Chapter 9

Summary and future work

9.1 Summary

In this thesis, the dynamical properties of ferromagnetic particles in the micrometer, sub-micrometer and nanometer size ranges were studied using a combination of analytical and numerical methods. This was to provide understanding of the resonance mechanisms in fine particle composites which are responsible for measured permeability spectra, and to enhance their magnetic response towards higher frequencies. We discovered the primary mechanism of microwave absorption in spherical particles and developed tools for simulation and analysis, including electro-micromagnetic software which couples the Landau-Lifshitz-Gilbert equaton to the complete solution of Maxwell's equations. Chapters 4 to 8 of this thesis provide the contribution to knowledge and advancement in the field and their main outcomes are outlined below.

In Chapter 4, the dynamical properties of saturated spherical shells was investigated analytically in the exchange-dominated regime. It was found that the presence of surface anisotropy plays an important role in the size dependent dynamical properties of spherical shells. Similar size dependant behaviour to the solid sphere was found for lower-order eigenvalues in the presence of surface anisotropy up to a thickness of $R_1/R_2 \approx 0.5$ after which large deviations began to occur, where R_1 and R_2 are

the inner and outer radii, respectively. Moreover, the presence of surface anisotropy was found to introduce a dependence of the zeroth mode on shell thickness, removing the degeneracy with the ferromagnetic resonance and leading to a pronounced size dependence of this mode for thin shells. In the final section of this chapter, the influence of a multilayered structure on the dynamical behaviour was investigated. The presence of a thin exchange-coupled outer shell was found to greatly shift the frequency of the exchange modes. This shift can be towards either higher or lower frequencies depending on the instrinic material parameters of the outer concentric shell.

In Chapter 5, the high-frequency dynamic behaviour of concentric permalloy nanorings supporting vortex domain structures was investigated by micromagnetic simulations. The long-range magnetostatic interactions were calculated and the impact on the ferromagnetic resonance was studied as a function of the geometric parameters of the system. The dynamic susceptibility was found to be significantly impacted by the presence of the long-range interaction between each ring. The coupling between neighbouring elements allowed for modulation of the frequency and amplitude of the resonances. The spatial localization of the uniform mode was also found to vary as a function of ring separation, corresponding to large variation in the amplitude of the real and imaginary components of the dynamic susceptibility.

In Chapter 6, the dynamic susceptibility of ferromagnetic spherical shells was investigated. The frequency of the higher order modes in saturated nanoshells were found to scale as $1/R_2^2$ in agreement with analytical calculations. A dependence on shell thickness was observed for the zeroth exchange mode even in the absence of surface anisotropy, which was attributed to the emergence of the 3D onion state in shells. Micromagnetic simulations of ground state structures revealed that a family of higher-order flexural modes can be excited in spherical shells which have been relaxed into the vortex state. In nanoshells these resonances appeared as narrow, intensive resonance bands localized primarily at the particle surface. For larger parti-

cles broader resonance bands were observed in the magnetic susceptibility, in addition to high-frequency resonances across the $15 - 25$ GHz frequency band.

In Chapter 7, the dynamical properties of relatively thick ($\approx$ 80 nm) permalloy elements supporting a vortex domain structure were investigated with numerical micromagnetic simulations, and compared with experiment. It was found that the static magnetisation configuration supports domain walls with perpendicular out-of-plane components which are three-dimensional in character. The polarity of the out-of-plane magnetisation can be switched dynamically in response to a magnetic pulse excitation. This is achieved by the formation of bullet-like excitations which propagate along the domain walls towards the corners of the element. Moreover, the presence of an external DC field was found to play an important role in the static properties of the permalloy elements.

In Chapter 8, a hybrid electromagnetic and micromagnetic method was proposed based on the finite-difference time-domain (FDTD) Maxwell's equation framework which can model electromagnetic wave interaction with metallic magnetic nanostructures. This numerical scheme offered efficiency and stability for solving the complex system of the combined Landau-Liftshitz-Gilbert (LLG) and Maxwell's equations. Numerical simulations were performed on semi-infinite permalloy prisms for sizes in the range $250-1000$ nm. The conductive properties of the prism were found to significantly impact the spatial distribution of the ferromagnetic resonance. Moreover, the partial penetration of the microwave into the material allowed for an additional edge mode to be excited, which played the dominant role in microwave absorption. The results indicate the importance of the combined electromagnetic-micromagnetic numerical approach to account for Eddy current screening and damping inside the magnetic material.

9.2 Future work

This thesis provided new found understanding into the topological, micromagnetic and electromagnetic properties of magnetic particles and their high-frequency behaviour. In particular, this research illustrates the rich parameter space available from the interplay between these intrinsic parameters to design and engineer magnetic particles or metastructures and composities supporting high-frequency permeabilities.

Building on this understanding, future work can focus on the resonance properties of magnetic particles with other geometrical features and domain configurations, such as novel curvature-induced DMI features. This research also focused on studying the dynamic response of spherical particles excited by small magnetic and electromagnetic fields to maintain operation in the linear regime of the dynamic response. Future work can consider the impact of increasing the magnitude and polarisation of the excitation field and nonlinear phenomena on the dynamic magnetic response.

The theoretical work and understanding of single particle behaviour developed here can be used to extend effective medium theories to predict the resonant properties of ensembles of particles with different packing fractions and dispersion of their magnetic and geometrical parameters. This would provide closer correlation between theoretical and experimental permeability spectra, and enable a quick route to determine the impact of varying composite parameters on the effective permeability.

The FDTD-LLG code can be extended to include multi-scale meshing in addition to graphical processing unit capabilities to improve computational load for large scale simulations of multi-particle arrays of novel magnetic particles supporting complex domain configurations. Development of a graphical user interface can further enable users to create and mesh geometries and materials in a user-friendly fashion.

The work in this thesis provides fundamental grounding to the extensions outlined above and to enable the design and engineering of high-frequency, high permeability composites for a wide range of applications in telecommunications, microwave devices and systems and spintronics.

Bibliography

[1] Streubel, R., Fischer, P., Kronast, F., Kravchuk, V. P., Sheka, D. D., Gaididei, Y., Schmidt, O. G., and Makarov, D. (2016) Magnetism in curved geometries. *Journal of Physics D: Applied Physics*, **49**, 363001.

[2] Liu, Q., Cao, Q., Bi, H., Liang, C., Yuan, K., She, W., Yang, Y., and Che, R. (2016) CoNi@SiO $_2$ @TiO $_2$ and CoNi@Air@TiO $_2$ microspheres with strong wideband microwave absorption. *Advanced Materials*, **28**, 486–490.

[3] Mercier, D., Lévy, J.-C. S., Viau, G., Fiévet-Vincent, F., Fiévet, F., Toneguzzo, P., and Acher, O. (2000) Magnetic resonance in spherical Co-Ni and Fe-Co-Ni particles. *Physical Review B*, **62**, 532–544.

[4] Wesselinowa, J. M. and Apostolova, I. (2007) Size and anisotropy effects on static and dynamic properties of ferromagnetic nanoparticles. *Journal of Physics: Condensed Matter*, **19**, 216208.

[5] Labaye, Y., Crisan, O., Berger, L., Greneche, J. M., and Coey, J. M. D. (2002) Surface anisotropy in ferromagnetic nanoparticles. *Journal of Applied Physics*, **91**, 8715.

[6] Hu, B., Zhao, C., and Li, Y. (2018) Modification of ferromagnetic nanostripe dynamic behavior by edge defects. *Materials Research Express*, **5**, 036111.

[7] Tanigaki, T., Takahashi, Y., Shimakura, T., Akashi, T., Tsuneta, R., Sugawara, A., and Shindo, D. (2015) Three-dimensional observation of magnetic vortex cores in stacked ferromagnetic discs. *Nano Letters*, **15**, 1309–1314.

[8] Vukadinovic, N., Vacus, O., Acher, O., and Pain, D. (2000) Magnetic excitations in a weak-stripe-domain structure: A 2d dynamic micromagnetic approach. *Physical Review Letters*, **85**, 2817–2820.

[9] Ding, J., Kakazei, G. N., Liu, X., Guslienko, K. Y., and Adeyeye, A. O. (2015) Higher order vortex gyrotropic modes in circular ferromagnetic nanodots. *Scientific Reports*, **4**, 4796.

[10] Boust, F. and Vukadinovic, N. (2004) Micromagnetic simulations of vortex-state excitations in soft magnetic nanostructures. *Physical Review B*, **70**, 172408.

[11] Gérardin, O., Youssef, J. B., Le Gall, H., Vukadinovic, N., Jacquart, P. M., and Donahue, M. J. (2000) Micromagnetics of the dynamic susceptibility for coupled permalloy stripes. **88**, 5899–5903.

[12] Wang, J., Zhang, B., Liu, Q., Ren, Y., and Liu, R. (2009) Micromagnetic calculation of dynamic susceptibility in ferromagnetic nanorings. *Journal of Applied Physics*, **105**, 083908.

[13] Fernández-Pacheco, A., Streubel, R., Fruchart, O., Hertel, R., Fischer, P., and Cowburn, R. P. (2017) Three-dimensional nanomagnetism. **8**, 15756.

[14] Gaididei, Y., Kravchuk, V. P., and Sheka, D. D. (2014) Curvature Effects in Thin Magnetic Shells. *Physical Review Letters*, **112**, 257203.

[15] Kravchuk, V. P., Roßler, U. K., Volkov, O. M., Sheka, D. D., van den Brink, J., Makarov, D., Fuchs, H., Fangohr, H., and Gaididei, Y. (2016) Topologically stable magnetization states on a spherical shell: Curvature-stabilized skyrmions. *Physical Review B*, **94**, 144402.

[16] Kravchuk, V. P., Sheka, D. D., Streubel, R., Makarov, D., Schmidt, O. G., and Gaididei, Y. (2012) Out-of-surface vortices in spherical shells. *Physical Review B*, **85**, 144433.

[17] Pylypovskyi, O. V., Kravchuk, V. P., Sheka, D. D., Makarov, D., Schmidt, O. G., and Gaididei, Y. (2015) Coupling of Chiralities in Spin and Physical Spaces: The Möbius Ring as a Case Study. *Physical Review Letters*, **114**, 144433.

[18] Yan, M., Kákay, A., Gliga, S., and Hertel, R. (2010) Beating the walker limit with massless domain walls in cylindrical nanowires. *Physical Review Letters*, **104**, 057201.

[19] Toneguzzo, P., Viau, G., Acher, O., Fiévet-Vincent, F., and Fiévet, F. (1998) Monodisperse Ferromagnetic Particles for Microwave Applications. *Advanced Materials*, **10**, 1032–1035.

[20] Toneguzzo, P., Acher, O., Viau, G., Pierrard, A., Fiévet-Vincent, F., Fiévet, F., and Rosenman, I. (1999) Static and dynamic magnetic properties of fine CoNi and FeCoNi particles synthesized by the polyol process. *IEEE Transactions on Magnetics*, **35**, 3469–3471.

[21] Toneguzzo, P., Acher, O., Viau, G., Fiévet-Vincent, F., and Fiévet, F. (1997) Observations of exchange resonance modes on submicrometer sized ferromagnetic particles. *Journal of Applied Physics*, **81**, 5546–5548.

[22] Aharoni, A. (1991) Exchange resonance modes in a ferromagnetic sphere. *Journal of Applied Physics*, **69**, 7762–7764.

[23] Aharoni, A. (1997) Effect of surface anisotropy on the exchange resonance modes. *Journal of Applied Physics*, **81**, 830–833.

[24] Viau, G., Fiévet-Vincent, F., Fiévet, F., Toneguzzo, P., Ravel, F., and Acher, O. (1997) Size dependence of microwave permeability of spherical ferromagnetic particles. *Journal of Applied Physics*, **81**, 2749–2754.

[25] Bukin, N., et al. (2016) Time-resolved imaging of magnetic vortex dynamics using holography with extended reference autocorrelation by linear differential operator. *Scientific Reports*, **6**, 36307.

[26] Brown, W. F., Jr. (1963) *Micromagnetics*. Wiley, New York.

[27] Sloika, M. I., Sheka, D. D., Kravchuk, V. P., Pylypovskyi, O. V., and Gaididei, Y. (2017) Geometry induced phase transitions in magnetic spherical shell. *Journal of Magnetism and Magnetic Materials*, **443**, 404–412.

[28] Goll, D., Berkowitz, A. E., and Bertram, H. N. (2004) Critical sizes for ferromagnetic spherical hollow nanoparticles. *Physical Review B*, **70**, 184432.

[29] A. Aharoni *Introduction to the Theory of Ferromagnetism, Clarendon Press, Oxford 1996*.

[30] Shibata, J., Tatara, G., and Kohno, H. (2011) A brief review of field- and current-driven domain-wall motion. *Journal of Physics D: Applied Physics*, **44**, 384004.

[31] Lebecki, K. M., Donahue, M. J., and Gutowski, M. W. (2008) Periodic boundary conditions for demagnetization interactions in micromagnetic simulations. **41**, 175005.

[32] Tannous, C. and Gieraltowski, J. (2006) The Stoner-Wohlfarth model of Ferromagnetism: Static properties. *arXiv:physics/0607117*.

[33] Lakshmanan, M. (2011) The fascinating world of the Landau-Lifshitz-Gilbert equation: an overview. *Philosophical Transactions of the Royal Society A: Mathematical, Physical and Engineering Sciences*, **369**, 1280–1300.

[34] Hickey, M. C. and Moodera, J. S. (2009) Origin of intrinsic gilbert damping. *Physical Review Letters*, **102**, 137601.

[35] Brown, W. F., Jr. (1963) Micromagnetics.

[36] Aharoni, A. (1991) Exchange resonance modes in a ferromagnetic sphere. *Journal of Applied Physics*, **69**, 7762–7764.

[37] Aharoni, A. (1997) Effect of surface anisotropy on the exchange resonance modes. *Journal of Applied Physics*, **81**, 830–833.

[38] Fiorani, D. *Surface Effects in Magnetic Nanoparticles, Chapter 5*.

[39] Arias, R., Chu, P., and Mills, D. L. (2005) Dipole exchange spin waves and microwave response of ferromagnetic spheres. *Physical Review B*, **71**, 224410.

[40] Dumas, E. and Sueur, F. (2014) On the Weak Solutions to the maxwell-landau-lifshitz Equations and to the hall-magneto-hydrodynamic equations. *Communications in Mathematical Physics*, **330**, 1179–1225.

[41] Boling, G. and Fengqiu, S. (1997) Global Weak Solution for the landau-lifshitz-maxwellEquation in Three Space Dimensions. *Journal of Mathematical Analysis and Applications*, **211**, 326–346.

[42] Vacus, O. and Vukadinovic, N. (2005) Dynamic susceptibility computations for thin magnetic films. *Journal of Computational and Applied Mathematics*, **176**, 263–281.

[43] Aziz, M. M. (2009) Sub-nanosecond electromagnetic-micromagnetic dynamic simulations using the finite-difference time-domain method. *Progress In Electromagnetics Research B*, **15**, 1–29.

[44] Kane Yee (1966) Numerical solution of initial boundary value problems involving maxwell's equations in isotropic media. *IEEE Transactions on Antennas and Propagation*, **14**, 302–307.

[45] Pereda, J., Vielva, L., Vegas, A., and Prieto, A. (1993) A treatment of magnetized ferrites using the FDTD method. *IEEE Microwave and Guided Wave Letters*, **3**, 136–138.

[46] Pereda, J., Vielva, L., Solano, M., Vegas, A., and Prieto, A. (1995) FDTD analysis of magnetized ferrites: application to the calculation of dispersion characteristics of ferrite-loaded waveguides. *IEEE Transactions on Microwave Theory and Techniques*, **43**, 350–357.

[47] Okoniewski, M. and Okoniewska, E. (1994) FDTD analysis of magnetized ferrites: a more efficient algorithm. *IEEE Microwave and Guided Wave Letters*, **4**, 169–171.

[48] Okoniewski, M. and Okoniewska, E. (1994) FDTD analysis of magnetized ferrites: a more efficient algorithm. *IEEE Microwave and Guided Wave Letters*, **4**, 169–171.

[49] Slodička, M. and Cimrák, I. (2003) Numerical study of nonlinear ferromagnetic materials. *Applied Numerical Mathematics*, **46**, 95–111.

[50] Tamion, A., Raufast, C., Hillenkamp, M., Bonet, E., Jouanguy, J., Canut, B., Bernstein, E., Boisron, O., Wernsdorfer, W., and Dupuis, V. (2010) Magnetic anisotropy of embedded Co nanoparticles: Influence of the surrounding matrix. *Physical Review B*, **81**, 144403.

[51] Jamet, M., Négrier, M., Dupuis, V., Tuaillon-Combes, J., Mélinon, P., Pérez, A., Wernsdorfer, W., Barbara, B., and Baguenard, B. (2001) Interface magnetic anisotropy in cobalt clusters embedded in a platinum matrix. *Journal of Magnetism and Magnetic Materials*, **237**, 293–301.

[52] Jamet, M., Wernsdorfer, W., Thirion, C., Dupuis, V., Mélinon, P., Pérez, A., and Mailly, D. (2004) Magnetic anisotropy in single clusters. *Physical Review B*, **69**, 024401.

[53] Dorfbauer, F., Evans, R., Kirschner, M., Chubykalo-Fesenko, O., Chantrell, R., and Schrefl, T. (2007) Effects of surface anisotropy on the energy barrier in cobalt-silver core-shell nanoparticles. *Journal of Magnetism and Magnetic Materials*, **316**, e791–e794.

[54] Luis, F., et al. (2006) Tuning the magnetic anisotropy of Co nanoparticles by metal capping. *Europhysics Letters (EPL)*, **76**, 142–148.

[55] Yanes, R., Chubykalo-Fesenko, O., Evans, R. F. L., and Chantrell, R. W. (2010) Temperature dependence of the effective anisotropies in magnetic nanoparticles with Néel surface anisotropy. *Journal of Physics D: Applied Physics*, **43**, 474009.

[56] Jamet, M., Wernsdorfer, W., Thirion, C., Mailly, D., Dupuis, V., Mélinon, P., and Pérez, A. (2001) Magnetic Anisotropy of a Single Cobalt Nanocluster. *Physical Review Letters*, **86**, 4676–4679.

[57] Salazar-Alvarez, G., et al. (2008) Cubic versus Spherical Magnetic Nanoparticles: The Role of Surface Anisotropy. *Journal of the American Chemical Society*, **130**, 13234–13239.

[58] Crespo, P., Litrán, R., Rojas, T. C., Multigner, M., de la Fuente, J. M., Sánchez-López, J. C., García, M. A., Hernando, A., Penadés, S., and Fernández, A. (2004) Permanent Magnetism, Magnetic Anisotropy, and Hysteresis of Thiol-Capped Gold Nanoparticles. *Physical Review Letters*, **93**, 087204.

[59] Mikhaylovskiy, R. V., Hendry, E., and Kruglyak, V. V. (2010) Negative permeability due to exchange spin-wave resonances in thin magnetic films with surface pinning. *Physical Review B*, **82**, 195446.

[60] Usov, N. A. and Grebenshchikov, Y. B. (2008) Influence of surface anisotropy on magnetization distribution in a single-domain particle. *Journal of Applied Physics*, **104**, 043903.

[61] Leonov, A. A., Dragunov, I. E., and Bogdanov, A. N. (2007) Surface-induced anisotropy and multiple states in elongated magnetic nanoparticles. *Applied Physics Letters*, **90**, 193112.

[62] Chappert, C. and Bruno, P. (1988) Magnetic anisotropy in metallic ultrathin films and related experiments on cobalt films (invited). *Journal of Applied Physics*, **64**, 5736–5741.

[63] Lee, J.-W., Jeong, J.-R., Shin, S.-C., Kim, J., and Kim, S.-K. (2002) Spin-reorientation transitions in ultrathin Co films on Pt(111) and Pd(111) single-crystal substrates. *Physical Review B*, **66**, 172409.

[64] Farle, M., Mirwald-Schulz, B., Anisimov, A. N., Platow, W., and Baberschke, K. (1997) Higher-order magnetic anisotropies and the nature of the spin-reorientation transition in face-centered-tetragonal Ni(001)/Cu(001). *Physical Review B*, **55**, 3708–3715.

[65] Hille, M., Frauen, A., Beyersdorff, B., Kobs, A., Heße, S., Frömter, R., and Oepen, H. P. (2013) Direct method for measuring the canting angle of magnetization. *Journal of Applied Physics*, **113**, 023902.

[66] Ramprecht, J. and Sjöberg, D. (2008) Magnetic losses in composite materials. *Journal of Physics D: Applied Physics*, **41**, 135005.

[67] Wang, H., Dai, Y., Gong, W., Geng, D., Ma, S., Li, D., Liu, W., and Zhang, Z. (2013) Broadband microwave absorption of CoNi@C nanocapsules enhanced by dual dielectric relaxation and multiple magnetic resonances. *Applied Physics Letters*, **102**, 223113.

[68] Ma, F., Qin, Y., and Li, Y.-Z. (2010) Enhanced microwave performance of cobalt nanoflakes with strong shape anisotropy. *Applied Physics Letters*, **96**, 202507.

[69] Wen, F., Yi, H., Qiao, L., Zheng, H., Zhou, D., and Li, F. (2008) Analyses on double resonance behavior in microwave magnetic permeability of multiwalled carbon nanotube composites containing Ni catalyst. *Applied Physics Letters*, **92**, 042507.

[70] Zhang, Q., Li, C., Chen, Y., Han, Z., Wang, H., Wang, Z., Geng, D., Liu, W., and Zhang, Z. (2010) Effect of metal grain size on multiple microwave resonances of Fe/TiO2 metal-semiconductor composite. *Applied Physics Letters*, **97**, 133115.

[71] Yong, Y., Yang, Y., Wen, X., and Jun, D. (2014) Microwave electromagnetic and absorption properties of magnetite hollow nanostructures. *Journal of Applied Physics*, **115**, 17A521.

[72] Wan, L., Zhang, J., Chen, Y., Wang, H., Hu, W., Liu, L., and Deng, Y. (2015) Preparation, characterization and microwave absorbing properties of nano-sized yolk-in-shell Ni-P nanospheres. *Journal of Physics D: Applied Physics*, **48**, 355302.

[73] Zou, J., Wang, Z., Yan, M., and Bi, H. (2014) Enhanced interfacial polarization relaxation effect on microwave absorption properties of submicron-sized hollow Fe $_3$ O $_4$ hemispheres. *Journal of Physics D: Applied Physics*, **47**, 275001.

[74] Xu, H.-L., Bi, H., and Yang, R.-B. (2012) Enhanced microwave absorption property of bowl-like Fe $_3$ O $_4$ hollow spheres/reduced graphene oxide composites. *Journal of Applied Physics*, **111**, 07A522.

[75] Mu, G., Chen, N., Pan, X., Yang, K., and Gu, M. (2007) Microwave absorption properties of hollow microsphere/titania/M-type Ba ferrite nanocomposites. *Applied Physics Letters*, **91**, 043110.

[76] Deng, Y., Zhao, L., Shen, B., Liu, L., and Hu, W. (2006) Microwave characterization of submicrometer-sized nickel hollow sphere composites. *Journal of Applied Physics*, **100**, 014304.

[77] Zhou, B., Wang, Y., Li, F., Tang, L., Wang, T., and Qiao, L. (2017) Submicron carbonyl iron particles as an efficient microwave absorber in the low frequency band. *Journal of Physics D: Applied Physics*, **50**, 475001.

[78] Néel, L. (1954) Anisotropie magnétique superficielle et surstructures d'orientation. *Journal de Physique et le Radium*, **15**, 225–239.

[79] Aharoni, A. (1987) Surface anisotropy in micromagnetics. *Journal of Applied Physics*, **61**, 3302–3304.

[80] Aharoni, A. (2002) Exchange Resonance Modes in a Hollow Sphere. *physica status solidi (b)*, **231**, 547–553.

[81] McKeever, C., Ogrin, F. Y., and Aziz, M. M. (2018) Influence of surface anisotropy on exchange resonance modes in spherical shells. *Journal of Physics D: Applied Physics*, **51**, 305003.

[82] Burgos, E., Sallica Leva, E., Gómez, J., Martínez Tabares, F., Vásquez Mansilla, M., and Butera, A. (2011) Surface pinning in ferromagnetic films with perpendicular anisotropy. *Physical Review B*, **83**, 174417.

[83] Heinrich, B., Celinski, Z., Cochran, J. F., Arrott, A. S., and Myrtle, K. (1991) Magnetic anisotropies in single and multilayered structures (invited). *Journal of Applied Physics*, **70**, 5769–5774.

[84] Abshinova, M. A., Lopatin, A. V., Kazantseva, N. E., Vilčákováa, J., and Sáhaa, P. (2007) Correlation between the microstructure and the electromagnetic properties of carbonyl iron filled polymer composites. *Composites Part A: Applied Science and Manufacturing*, **38**, 2471–2485.

[85] Chen, Y., Fan, X., Zhou, Y., Xie, Y., Wu, J., Wang, T., Chui, S. T., and Xiao, J. Q. (2015) Designing and Tuning Magnetic Resonance with Exchange Interaction. *Advanced Materials*, **27**, 1351–1355.

[86] Shimon, G., Adeyeye, A. O., and Ross, C. A. (2013) Magnetic vortex dynamics in thickness-modulated Ni 80 Fe 20 disks. *Physical Review B*, **87**, 214422.

[87] Chai, G., Wang, X., Si, M., and Xue, D. (2013) Adjustable microwave permeability of nanorings: A micromagnetic investigation. *Physics Letters A*, **377**, 1491–1494.

[88] Mu, C., Song, J., Xu, J., and Wen, F. (2016) Dynamic susceptibility of onion in ferromagnetic elliptical nanoring. *AIP Advances*, **6**, 065026.

[89] Giesen, F., Podbielski, J., Korn, T., and Grundler, D. (2005) Multiple ferromagnetic resonance in mesoscopic permalloy rings. *Journal of Applied Physics*, **97**, 10A712.

[90] Keatley, P. S., Yu, W., O'Brien, L., Read, D. E., Cowburn, R. P., and Hicken, R. J. (2014) Time-resolved Kerr microscopy of coupled transverse domain walls in a pair of curved nanowires. *Journal of Applied Physics*, **115**, 17D507.

[91] Hayward, T. J., Bryan, M. T., Fry, P. W., Fundi, P. M., Gibbs, M. R. J., Allwood, D. A., Im, M.-Y., and Fischer, P. (2010) Direct imaging of domain-wall interactions in Ni 80 Fe 20 planar nanowires. *Physical Review B*, **81**, 020410(R).

[92] Hayward, T. J., Llandro, J., Balsod, R. B., Bland, J. A. C., Morecroft, D., Castaí±o, F. J., and Ross, C. A. (2006) Switching behavior of individual pseudo-spin-valve ring structures. *Physical Review B*, **74**, 134405.

[93] Carvalho-Santos, V. L., Moura-Melo, W. A., and Pereira, A. R. (2010) Miniaturization of vortex-comprising system using ferromagnetic nanotori. *Journal of Applied Physics*, **108**, 094310.

[94] Jain, S. and Adeyeye, A. O. (2010) Aligned Alternating Head-to-Head and Tail-to-Tail Domain Walls in Ferromagnetic Concentric Rings. *IEEE Transactions on Magnetics*, **46**, 1595–1598.

[95] Avila, J. I., Tumelero, M. A., Pasa, A. A., and Viegas, A. D. C. (2015) Magnetoresistive system with concentric ferromagnetic asymmetric nanorings. *Journal of Applied Physics*, **117**, 103901.

[96] Yoo, Y. G., Kläui, M., Vaz, C. A. F., Heyderman, L. J., and Bland, J. A. C. (2003) Switching field phase diagram of Co nanoring magnets. *Applied Physics Letters*, **82**, 2470–2472.

[97] McKeever, C., Ogrin, F. Y., and Aziz, M. M. (2017) Dynamic susceptibility of concentric permalloy rings with opposite chirality vortices. *Journal of Applied Physics*, **121**, 203901.

[98] Walker, L. R. (1957) Magnetostatic Modes in Ferromagnetic Resonance. *Physical Review*, **105**, 390–399.

[99] Chu, P., Mills, D. L., and Arias, R. (2006) Exchange/dipole collective spin-wave modes of ferromagnetic nanosphere arrays. *Physical Review B*, **73**.

[100] Voltairas, P. A., Fotiadis, D. I., and Massalas, C. V. (2000) Mode mixing in ferromagnetic resonance in magnetic microspheres. *Journal of Applied Physics*, **88**, 374–378.

[101] Kong, D., Wang, S., and Chen, C. (2008) Magnetization ground states and phase diagrams for a nanosized Co hollow sphere: An onion-type magnetization state. *Journal of Applied Physics*, **104**, 013923.

[102] Yoo, Y. G., Kläui, M., Vaz, C. A. F., Heyderman, L. J., and Bland, J. A. C. (2003) Switching field phase diagram of Co nanoring magnets. *Applied Physics Letters*, **82**, 2470–2472.

[103] Noske, M., et al. (2016) Three-dimensional Character of the Magnetization Dynamics in Magnetic Vortex Structures: Hybridization of Flexure Gyromodes with Spin Waves. *Physical Review Letters*, **117**, 037208.

[104] Kim, S.-K., Yoo, M.-W., Lee, J., Lee, H.-Y., Lee, J.-H., Gaididei, Y., Kravchuk, V. P., and Sheka, D. D. (2015) Resonantly excited precession motion of three-dimensional vortex core in magnetic nanospheres. *Scientific Reports*, **5**, 11370.

[105] Lee, J.-H., Kim, J., Kim, M.-K., Sim, J., and Kim, S.-K. (2017) Nutation-like-mode excitation of coupled vortex cores in magnetic spherical shells. *Journal of Applied Physics*, **122**, 233903.

[106] Kurlyandskaya, G. V., Bhagat, S. M., Luna, C., and Vazquez, M. (2006) Microwave absorption of nanoscale CoNi powders. *Journal of Applied Physics*, **99**, 104308.

[107] Kittel, C. (1948) On the Theory of Ferromagnetic Resonance Absorption. *Physical Review*, **73**, 155–161.

[108] Lagarkov, A. N., Semenenko, V. N., Chistyaev, V. A., and Iakubov, I. T. (2012) High-frequency modes in magnetic spectra of carbonyl iron. *Journal of Magnetism and Magnetic Materials*, **324**, 3402–3405.

[109] Chen, A.-P., Gonzalez, J. M., and Guslienko, K. Y. Magnetization configurations and reversal of magnetic nanotubes with opposite chiralities of the end domains. **109**, 073923.

[110] Mehlin, A., Gross, B., Wyss, M., Schefer, T., Tütüncüoglu, G., Heimbach, F., Fontcuberta i Morral, A., Grundler, D., and Poggio, M. Observation of end-vortex nucleation in individual ferromagnetic nanotubes. **97**, 134422.

[111] Buchter, A., et al. Reversal mechanism of an individual ni nanotube simultaneously studied by torque and SQUID magnetometry. **111**, 067202.

[112] Vojkovic, S., Nunez, A. S., Altbir, D., and Carvalho-Santos, V. L. (2016) Magnetization ground state and reversal modes of magnetic nanotori. *Journal of Applied Physics*, **120**, 033901.

[113] Liu, Z., Che, R., Wei, Y., Liu, Y., Elzatahry, A. A., Dahyan, D. A., and Zhao, D. (2017) Broadening microwave absorption via a multi-domain structure. **5**, 046104.

[114] Gong, M., Kirkeminde, A., Skomski, R., Cui, J., and Ren, S. Template-directed FeCo nanoshells on AuCu. **10**, 4118–4122.

[115] Bolte, M., et al. (2008) Time-Resolved X-Ray Microscopy of Spin-Torque-Induced Magnetic Vortex Gyration. *Physical Review Letters*, **100**, 176601.

[116] Pribiag, V. S., Krivorotov, I. N., Fuchs, G. D., Braganca, P. M., Ozatay, O., Sankey, J. C., Ralph, D. C., and Buhrman, R. A. (2007) Magnetic vortex oscillator driven by d.c. spin-polarized current. *Nature Physics*, **3**, 498–503.

[117] Ruotolo, A., Cros, V., Georges, B., Dussaux, A., Grollier, J., Deranlot, C., Guillemet, R., Bouzehouane, K., Fusil, S., and Fert, A. (2009) Phase-locking of magnetic vortices mediated by antivortices. *Nature Nanotechnology*, **4**, 528–532.

[118] Dussaux, A., et al. (2010) Large microwave generation from current-driven magnetic vortex oscillators in magnetic tunnel junctions. *Nature Communications*, **1**, 1–6.

[119] Barman, A., Barman, S., Kimura, T., Fukuma, Y., and Otani, Y. (2010) Gyration mode splitting in magnetostatically coupled magnetic vortices in an array. *Journal of Physics D: Applied Physics*, **43**, 422001.

[120] Sukhostavets, O. V., Gonzalez, J. M., and Guslienko, K. Y. (2011) Magnetic Vortex Excitation Frequencies and Eigenmodes in a Pair of Coupled Circular Dots. *Applied Physics Express*, **4**, 065003.

[121] Han, D.-S., Vogel, A., Jung, H., Lee, K.-S., Weigand, M., Stoll, H., Schütz, G., Fischer, P., Meier, G., and Kim, S.-K. (2013) Wave modes of collective vortex gyration in dipolar-coupled-dot-array magnonic crystals. *Scientific Reports*, **3**, 2262.

[122] Jung, H., Yu, Y.-S., Lee, K.-S., Im, M.-Y., Fischer, P., Bocklage, L., Vogel, A., Bolte, M., Meier, G., and Kim, S.-K. (2010) Observation of coupled vortex gyrations by 70-ps-time- and 20-nm-space-resolved full-field magnetic transmission soft x-ray microscopy. *Applied Physics Letters*, **97**, 222502.

[123] Streubel, R., Kravchuk, V. P., Sheka, D. D., Makarov, D., Kronast, F., Schmidt, O. G., and Gaididei, Y. (2012) Equilibrium magnetic states in individual hemispherical permalloy caps. *Applied Physics Letters*, **101**, 132419.

[124] Yoo, M.-W. and Kim, S.-K. (2015) Curved geometrical confinement effect on vortex-state reversals in magnetic half-spheres. *Applied Physics Express*, **8**, 063003.

[125] Goll, D., Macke, S., Berkowitz, A., and Bertram, H. (2006) Magnetic ground states and the role of vortices in ferromagnetic hollow nanospheres. *Physica B: Condensed Matter*, **372**, 282–285.

[126] Katine, J. A., Albert, F. J., Buhrman, R. A., Myers, E. B., and Ralph, D. C. (2000) Current-Driven Magnetization Reversal and Spin-Wave Excitations in Co / Cu / Co Pillars. *Physical Review Letters*, **84**, 3149–3152.

[127] Kammerer, M., et al. (2011) Magnetic vortex core reversal by excitation of spin waves. *Nature Communications*, **2**, 279.

[128] Kim, S.-K., Lee, K.-S., Yu, Y.-S., and Choi, Y.-S. (2008) Reliable low-power control of ultrafast vortex-core switching with the selectivity in an array of vortex states by in-plane circular-rotational magnetic fields and spin-polarized currents. *Applied Physics Letters*, **92**, 022509.

[129] Bohlens, S., Krüger, B., Drews, A., Bolte, M., Meier, G., and Pfannkuche, D. (2008) Current controlled random-access memory based on magnetic vortex handedness. *Applied Physics Letters*, **93**, 142508.

[130] Van Waeyenberge, B., et al. (2006) Magnetic vortex core reversal by excitation with short bursts of an alternating field. *Nature*, **444**, 461–464.

[131] Verba, R. V., Hierro-Rodriguez, A., Navas, D., Ding, J., Liu, X. M., Adeyeye, A. O., Guslienko, K. Y., and Kakazei, G. N. (2016) Spin-wave excitation modes in thick vortex-state circular ferromagnetic nanodots. *Physical Review B*, **93**, 214437.

[132] Guslienko, K. Y., Novosad, V., Otani, Y., Shima, H., and Fukamichi, K. (2001) Magnetization reversal due to vortex nucleation, displacement, and annihilation in submicron ferromagnetic dot arrays. *Physical Review B*, **65**, 024414.

[133] Natali, M., Prejbeanu, I. L., Lebib, A., Buda, L. D., Ounadjela, K., and Chen, Y. (2002) Correlated Magnetic Vortex Chains in Mesoscopic Cobalt Dot Arrays. *Physical Review Letters*, **88**, 157203.

[134] Ding, J., Jain, S., Lapa, P. N., Khaire, T., Lendinez, S., Posada, C. M., Zhang, W., Pearson, J. E., Hoffmann, A., and Novosad, V. (2016) Gyrotropic frequency control in ferromagnetic dots using a nanoscale vortex barrier. *AIP Advances*, **6**, 056102.

[135] K. J. Binns, P. J. Lawrenson, and C. W. Trowbridge (1994) *The analytical and numerical solution of electric and magnetic fields*. John Wiley & Sons, New York.

[136] Yao, Z., Rüştü Umut, T., Itoh, T., and Wang, Y. E. (2018) A multiscale unconditionally stable time-domain (must) solver unifying electrodynamics and micromagnetics. *IEEE Transactions on Microwave Theory and Techniques*, **66**, 2683 – 2696.

[137] Reineix, A., Monediere, T., and Jecko, F. (1992) Ferrite analysis using the finite-difference time-domain (FDTD) method. *Microwave and Optical Technology Letters*, **5**, 685–686.

[138] Maksymov, I. S. and Kostylev, M. (2013) Impact of conducting nonmagnetic layers on the magnetization dynamics in thin-film magnetic nanostructures. *Journal of Applied Physics*, **113**, 043927.

[139] Greenwood, A. D., French, D. M., Hoff, B. W., and Heidger, S. L. (2014) Finite-difference time-domain/Landau-Lifshitz-Gilbert algorithm for modeling ferrites with hysteresis. *2014 USNC-URSI Radio Science Meeting (Joint with AP-S Symposium)*, Memphis, TN, USA, Jul., pp. 48–48, IEEE.

[140] Berenger, J.-P. (1994) A perfectly matched layer for the absorption of electromagnetic waves. *Journal of Computational Physics*, **114**, 185–200.

[141] Kraus, L., Infante, G., Frait, Z., and Vázquez, M. (2011) Ferromagnetic resonance in microwires and nanowires. *Physical Review B*, **83**, 174438.

[142] Aharoni, A. (1998) Demagnetizing factors for rectangular ferromagnetic prisms. *Journal of Applied Physics*, **83**, 3432–3434.